Cornelia Gießler

Theoretical investigations of electromagnetic control of glass melt flow

Theoretical investigations of electromagnetic control of glass melt flow

Von Cornelia Gießler

Universitätsverlag Ilmenau
2008

Impressum

Bibliografische Information der Deutschen Nationalbibliothek
Die Deutsche Nationalbibliothek verzeichnet diese Publikation in der Deutschen Nationalbibliografie; detaillierte bibliografische Angaben sind im Internet
über http://dnb.d-nb.de abrufbar.

Diese Arbeit hat der Fakultät Maschinenbau als Dissertation vorgelegen

Tag der Einreichung:	8. Februar 2008
1. Gutachter:	Univ.-Prof. Dr. rer. nat. habil. Andre Thess; Technische Universität Ilmenau
2. Gutachter:	Associate Professor Oleg Zikanov, University of Michigan, Dearborn
3. Gutachter:	Dr.-Ing. Ulrich Lange, SCHOTT AG, Mainz
Tag der Verteidigung:	2. Juni 2008

Technische Universität Ilmenau/Universitätsbibliothek
Universitätsverlag Ilmenau
Postfach 10 05 65
98684 Ilmenau
www.tu-ilmenau.de/universitaetsverlag

Herstellung und Auslieferung
Verlagshaus Monsenstein und Vannerdat OHG
Am Hawerkamp 31
48155 Münster
www.mv-verlag.de

ISBN 978-3-939473-37-4 (Druckausgabe)
urn:nbn:de:gbv:ilm1-2008000104

Abstract

The electromagnetic flow control of fluids with high electrical conductivity like liquid metals has been investigated so far and is well established in industrial processes. The application of electromagnetic (Lorentz) forces in fluids with a low electrical conductivity such as glass melts is a comparably new topic. The Lorentz force in glass melts can be generated by the interaction of an imposed electrical current and an external magnetic field. Basically, the Lorentz force can be used to regulate the mass flow rate in a duct or a pipe or to improve the mixing.

This theoretical work addresses both applications in glass melts and focuses on the consideration of the temperature-dependent viscosity and electrical conductivity.

In the first main part of the thesis the pipe flow of glass melt is studied on the basis of an one-dimensional analytical model. The flow is influenced by Lorentz force and gravity as well as temperature variation due to wall heat loss, electrical heating, advection, and heat diffusion. For high and very low driving forces the mean velocity is found to be proportional to the forces as known from laminar pipe flow with constant material properties. In between these two regimes, however, a new flow regime is identified. If there are no heat losses through the wall, the mean velocity is proportional to the square root of the driving force. In the presence of wall heat loss the solution for the steady flow is even found to be non-unique, and to involve bifurcations. This nonlinear behavior is shown to be a result of the closed-loop interaction between the velocity, temperature, and temperature-dependent material properties. The results of the analytical model are validated by two-dimensional axisymmetric numerical simulations. The non-unique flow characteristic could be observed in a simple non-magnetic experiment.

In the second main part of the thesis three-dimensional numerical simulations of glass melt in a small scale crucible heated by two rod electrodes are presented. The Lorentz force leads to an overall increase of the kinetic energy and, if it is the dominating driving force, the mean velocity is found to be an almost linear function of the Lorentz force. The transition from a buoyancy dominated flow regime to a Lorentz force dominated one and vice versa is characterized by a hysteresis. One obtains two steady solutions for one set of parameters depending on the starting conditions of the steady calculations. The three-dimensional problem is then reduced to an one-dimensional set of algebraic equations describing steady buoyancy driven laminar flow of glass melt in a closed loop under the influence of a localized Lorentz force. The loop is a highly simplified representation of a closed streamline in glass melt flow in the small scale crucible or a real furnace. The model reveals the role of temperature-dependent viscosity and conductivity in glass melt flows in a pure form that is not visible in full numerical simulations. Finally, the results obtained with the different approaches are compared with each other.

Zusammenfassung

Die elektromagnetische Strömungskontrolle von Flüssigkeiten mit hoher elektrischer Leitfähigkeit wird bereits in verschiedenen Bereichen industriell genutzt. Vergleichsweise neu ist die Anwendung elektromagnetischer (Lorentz) Kräfte zur Beeinflussung von Fluiden mit geringer elektrischer Leitfähigkeit, wie beispielsweise Glasschmelzen. Die Lorentzkraft in Glasschmelzen wird durch die Überlagerung eines eingeprägten elektrischen Stromes und eines externen Magnetfeldes erzeugt. Grundsätzlich kann die Lorentzkraft zur Durchflussregulierung und für das Durchmischen genutzt werden. Diese theoretische Arbeit widmet sich beiden Anwendungsmöglichkeiten unter Berücksichtigung der charakteristischen Materialeigenschaften von Glasschmelzen.

Im ersten Teil der Dissertation wird die Rohrströmung von Glasschmelzen anhand eines eindimensionalen analytischen Modells untersucht. Die Strömung wird durch Lorentzkraft und Gravitation beeinflusst. Weiterhin werden Temperaturänderungen durch Wärmeverluste, direkte elektrische Heizung, Konvektion und Wärmeleitung in die Betrachtung einbezogen. Wie bei laminarer Rohrströmung mit konstanten Materialeigenschaften hängt die mittlere Geschwindigkeit im Bereich hoher und sehr niedriger antreibender Kräfte linear von diesen ab. Für reine Heizung wird eine neue laminare Strömungscharakteristik beobachtet – das Quadrat der mittleren Geschwindigkeit ist proportional zur antreibenden Kraft. Bei Kühlung jedoch kann das Strömungsverhalten Bifurkationen – mehrwertige Lösungen – aufweisen, die bereits durch ein einfaches nicht-magnetisches Experiment nachgewiesen werden können. Dieses nichtlineare Verhalten wird durch die starke Kopplung von Geschwindigkeit, Temperatur und temperaturabhängigen Materialeigenschaften hervorgerufen. Die Ergebnisse des analytischen Modells werden durch zweidimensionale, axialsymmetrische Simulationen validiert.

Im zweiten Teil dieser Arbeit wird dreidimensionale Strömungssimulationen von Glasschmelze in einem Tiegel präsentiert. Die Lorentzkraft führt insgesamt zu einer Zunahme der kinetischen Energie. Die mittlere Geschwindigkeit ist eine lineare Funktion der Lorentzkraft, falls diese dominiert. Der Übergang von einer vorwiegend durch Auftrieb angetriebenen Strömung zu einer elektromagnetisch gesteuerten Strömung ist durch eine Hysterese gekennzeichnet. Man erhält zwei verschiedene stationäre Strömungsstrukturen für einen gegebenen Steuerparameter. Die Lösung hängt dabei von den Anfangsbedingungen der Berechnung ab. Weiterhin kann das dreidimensionale Problem auf eine Strömung in einem geschlossenen Rohrkreislauf reduziert werden. Die mittlere Geschwindigkeit wird dabei durch eine algebraische Gleichung beschrieben. Der geschlossene Rohrkreislauf ist die stark vereinfachte Darstellung einer geschlossenen Stromlinie in einem Tiegel unter dem Einfluss der Lorentzkraft. Das Modell ermöglicht klar den Einfluss der tempera-turabhängigen Viskosität und elektrischen Leitfähigkeit auf das Strömungsverhalten aufzuzeigen.

Contents

1 Introduction

> *Everything should be made as simple as possible, but not simpler.*
>
> A. Einstein

Glass is an ubiquitous material whose production is the most ancient form of industry as it can be dated back to 2,500 BC [81]. Nowadays the need of high quality glass products still requires permanent improvement of the production process and exploration of new production techniques. Furthermore, a reliable processing of glass melts needs an accurate flow prediction and reliable flow control mechanism. Electromagnetic forces are one possibility to control the flow of glass melts which is a comparatively new topic for glass manufacturers. For the application it is essential to know,

whether electromagnetic forces can lead to sufficient strong changes in the flow velocity so as to control the mass flow rate, to enhance mixing, and to generate any desired flow pattern.

The present thesis will answer this question on the basis of analytical models and numerical simulations for basic geometries to obtain a deeper understanding of the underlying physical mechanism. Moreover, the thesis will study,

how the glass melt material properties influence the electromagnetically driven flow.

In this chapter a brief introduction to the topic shall be given by describing electromagnetic forces in glass melts in Sec. 1.1, followed by an explanation of the characteristics of molten glass which are relevant for our considerations in Sec. 1.2. In Sec. 1.3 we briefly introduce common processing techniques and discuss possible applications of electromagnetic forces. This chapter concludes with the scope of the thesis in Sec. 1.4.

1.1 Electromagnetic forces in glass processing

While the application of electromagnetic forces for flow control in other areas of material processing like steel casting and production of aluminum is well established [13], the application of electromagnetic forces in glass melts is a comparably new topic. The difficulty with glass melts arises from the fact that their electrical conductivity is nearly five orders of magnitude smaller than that of liquid metals. Electromagnetic forces, also called Lorentz forces $\mathbf{f}$, are generated by the superimposition of an electric current density $\mathbf{J}$ and a magnetic flux density $\mathbf{B}$ according to

$$\mathbf{f} = \mathbf{J} \times \mathbf{B}. \tag{1.1}$$

We distinguish between different types of Lorentz forces as the origin of $\mathbf{J}$ and $\mathbf{B}$ are manifold [38].

The electric current density spreads out in electrically conducting media with the electrical conductivity $\sigma > 0$ S/m. The different possibilities of the current density generation are combined in Ohm's law [52]

$$\mathbf{J} = \sigma \left(-\nabla\phi + \mathbf{u} \times \mathbf{B} - \frac{\partial \mathbf{A}}{\partial t} \right). \tag{1.2}$$

The first component $-\sigma\nabla\phi$ results from the gradient of the spatial distributed electric potential $\nabla\phi$. Furthermore, the superimposition of the movement of an electrically conducting liquid or solid body with the velocity $\mathbf{u}$ and a magnetic field yields an so-called induced current density $\sigma(\mathbf{u} \times \mathbf{B})$. It is comparably small due to the small velocities and the low electrical conductivity of molten glass. During the modeling of electric current densities in glass melt flow this component is always neglected. Additionally, a time-varying magnetic field leads to a second induced current density component $\sigma(-\partial\mathbf{A}/\partial t)$ where $\mathbf{A}$ is the magnetic vector potential. This induced current is used in glass industry for cold crucible induction furnaces [39] as the frequency of the magnetic field is high. As we consider time-independent magnetic fields in the present work, this induced current density is zero.

The second component of the Lorentz force, the magnetic flux density $\mathbf{B}$ with $\mathbf{B} = \nabla \times \mathbf{A}$, can be given as an external magnetic field which we label $\mathbf{B_0}$. Furthermore, the electric current is surrounded by a magnetic field according to Ampere's law $\nabla \times \mathbf{B} = \mu\mathbf{J}$. In general, the magnetic field around spatial distributed currents in the glass melt is negligible whereas the magnetic field around current carrying electrodes $\mathbf{B_E}$ immersed into glass melt is comparably large [33].

The first Lorentz force component we like to introduce is based on the magnetic field around an electrode $\mathbf{B_E}$ and the electric current in the melt

$$\mathbf{f_{Ln}} = \sigma(-\nabla\phi) \times \mathbf{B_E}. \tag{1.3}$$

It is called *natural Lorentz force* and always exists in the vicinity of electrodes. A schematic diagram of f_{Ln} is given in Fig. 1.1(a). There is a long-standing and still unresolved controversy ([32], [9], [33]) as to whether naturally occurring electromagnetic forces should be included into models of glass melt flows. Similar flows occur in a variety of electromagnetic materials processing techniques and are often called electrically induced vortical flows [3]. We neglect the effects of the natural Lorentz force in our considerations as we focus on electromagnetic forces in glass melts which can be used to control the flow.

In the future the *induced Lorentz force*

$$\mathbf{f_{Li}} = \sigma(\mathbf{u} \times \mathbf{B_0}) \times \mathbf{B_0} \tag{1.4}$$

can become interesting for glass manufacturers as it is the basis for the Lorentz force velocimetry [73] which is already successfully used for the contactless mass flow measurement of liquid metals [40]. As shown in Fig. 1.1(b) it is formed by an induced current

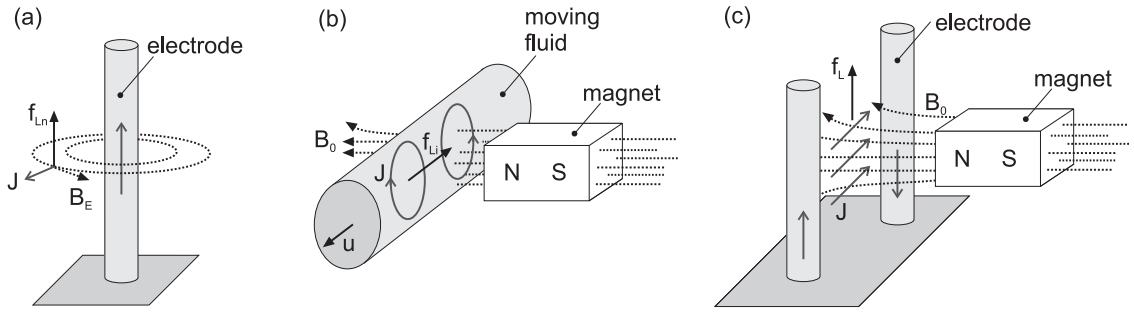

Figure 1.1: Lorentz forces in glass melt: (a) natural Lorentz force $\mathbf{f_{Ln}}$ in the vicinity of electrodes, (b) induced Lorentz forces $\mathbf{f_{Li}}$ as basis to measure contactlessly the mass flow rate, and (c) imposed Lorentz force $\mathbf{f_L}$ to control the flow.

density $\sigma(\mathbf{u} \times \mathbf{B_0})$ and an external magnetic field $\mathbf{B_0}$. One has to generate large magnetic flux densities $\mathbf{B_0}$ as σ and $\mathbf{u}$ in glass melts are approximately 10^5 and 10^3 times smaller than in liquid metals. But today's magnetic technique is not able to produce such magnitudes of the magnetic flux density for industrial applications. However, for future needs it is desirable to know how the temperature dependence of the viscosity and electrical conductivity influence the induced Lorentz force. In the course of his diploma thesis Schlegel [65] performed two-dimensional axisymmetric simulations of glass melt in a pipe with circular cross section. The pipe is surrounded by a current-carrying coil and cooled at the wall. During the parameter studies with the commercial software Comsol Schlegel systematically varied the cooling rate and the mass flow rate. As expected, with an increasing cooling rate the reduction of σ leads to a reduction of f_{Li}. Even more, Schlegel found an induced Lorentz force component which results from the characteristic material properties of glass melt and therefore is not part of the primary theory of the Lorentz force velocimetry [72]. However, due to the very small magnitudes of f_{Li} which Schlegel obtained during his studies we neglect its effect in the present thesis as well.

For the present thesis the important electromagnetic force is the *imposed Lorentz force* $\mathbf{f_L}$ being composed of the current density in the melt $\sigma(-\nabla\phi)$ and an external magnetic flux density $\mathbf{B_0}$ according to

$$\mathbf{f_L} = \sigma(-\nabla\phi) \times \mathbf{B_0}. \tag{1.5}$$

Fig. 1.1(c) gives a schematic drawing of the basic principle. The variable design of the distribution of $\mathbf{B_0}$ and of $(-\nabla\phi)$ allows for almost any desired orientation of the imposed Lorentz force. Its magnitude $f_L = |\mathbf{f_L}|$ depends on the magnitude of $B_0 = |\mathbf{B_0}|$, $|\nabla\phi|$ and σ. As the electrical conductivity σ is given by the composition of the glass melt, f_L is adjustable by the magnitudes of the two external control parameters, namely B_0 and $|\nabla\phi|$. Hence, the imposed Lorentz force is a very good control parameter to increase or reduce an existing mass flow rate. Moreover, the variable design of the orientation of $\mathbf{f_L}$ allows for the generation of almost any desired flow pattern. Therefore, $\mathbf{f_L}$ is the electromagnetic force which can be the basis of new techniques in glass processing. Before we discuss common processing techniques and possible applications of the imposed Lorentz force, we highlight the characteristics of glass melt and glass melt flow in the following section.

1.2 Characteristics of glass melt and glass melt flow

Glass melt is assumed to be a Newtonian fluid. It is characterized by a very high dynamic viscosity η and a very low electrical conductivity σ. Like the viscosity of magma and polymers, η of glass melt decreases nonlinearly with the temperature T. In glass science it is common to express this dependence with the so-called Vogel-Fulcher-Tammann equation [54], which is

$$\eta(T) = \eta_0 \, \exp\left(\frac{A}{T+B}\right). \tag{1.6}$$

The constant parameters η_0, A, and B depend on the fluid, whereas B is typically negative. Since $\eta \to \infty$ for $T \to |B|$ the viscosity law, Eq. (1.6), only makes sense for $T > -B$. The viscosity can vary more than one order of magnitude in typical working temperature ranges. In Tabs. A.1, A.2, and Fig. A.3 of the appendix examples can be found on the basis of three types of glass melts which we have considered in the thesis. Several analytical models describing the flow of magma [55], [30], [87], polymeres [63], and glass melt [48], [23] revealed that the temperature-dependent viscosity modifies the flow significantly. It can lead to non-linear flow characteristics, instabilities, and multi-valued solutions even in simple geometries like channels or pipes.

Like $\eta(T)$, the electrical conductivity $\sigma(T)$ can vary over one order of magnitude and can also be approximated by an exponential function, the law of Rasch and Hinrichsen

$$\sigma(T) = \sigma_0 \, \exp\left(-\frac{E}{T}\right), \tag{1.7}$$

again with constant parameters σ_0, and E specific to the considered glass melt [54]. In contrast to $\eta(T)$, the electrical conductivity is increasing with T. Depending on the composition of the melt and the temperature range there are typical values for the electrical conductivity ranging from $\sigma = 0.1$ S/m up to 10 S/m, which is about 10^4 to 10^6 times lower than σ of liquid metals. The dependence of σ on T is especially of interest for setups with an electric current distribution and hence, with imposed Lorentz forces $\mathbf{f_L}$, as $\mathbf{J}$ is proportional to $\sigma(T)$ according to Eq. (1.2). Let us note that the electric potential ϕ depends on σ as well, as it calculates from the Laplace equation

$$\nabla \cdot (-\sigma(T)\nabla\phi) = 0, \tag{1.8}$$

which results from the solenoidality of the current density $\nabla \cdot \mathbf{J} = 0$, and $\mathbf{J} = -\sigma(\nabla\phi)$. Additionally, the temperature dependency of σ influences the direct electrical heating significantly where the volumetric heat input is

$$q = \sigma(T)(\nabla\phi)^2. \tag{1.9}$$

In an unstable system a perturbation by an increasing temperature leads to an amplified $\sigma(T)$ and thus to an amplified q. If the heat transport mechanisms in the melt are not able to remove the increasing heat input, it results in higher temperatures. This self-induced runaway of the temperature is also denoted as *thermal instability* [76]. Previous studies have shown that mainly systems with pure heat conduction tend to be thermally unstable

whereas internal radiation stabilizes the system [67]. The thermal instability takes place in hot regions, e.g. locally around electrodes of production furnaces, or globally in small-scale crucibles with direct electric heating. If a required processing temperature is in such an unstable regime, the heat input has to be controlled continuously over the electric potential [69]. Alternatively, thermal stability can be achieved theoretically by assuming a constant current density $\mathbf{J_0}$ as it leads to

$$q = \frac{J_0^2}{\sigma(T)}. \tag{1.10}$$

Another characteristic of glass melts is a very large Prandtl number $\mathrm{Pr} \gg 1$ being defined by

$$\mathrm{Pr} = \frac{\eta c_P}{\lambda}, \tag{1.11}$$

with the heat capacity c_P, and the heat conductivity λ. The Prandtl number gives the ratio between the viscous and the thermal diffusion. It describes the relative growth of the velocity and the thermal boundary layer thickness, δ_s and δ_t, respectively. For laminar flow over a flat plate the relation $\mathrm{Pr}^{1/2} \sim \delta_s/\delta_t$ is valid [77]. Hence, for glass melt flow we can expect that the thermal boundary layer is much smaller than the velocity boundary layer, $\delta_t \ll \delta_s$. This characteristic of glass melts is important, e.g. for numerical simulations as the correct resolution of the extremely small boundary layer requires a study of the mesh. Therefore, the resolution of the boundary layers will be part of the mesh studies which we present in the Appendix A.4.

The flow of glass melts can be described as very slow and creeping. Therefore, the assumption of laminar flow is frequently used in the glass community. It is supported by a low Reynolds number $\mathrm{Re} < 1$ which gives the ratio of inertia and viscous forces in forced convection and is defined by

$$\mathrm{Re} = \frac{uL\rho}{\eta}, \tag{1.12}$$

with the magnitude of the velocity $u = |\mathbf{u}|$, the density ρ, and a characteristic length L.

However, the classification of the flow regimes for free convection, i.e. laminar, turbulent and the transition from laminar to turbulent, is based on the Rayleigh number Ra. It is the product of the Grashof and the Prandtl number and defined by

$$\mathrm{Ra} = \mathrm{Gr} \cdot \mathrm{Pr} = \frac{g\beta\Delta T L^3 \rho^2 c_P}{\eta\lambda}, \tag{1.13}$$

with the acceleration of gravity g, the thermal expansion coefficient β, and a characteristic temperature difference ΔT. The transition from a spatially symmetric laminar flow to an asymmetric laminar flow is of particular interest for glass melts. Typically, the Rayleigh number in glass melt flow can become large which implies that the symmetric laminar flow regime might be left. This symmetry breaking is observed for $\mathrm{Ra} \gtrsim 10^5$ in convection cells with bottom-heated and top-cooled walls (Benard cells) [44], [45], and as well in cavities with internal volumetric heat sources [46]. Studies with temperature-dependent viscosity representing the Earth's mantle convection showed that the transition shifts

to smaller values of Ra if the viscosity contrast within the system increases [56], [53]. Lim et al. [49] showed numerically for a container glass in a standard melting furnace without direct electrical heating that the flow can become unsteady for a volume-averaged Rayleigh number of $\mathrm{Ra} \sim 10^4$ and more chaotic for $\mathrm{Ra} \sim 10^6$, which occurred for typical length scales and temperature differences in the production process. It shows, that the frequently used assumption of symmetric and steady glass melt flow can be left and has to be controlled carefully.

Altogether, the underlying fluid dynamical problem of the high-Prandtl number fluid with nonlinear temperature-dependent viscosity and electrical conductivity is characterized by low Reynolds and high Rayleigh numbers.

Let us stress that the large variations of the material properties make it difficult to specify the exact values of the characteristic non-dimensional numbers. Therefore, frequently the non-dimensional numbers are given for a reference temperature or for certain values of the material properties. Additional characteristic numbers summarize the material property laws as suggested by Hrma [34]. In [49] Lim and co-workers used volume-averaged values of the non-dimensional numbers. This method will fail most of the time as it does not reflect the characteristics of the material properties. Alternatively, often just a coarse parameter domain for the characteristic numbers is given and the input and output parameters for a considered system carry SI units. In the present thesis we will introduce non-dimensional descriptions for analytical models like in Secs. 2.1 and 3.2 as the number of characteristic numbers is manageable. The results of the three-dimensional simulations of Sec. 3.1 are given in dimensional form due to the complexity of the physical model.

1.3 Flow control of glass melt

The goal of glass processing is to provide a chemical homogeneous melt to satisfy the quality standards which is carefully cooled down to a defined temperature and has a certain mass flow rate at the forming device. Electromagnetic forces are an alternative or an enhancement to already established manufacturing processes for all those requirements.

Most industrial furnaces for glass mass production are featured by continuous manufacturing processes. The design of such constructions is manifold, see e.g. [54], [76], [74]. Fig. 1.2 just pictures a simplified schematic drawing to explain the basics of the process. Typically the solid granular is continuously fed to the surface of the melt. Burners above the surface apply steady radiative non-uniform heat in horizontal direction which is inducing a thermally driven convection. Alternatively, in the case of electric melting, or in addition, in the case of electric boosting, electrodes are placed in the melt. The volumetric heat input leads to temperature gradients and buoyancy driven convection which is mixing the melt. The melt flows through a throat from the melting zone to the conditioning zone of the furnace in which the temperature homogenization starts. The furnace is connected to the forming device by a forehearth and a feeder which are usually ducts or pipes. In these feeder systems, the glass has to be cooled from the necessary refining temperature down to a suitable forming temperature. This cooling process must be carefully controlled in order to avoid defects induced by strong temperature gradients such as inhomogeneities

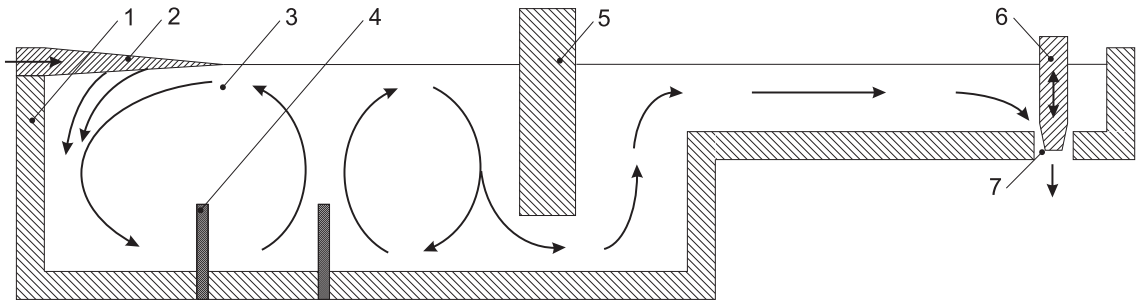

Figure 1.2: Simplified example of a furnace and a feeder system with 1 refractory walls, 2 solid granular – batch, 3 glass melt, 4 electrode, 5 throat, 6 plunger, and 7 outflow.

of the refractive index of the final product. Moreover, since the flow in a feeder is usually driven by the hydrostatic pressure difference only, the feeder system is also used for controlling the desired mass flow rate by pre-determined cooling. The control of the cooling rate is usually realized by applying an electrical current (either directly to the glass melt, or, if the walls of the feeder system are electrically conducting, to the walls of the pipe), which introduces Joule heat into the system. Likewise plungers are used to control the mass flow rate or to portion the melt by controlling the cross-sectional area of the outflow. Alternatively, imposed Lorentz forces could be used to control the mass flow rate. Kunert and co-workers first suggested in [47] the use of Lorentz forces to *control the mass flow rate* of glass melts in channels or pipes, particularly in feeders or forehearths. The force is generated in such a way that it is orientated in the same or opposite direction of the mainstream and leads to an increase or reduction of the mass flow rate. It is preferred to use electrodes situated at two opposite walls of the channel which can also be used to compensate heat losses. The remaining two walls are used for the access of the magnetic system. In chapter 2 we will catch up on the electromagnetic control of the mass flow rate by considering electromagnetically controlled glass melt flow in a pipe with circular cross section.

Imposed Lorentz forces can also be used to improve the *homogenization*, which takes place in all stages of the melt processing including forehearths and feeders. It is based on the diffusion at the interfaces between the different melt components or inhomogeneities. A maximization of the interface areas can be achieved by stretching and folding, hence by high flow gradients. Various operations are already part of the production process to introduce a flow in the melt. As already mentioned before, it is common to have a thermal convection by applying temperature gradients on the melt surface or in the melt volume. The temperature gradients are comparable small to achieve a good homogenization. Refinement bubbles, which may exist in the melt, can lead to a convection as well. In addition, gas bubbles are inserted into the melt via nozzles. The so-called bubbling increases convection locally, but leads to increasing wear of the refractory wall in the vicinity of the nozzles. Mechanical stirrers are often used and are typically installed just before the forming device. The stirrer material depends on the glass composition itself, e.g. the stirrer is made of platinum for optical glasses or ceramic for container glasses. It is disadvantageous that a minimum distance between the stirrer and the walls has to

be met to avoid corrosion. Therefore, mechanical stirrers can only influence parts of the melt.

1972 Walkden first patented [82] methods to use the imposed Lorentz force for homogenization. He suggested different arrangements in feeders and furnaces and recognized that the method allows for the production of a variety of different glass flow patterns. For a feeder system with three electrodes and two magnets a detailed schematic description of the flow pattern with different polarizations of the magnet is given. The patent lacks further detailed requirements, e.g. on the dimensions of the setup and on the composition of the melt. Without any explanation it just states that the ratio between imposed Lorentz force and buoyancy should be unity or larger at least in some regions of the melt. A different arrangement consisting of three pairs of electrodes and two magnets in a crucible was patented in 1981 by Michelson and co-workers in [51]. Depending on the control sequence of the alternating electric and magnetic fields the glass melt flows along three different closed trajectories being set orthogonal to each other. The authors developed a specific flow control regime, which is changing the direction of the trajectories every couple of minutes. Glass probes of the electromagnetic stirred melts are compared with mechanical stirred ones. It showed clearly a reduction of the number and the size of remaining bubbles and the disappearance of stria. Two years later, in 1983, Osmanis and co-workers generated superimposed oscillations in the melt by applying an additional high-frequent magnetic field [58]. Again, an improvement of the glass quality was shown. In [57] Osmanis et al. first mentioned the dimensions of the presented laboratory scale setup for electromagnetic stirring. As the velocity of the glass melt can not be measured directly, Fekolin & Stupak [18] performed a so called 'cold' experiment [70] with glycerin-based model fluids. The experiment represented a feeder with electric and magnetic fields to stir the pressure-driven fluid flow. Colored indicators were used to visualize the flow and to calculate the velocity. Studies for various electric currents, magnetic flux densities and compositions allowed the calculation of the electromagnetically controlled velocity in glass melts on the basis of similarity considerations. As the material properties were chosen for a reference temperature, this similarity analysis may fail and may lead to wrong results as the similarity did not consider the temperature-dependent electrical conductivity and viscosity [34]. The concept of electromagnetic control of buoyant driven convection in a small scale crucible of [57] was later taken up by Krieger and co-workers. Firstly they showed the influence of the imposed Lorentz force for two orientations on the basis of temperature measurements [35], [42]. To visualize the flow they then interpreted the stria formation in stacked melts using colored and colorless glass. In [43] the authors calculated the velocities of glass on the basis of temperature fluctuations. So far, the discussed arrangements given in the literature use pairs of rod electrodes only to impose $\mathbf{J}$. Lately, Halbedel et al. patented [29] the combination of an electrically conducting channel and a central electrode.

The literature survey showed that the number of publications about electromagnetic flow control of glass melts is limited. Altogether, the authors suggested a variety of arrangements to generate a variety of flow patterns. The published experimental results have proven the influence of the imposed Lorentz force for selected glass compositions, certain setups and a limited number of control parameters (the current density and the magnetic flux density). Furthermore, all authors state that small dimensions of the setup – like

in feeders or forehearths – are required for the generation of sufficient large magnetic flux densities. Setups with direct electric heating are predestined for the application of imposed Lorentz forces as the current density is already present and the added external magnetic field does not lead to additional impurities in the melt.

However, the published studies don't give universal statements about the influence of the imposed Lorentz force on glass melt flow. The effect of imposed Lorentz forces on a high-viscous and low-electrical conducting fluid with internal heat generation is still not well investigated. Especially the strong coupling of the velocity and temperature fields due to the temperature-dependent viscosity and electrical conductivity remains poorly understood.

1.4 Scope of thesis

The thesis contributes through theoretical investigations to a better understanding of glass melt flow under the influence of the imposed Lorentz force. A main focus is the consideration of the temperature-dependent viscosity and the temperature-dependent electrical conductivity to study their effects on non-isothermal flows. Reduced models for simple geometries shall give universal scale-relations for the velocity and temperature field as functions of the material properties and the imposed Lorentz force. The models permits one to investigate systematically the appearing physical mechanism. Furthermore, the models can state, how strong electromagnetic forces ought to be in order to control effectively the flow of a glass melt. The influence of spatial distributed imposed Lorentz forces on flow pattern will be studied by means of three-dimensional simulations for a selected setup. We will discuss under which conditions a desired flow pattern can be generated. The transition from a buoyancy driven flow to an electromagnetically controlled flow will be described in detail and will be compared with the universal scale relations. As the physical effects in glass melt flow are manifold, we concentrate on the already mentioned effects. We have decided to neglect certain effects, like heat transfer by internal radiation or natural Lorentz force. Therefore, they will not be discussed in this dissertation.

The thesis is basically subdivided into two main parts and structured as follows. In the next chapter, which constitutes the first main part of the thesis, we study an one-dimensional model of glass melt in a pipe with circular cross-section, originally published in [23]. The flow is influenced by imposed Lorentz force and gravity as well as temperature variation due to wall heat loss, direct electrical heating, and heat diffusion. It is a simplified representation of electromagnetically controlled glass melt flow in a feeder or forheart. Model validations by two-dimensional axisymmetric simulation [24] and a cold experiment identify the range of validity. In the second main part of this thesis, chapter 3, we focus on electromagnetic control of buoyancy driven convection based on two recent papers [26], [27] by the author and A. Thess. First we present complete three-dimensional simulations of glass melt in a crucible and study the velocity and temperature field for various electric potentials and magnetic flux densities. Furthermore, we reduce the three-dimensional problem to a single nonlinear equation for the cross-section averaged velocity in a closed loop which is a highly simplified representation of a closed streamline in glass

melt flow. The model is based on the energy equation for the temperature and the Stokes equation for the velocity distribution inside the loop. Due to the variety of considered models and methods we will give literature overviews and summaries of the results in the corresponding chapters and sections. The thesis concludes with a brief outlook on possible future studies in chapter 4.

2 Electromagnetically controlled flow in a pipe

First theoretical contributions to the laminar flow in a circular pipe were made independently by Eduard Hagenbach and by Franz Neumann as early as 1860. Now this flow is very well known as the so called Hagen-Poiseuille profile to commemorate the experimental work of Gotthilf H.L. Hagen in 1839 and Jean L.M. Poiseuille in 1840 [71]. Given such a long history it is difficult to imagine that there are still aspects of laminar pipe flow worth being investigated. However, one should have in mind that the known solution is valid only if the density and the viscosity of the fluid are constant. The goal of the present part of the thesis is to show that even a laminar pipe flow can become quite complex as soon as it is coupled with a temperature field due to strongly temperature-dependent viscosity and electrical conductivity. This class of problems is relevant for important applications in geophysics and engineering ranging form the investigation of lava flows to the flow of molten glass in forehearth or feeder systems in industrial glass manufacturing processes for products such as optical lenses or tubes for pharmaceutical packagings. Additionally, we are interested in the question whether imposed Lorentz force influences the flow of glass melt in a pipe and if the Lorentz force can be used to control the mass flow rate.

There are few analytical investigations which address the coupling between the temperature and velocity field caused by temperature-dependent material parameters despite its importance in geophysical and industrial applications. In the case of high Reynolds numbers $\mathrm{Re} \gg 1$ the influence of viscosity variation on the transition from laminar to turbulent pipe flow was studied, e.g. by Schärfer & Herwig [64], Wall & Nagata [83]. More relevant for our work are studies dealing with high viscosity variations for low Reynolds number flows, $\mathrm{Re} \ll 1$. In [55] Ockendon & Ockendon studied the two-dimensional steady flow of a Newtonian fluid driven by a constant mass flux in a rectangular channel. The channel walls were assumed to be suddenly heated or cooled. Effects of heat dissipation were neglected. Asymptotic descriptions for the velocity and temperature fields have been derived for polynomial and exponential variation of viscosity with temperature. Pearson [60] considered a plane channel flow with very intense heat generation and no cooling at the side walls. The similarity solution revealed the existence of a thin thermal boundary layer and an even thinner shear layer leading to plug flow almost across the whole channel. Extended asymptotic studies for circular pipe flows including viscous dissipation and solidification near cooled walls were performed by Richardson [63]. With the viscosity depending on the temperature and the shear rate, multi-valued relationships between flow rate and pressure-drop are found. Whitehead & Helfrich [86] considered a slot flow with cooled walls and a viscosity depending linearly on temperature. They treated the problem in the framework of the Hele-Shaw approximation where the velocity,

temperature and viscosity were averaged across the gap. For sufficiently large viscosity contrasts and a given pressure drop three steady state solutions for the velocity were found as well. Moreover, a stability analysis as well as experiments for pipe and slot flow were performed. This work for cross-averaged flow structures was continued by Helfrich [30]. He performed a detailed linear stability analysis and calculations of the nonlinear flow evolution. Fingering instabilities were found for sufficiently large viscosity gradients. In fast flowing zones hot fluid was found to be focused and moderately cooled, while in cold, slow flowing zones the fluid was shown to undergo strong cooling and to become very viscous. Wylie & Lister [87] studied a channel flow with cooled walls and viscosity depending on temperature. However, the authors of this work considered the full two- and three-dimensional flow structures and performed linear stability analysis of steady flows to two- and three-dimensional disturbances. The bifurcations observed in previous studies were confirmed. Lange & Loch [48] also developed analytical pipe flow models of a highly viscous fluid driven by a pressure gradient and affected by heat loss through the wall. In the simplest model the temperature was cross-section averaged. In a refined model the temperature distribution in the direction of the pipe radius was expanded asymptotically in terms of the Nusselt number. Also the calculations with glass melt parameters revealed bifurcations. The model was used to show how a cascade of heating circuits regulating the heat flux affected the location of the bifurcation in the parameter spectrum. The cascade of heating circuits was shown to change the flow for a desired flow rate from an unstable to a stable one.

In our work we consider laminar flow with strongly nonlinear temperature-dependent viscosity and cooled walls. We extend previous studies by including the effect of Joule heating, which appears if an electrical current flows through the fluid. As our work was prompted by investigations into the electromagnetic flow control of glass melts, the strongly nonlinear temperature dependence of the electrical conductivity is taken into account as well. To study the flow characteristics in a simplified way we derive a one-dimensional approximation to the energy and momentum equation. To this end the velocity, temperature and temperature-dependent material parameters will be averaged over the cross section of the pipe. As a result we shall be able to study the interplay between heating, cooling and the mentioned material parameters at minimum computational expense. Our aim is to analyze the temperature distribution and the velocity and their dependence on the external parameters, in particular on the imposed Lorentz force.

In Sec. 2.1 the considered configuration is explained and the governing equations for the temperature distribution and velocity in a circular pipe are derived. In Sec. 2.2 we briefly sketch the solution method. The results for the full nonlinear system are described and discussed in Sec. 2.3. Different cases are considered: (i) heating without cooling, (ii) heating and cooling, (iii) the influence of heat diffusion along the pipe axis, and (iv) example calculations for glass melt given in SI units. In Sec. 2.4 we discuss two-dimensional axisymmetric numerical calculations to validate the analytical one-dimensional model and in Sec. 2.5 we briefly introduce a simple non-magnetic laboratory experiment of the pipe flow model. Finally we summarize the key results of this work and give some concluding remarks in Sec. 2.6.

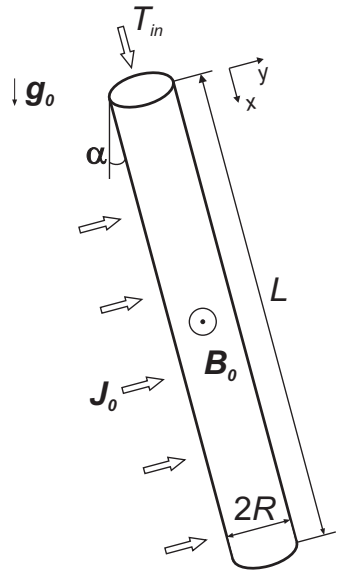

Figure 2.1: Sketch of the considered problem (not to scale).

2.1 Formulation of the analytical model

We consider a laminar and steady flow of a viscous electrically conducting fluid, preferable glass melt, in a circular pipe with the radius R and the length $L \gg R$ driven by gravity and Lorentz force as shown in Fig. 2.1.

The highly viscous Newtonian fluid with constant density ρ_0 is assumed to have strongly temperature-dependent viscosity and electrical conductivity according to Eq. (1.6) and Eq. (1.7), respectively. Furthermore, we assume that the fluid is thermally conducting with a constant effective thermal conductivity λ_0.

The glass melt flow is driven by gravity, which is not necessarily parallel to the axis of the pipe. We therefore only need to consider the component $\mathbf{f_g} = \rho_0 g \mathbf{e_x}$ of the gravity force acting along the axis of the pipe where $g = g_0 \cos\alpha$ and α is defined in Fig. 2.1. Moreover, we are interested in the question how the flow is modified when an imposed Lorentz force $\mathbf{f_L} = \mathbf{J_0} \times \mathbf{B_0}$ is created by the interaction of an electric current and a magnetic field. In practical applications one would like to know how this electromagnetic force, which acts along the pipe, affects the flow rate of glass melts. We assume that the Lorentz force is generated by a constant and steady external electrical current density $\mathbf{J_0} = J_0 \mathbf{e_y}$ and a homogeneous and steady external magnetic field $\mathbf{B_0} = B_0 \mathbf{e_z}$. $\mathbf{J_0}$ and $\mathbf{B_0}$ capture the whole volume of the pipe as shown in Fig. 2.1. The current density leads to heat production due to the Joule effect. The heat production per unit volume is given by $q = J_0^2/\sigma(T)$. Furthermore, we assume a low Brinkman number $\mathrm{Br} \ll 1$, describing the relation between viscous heating and fluid conduction. This assumption enables us to neglect the effects of viscous dissipation in the heat equation. At the pipe walls we assume that the heat transfer coefficient h and the surrounding temperature T_∞ are given. Then the heat flux at the wall can be computed invoking Newton's law of cooling [37]. In the

Appendix A.2 the validity of the convective boundary condition is shown on the basis of a typical pipe in glass processing.

The steady low-Reynolds number flow at hand is governed by the Stokes equation

$$0 = -\nabla p + \nabla \cdot \{\eta(T)[\nabla \mathbf{u} + (\nabla \mathbf{u})^T]\} + \rho_0 g \mathbf{e_x} + J_0 B_0 \mathbf{e_x}, \tag{2.1}$$

the heat equation

$$\rho_0 c_P (\mathbf{u} \cdot \nabla) T = \lambda_0 \nabla^2 T + \frac{J_0^2}{\sigma(T)}, \tag{2.2}$$

and the condition of incompressibility

$$\nabla \cdot \mathbf{u} = 0. \tag{2.3}$$

With the previously stated condition $L \gg R$ in mind, we assume that the thermal entry length is much smaller than the pipe length which is expressed as $uR^2/\lambda_0 \ll L$. This assumption enables us to reduce the three-dimensional governing equations (2.1)-(2.3) to a set of equations for a one-dimensional cross-section averaged temperature $T(x)$ and a single cross-section averaged velocity u. Since our fluid is incompressible, u does not depend on x. The necessary calculations are sketched in Appendix A.1. With our simplifying assumptions the momentum equation integrated over the pipe length becomes

$$L\rho_0 g + L J_0 B_0 = \frac{8u}{R^2} \int_0^L \eta(T) dx, \tag{2.4}$$

with the driving forces on the left hand side and the friction force on the right hand side. If the temperature distribution $T(x)$ were known, this equation would immediately provide the unknown velocity. However, this is not the case, and we have to invoke the heat equation to determine $T(x)$.

The simplified one-dimensional heat equation becomes

$$\rho_0 c_P u \frac{dT}{dx} = \frac{J_0^2}{\sigma(T)} - \frac{2h}{R}(T - T_\infty) + \lambda_0 \frac{d^2T}{dx^2}. \tag{2.5}$$

We impose the boundary conditions

$$T = T_{in} \quad \text{for} \quad x = 0, \tag{2.6}$$

$$\frac{dT}{dx} = 0 \quad \text{for} \quad x = L. \tag{2.7}$$

Eq. (2.5) represents the balance of heat advection described by the left hand side and the heat production due to the Joule effect, the heat loss through the side walls and the heat diffusion. The heat diffusion term in Eq. (2.5) contributes little to the heat balance for the applications relevant to our work. It is therefore neglected in most of our computations except for those discussed in Sec. 2.3.3. Our main focus is on the interplay between advection, heating and cooling. If the velocity u were known, Eq. (2.5) with the

boundary conditions (2.6) and (2.7) would give us $T(x)$. However, u is unknown until we have solved the remanent of the Stokes equation (2.4). This illustrates the closed-loop interaction between the velocity and the temperature in our problem.

To cast the governing Eqs. (2.4)-(2.5) into a non-dimensional form the structure of the material parameters has to be taken into account. We introduce a non-dimensional temperature as follows:

$$\theta = \frac{T}{E}.$$

Furthermore, we introduce the non-dimensional longitudinal coordinate x', the non-dimensional velocity u', the control parameters M, P, N, K and the material parameters S, Q according to

$$x' = \frac{x}{L},\ u' = \frac{8\eta_0}{R^2\rho_0 g}\ u,\ M = 1 + \frac{J_0 B_0}{\rho_0 g},\ P = \frac{8\eta_0 L}{\rho_0^2 \sigma_0 g c_P E R^2}\ J_0^2,$$

$$N = \frac{16\eta_0 L}{\rho_0^2 g c_P R^3} h,\ K = \frac{8\eta_0}{\rho_0^2 g c_P R^2 L}\lambda_0,\ S = \frac{E}{A},\ Q = \frac{B}{A}.$$

The forcing parameter M is a measure for the applied Lorentz force in relation to the effective gravity. Changing M is equivalent to changing the applied Lorentz force. Without the Lorentz force $M = 1$. The parameter P is proportional to the square of the electric current density and therefore a measure of the injected heat. All other quantities entering P are constant geometry and material parameters. The same is true for N and K. As N is proportional to h it is a non-dimensional measure for the wall heat loss. The parameter K is a measure for the heat diffusion because of its proportionality to λ_0. The parameters S and Q are material parameters related to the electrical conductivity and viscosity.

After performing the nondimensionalisation and dropping the primes we obtain the following non-dimensional set of governing equations

$$M = u \int_0^1 \exp\left(\frac{1}{S\theta + Q}\right) dx, \tag{2.8}$$

$$u\frac{d\theta}{dx} = P\ \exp\left(\frac{1}{\theta}\right) - N(\theta - \theta_\infty) + K\frac{d^2\theta}{dx^2}, \tag{2.9}$$

$$\theta = \theta_{in} \quad \text{for} \quad x = 0, \tag{2.10}$$

$$\frac{d\theta}{dx} = 0 \quad \text{for} \quad x = 1. \tag{2.11}$$

The governing equations (2.8)-(2.9) for the considered problem consist of an integral and a second order differential equation which determine the nondimensional velocity u and temperature distribution $\theta(x)$. Eq. (2.8) expresses the balance between the driving forces on the left hand side and the length-integrated viscous friction on the right hand side. Eq. (2.9) represents the balance between advection on the left hand side and Joule heating, wall heat loss, and heat diffusion on the right hand side.

The governing Eqs. (2.8)-(2.9) are coupled by the temperature $\theta(x)$, which appears in the friction term of the momentum equation because of the considered temperature-dependent viscosity. The second coupling is due to the appearance of u in the heat equation. Equations (2.8) and (2.9) could also be combined into a single integro-differential equation for $\theta(x)$ by eliminating u. But we have decided to keep them separate to highlight their origin from the momentum and heat equation (2.1) and (2.2), respectively. Furthermore, one of the parameters M, P, N or K is redundant and can be scaled to 1. We did not apply this scaling to underline the physical source of these parameters.

In the analysis that follows we are most interested in the flow characteristic u as a function of the forcing parameter M and the temperature field $\theta(x)$ under the influence of various heating parameters P, wall heat loss parameters N, and diffusion parameters K. The rest of Sec. 2 is devoted to the treatment of the system (2.8)-(2.9).

2.2 Solution method

We solve the nonlinear integro-differential set of Eqs. (2.8)-(2.9) using a two-step numerical procedure. In the first step the differential equation (2.9) is integrated for an initial guess of the given mean velocity u. If a system without diffusion is investigated, $K = 0$, the resulting first-order differential equation is solved with a Runge-Kutta method for a given entrance temperature θ_{in}. For this case the second boundary condition, Eq. (2.11), is discarded. The complete second-order differential equation with diffusion is rewritten as a set of two differential equations of first-order and is solved by applying a shooting method to fulfill the boundary conditions. In the course of the shooting procedure the stiff set of equations is solved with an implicit Runge-Kutta method. Shooting from the inlet, $x = 0$, requires an initial guess for the temperature gradient at $x = 0$. For $u/K \gg 1$ the calculated temperature distribution is extremely sensitive to this guess. We observe that the given boundary condition at $x = 1$ could not be reached even by applying special root finding methods like Ridders' algorithm [62] to determine the initial guess. We have avoided these convergence problems by shooting from the outlet. We prescribed the outlet temperature θ_{out} and varied it using a root finding method to meet the required inlet temperature θ_{in}. We found the solution to converge for a wide range of u/K even for a rough initial guess of θ_{out} and a simple root finding procedure like the bisection method.

In the second step the resulting temperature distribution $\theta(x)$ is used to compute the integral of Eq. (2.8) with the help of the extended trapezoidal rule. For a given force parameter M, we use a root-finding method to find u so as to obey the governing equations. For a given velocity u, the unknown force M is uniquely determined with Eq. (2.8).

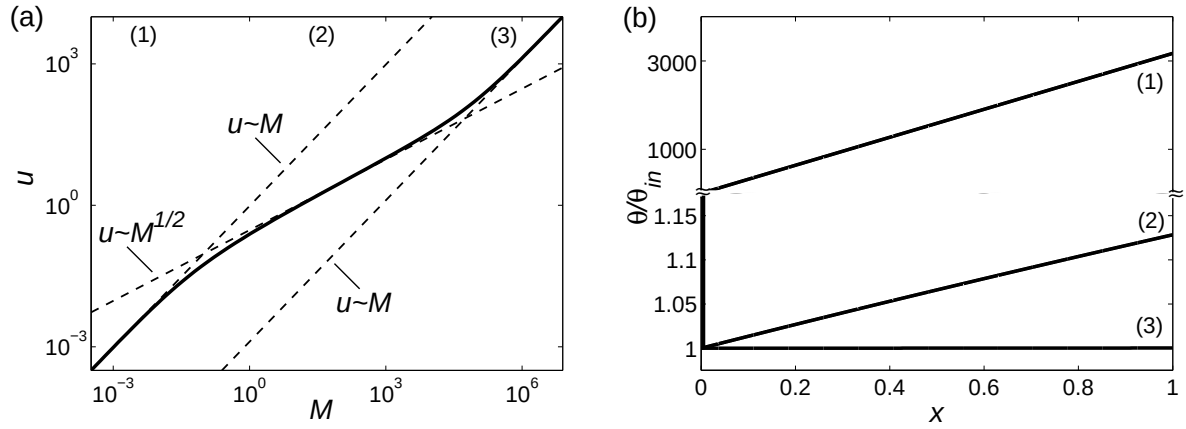

Figure 2.2: Flow regime for internal heating, $P = 1$, no wall heat loss, $N = 0$, no diffusion, $K = 0$ and $S = \theta_{in} = 1$, $Q = -0.85$: (a) Velocity u as a function of the forcing parameter M being the solution of Eqs. (2.8)-(2.9). The curve is divided into three branches: for low (1) and high velocities (3) the relation $u \sim M$ is fulfilled. For intermediate velocities (2) a scaling $u \sim M^{1/2}$ is found as indicated by the dashed lines. (b) Representative distribution of normalized temperature θ/θ_{in} along x for each of the branches defined in (a).

2.3 Selected results

2.3.1 Heating without wall heat loss

In this part we discuss our results for a system without wall heat loss, $N = 0$, and without heat diffusion, $K = 0$. The material parameters are set to $S = 1$ and $Q = -0.85$ while the inlet temperature is set to $\theta_{in} = 1$, respectively. This case is characterized by a balance between advection and Joule heating. Fig. 2.2(a) shows the dependence of the velocity on the forcing parameter for one heating parameter. In Fig. 2.2(b) the temperature distribution normalized to the inlet temperature for slow, moderate and high velocities is plotted. In general, the velocity u is a monotonically increasing function of the forcing parameter M. For low and high forces the velocity is proportional to the force $u \sim M$ as it is known from laminar pipe flow with constant material parameters. But in between these linear domains we find that the velocity varies as $u \sim M^{1/2}$.

How can these regimes be explained? The key to the explanation is the link between the driving force M and the velocity u provided by the viscosity integral in Eq. (2.8). As a consequence, the "friction law" $u(M)$ depends on the viscosity distribution $\exp[1/(S\theta(x)+Q)]$ along the pipe. The viscosity distribution differs considerably for each of the branches (1), (2) and (3) as it is sketched in Fig. 2.3. For a constant viscosity, the velocity and the force are related linearly as $u \sim M$. This is the case for strong forcing and high velocities because the heating effect is very weak due to the low residence time. In this case the temperature is nearly constant, i.e. $\theta(x) = \theta_{in}$ (see curve (3) in Fig. 2.2(b) which leads to a constant viscosity as can be seen in curve (3) of Fig. 2.3. For this case the momentum Eq. (2.8) becomes $M = u \exp(1/(S\theta_{in} + Q))$ with $\exp(1/(S\theta_{in} + Q)) > 1$

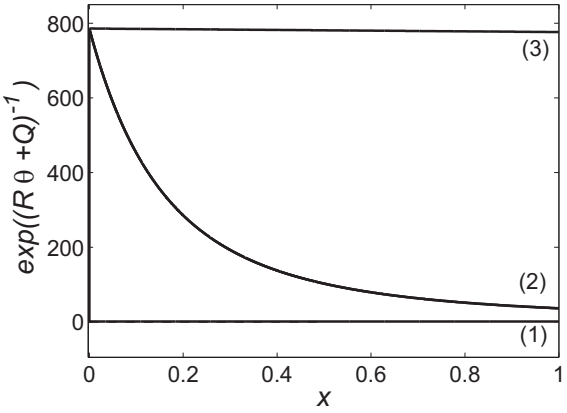

Figure 2.3: Examples of the distribution of the non-dimensional viscosity $\exp(1/(S\theta + Q))$ along the pipe axis x for the branches (1), (2) and (3) defined in Fig. 2.2(a) and obtained with the same set of parameters.

for $(S\theta_{in} + Q) > 0$ and provides the desired linear relationship on branch (3). For very low velocities, corresponding to branch (1) in Fig. 2.2(a), the viscosity does not change along the pipe either. In this case the melt is heated up very quickly as soon as it enters the pipe. This leads to a very high electrical conductivity and very low Joule heating, respectively. As a result of the high temperatures in this branch, the viscosity jumps quickly to its lowest possible value corresponding to $\exp((S\theta + Q)^{-1}) \to 1$ and remains virtually constant along x. This effect is seen in curve (1) of Fig. 2.3. The force M attains its theoretically lowest possible value and we have $M = u$. For moderate velocities, i.e. between the two linear flow regimes (1) and (3), the relationship between M and u becomes nonlinear as the temperature distribution – and hence the viscosity integral – is sensitive to velocity changes.

An explanation of these phenomena can also be given on the basis of an asymptotic algebraic solution to Eqs. (2.8)-(2.9). This solution has the virtue to display the interaction between the temperature-dependent viscosity and the driving forces in its purest form. First we expand the temperature in x around the pipe entrance, e.g. $\theta \approx \theta_{in} + \frac{d\theta}{dx}x$, to obtain a linear temperature distribution. With the derivative $d\theta/dx$ evaluated from the heat balance given by Eq. (2.9), the linearized temperature field becomes

$$\theta = \theta_{in} + \left\{ \frac{P}{u} \exp\left(\frac{1}{\theta_{in}}\right) \right\} x. \tag{2.12}$$

This expression is valid for moderate and large velocities as its derivation requires $u \gg P/\theta_{in} \exp(1/\theta_{in})$. Although Eq. (2.12) is a crude simplification, it shows the influence of the the parameters on the temperature distribution along the pipe. The temperature gradient increases with the heating parameter P, but decreases with velocity u due to a reduced residence time. The temperature gradient depends strongly on the inlet temperature θ_{in} due to the exponential temperature-dependence of the electrical conductivity. Particularly for a low inlet temperature $\theta_{in} \ll 1$ the temperature gradient is strongly amplified since $\exp(1/\theta_{in}) \gg 1$. Using Eq. (2.12) the momentum equation (2.8) simplifies

to

$$M = u \int_0^1 \exp\left\{ \frac{1}{S\theta_{in}+Q} \cdot \frac{1}{1+\frac{SP}{S\theta_{in}+Q}\frac{1}{u}\exp\left(\frac{1}{\theta_{in}}\right)x} \right\} dx. \tag{2.13}$$

With

$$Z = \frac{1}{S\theta_{in}+Q}, \;\; \hat{M} = \frac{M}{SPZ}\exp\left\{-Z-\frac{1}{\theta_{in}}\right\},$$

$$\hat{u} = \frac{u}{SPZ}\exp\left\{-\frac{1}{\theta_{in}}\right\} \;\text{ and }\; X = \frac{x}{\hat{u}}$$

Eq. (2.13) becomes

$$\hat{M} = \hat{u}^2 \int_0^{1/\hat{u}} \exp\left\{-\frac{ZX}{1+X}\right\} dX. \tag{2.14}$$

Thus our problem can be considered as a Laplace-type integral of the form $I(Z) = \int_a^b f(X)\exp\{Z\phi(X)\}dX$ with $f(X) = 1$ and $\phi(X) = -X/(1+X)$. The coefficient Z characterizes the viscosity at the pipe entrance $x = 0$ whose non-dimensional value is

$$\eta_{in} = \exp\left\{\frac{1}{S\theta_{in}+Q}\right\}. \tag{2.15}$$

Now we assume that this viscosity is very large which is equivalent to $X \to \infty$. With this assumption we are able to solve the integral $I(Z)$ by integration by parts leading to $I(Z) \approx f(X)\exp\{Z\phi(X)\}/(Z\phi'(X))\;|_a^b$ as it is explained in ref. [2]. Observe that this asymptotic evaluation of the Laplace-type integral does not require the function $\phi(X)$ to have any particular property apart from steadiness. After applying this method for fixed $\hat{u}$ with $O(1/Z)$ correction and an additional transformation with $\widetilde{M} = \hat{M}/Z$ and $\widetilde{u} = \hat{u}/Z$ we obtain

$$\widetilde{M} = \widetilde{u}^2\left[1-\exp\left(-\frac{1}{\widetilde{u}}\right)\right]. \tag{2.16}$$

Already this simple and compact algebraic equation describes a very interesting flow behavior, which is shown in Fig. 2.4. For $\widetilde{u} \gg 1$ one can use the linear expansion $\exp(-1/\widetilde{u}) = 1 - 1/\widetilde{u}$ of the exponential function in which case Eq. (2.16) becomes $\widetilde{u} \sim \widetilde{M}$. For this case the velocity $\widetilde{u}$ is proportional to $\widetilde{M}$ as expected for a laminar flow. In contrast, for $\widetilde{u} \ll 1$ the exponential function in Eq. (2.16) tends to zero, $\exp(-1/\widetilde{u}) \to 0$. As a result the velocity changes according to $\widetilde{u} \sim \widetilde{M}^{1/2}$.

However, this approximation requires moderate and big velocities and very big entrance values of the viscosity $\eta_{in} \to \infty$. For very small velocities, which is equivalent to $X \gg Z$, Eq. (2.16) misses an $O(\exp(-Z)/\hat{u})$ correction from the solved integral approximation. This explains why it does not reproduce branch (1) and shows a nonlinear behavior $M \sim u^2$ for small velocities in contrast to the exact solution. A direct comparison between the analytical and exact solutions for one set of parameters is shown in Fig. 2.5.

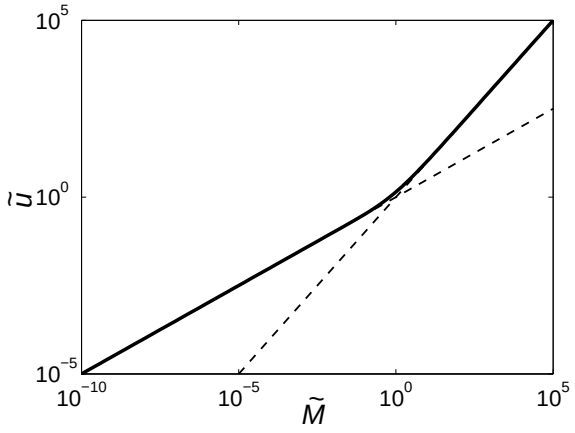

Figure 2.4: Transition between linear and nonlinear friction law for a short pipe: Velocity $\widetilde{u}$ as a function of the force $\widetilde{M}$ as obtained from solving Eq. (2.16). The curve is divided into two branches: for strong forces $\widetilde{M} \gg 1$ the velocity changes according to $\widetilde{u} \sim \widetilde{M}$ as for ordinary laminar pipe flow with constant material parameters. For weak forces $\widetilde{M} \ll 1$ the relation $\widetilde{u} \sim \widetilde{M}^{1/2}$ is fulfilled.

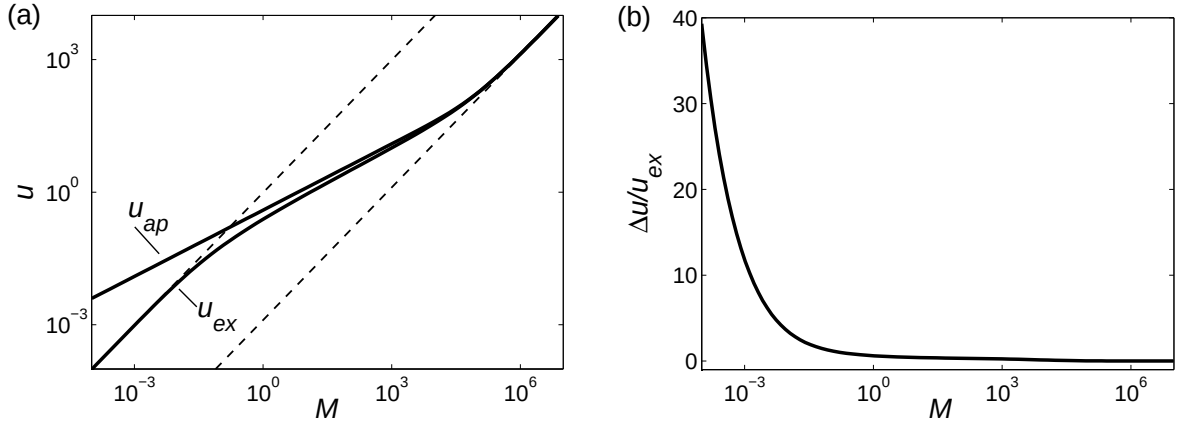

Figure 2.5: (a) Comparison between the exact velocity u_{ex} and the approximated velocity u_{ap} as function of the forcing parameter M as obtained by solving Eqs. (2.8)-(2.9) and Eq. (2.16), respectively. (b) Relative velocity difference $(u_{ap} - u_{ex})/u_{ex}$ as a function of the forcing parameter M. The calculations are performed with the set of parameters used for Fig. 2.2 and 2.3.

Fig. 2.6 shows, how the modification of η_{in} influences the nonlinear flow regime. For $\eta_{in} \approx 1$ the nonlinear branch is virtually absent. The larger η_{in} becomes, the stronger the nonlinear branch develops as the transition zone between maximum viscosity for fast flows $P/u \to 0$ and minimal viscosity for slow flows $P/u \to \infty$ increases. In Fig. 2.6 η_{in} varies as the material parameter Q is modified for fixed S and θ_{in}. A quantitatively similar picture can be obtained for a given fluid with fixed material parameters S and Q and a variation of the inlet temperature θ_{in}. If θ_{in} is such that $\eta_{in} \to 1$, heating does not influence the flow. In this case, the significant viscosity variation takes place outside

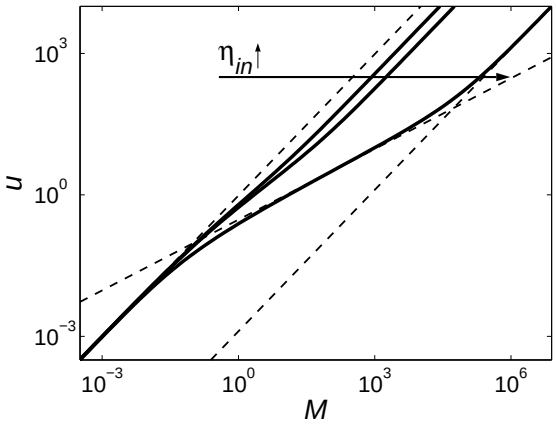

Figure 2.6: Velocity of a heated system with $P = S = \theta_{in} = 1$ and different material parameters $Q = 0, -0.425, -0.85$ leading to $\eta_{in} = 2.72, 5.69, 785.77$. The curves visualize how the set of parameters Q, S, θ_{in} influences the development of the nonlinear flow regime. For $\eta_{in} \to \infty$, a flow regime with $u \sim M^{1/2}$ develops between the two linear branches.

of the chosen temperature range. Furthermore, Fig. 2.6 visualizes that the wider the gap between the two linear branches of $u(M)$ becomes, the better the nonlinear branch develops.

Nonlinear flow we find for $\eta_{in} > 1$ with $M \sim u^b$, $1 < b \leq 2$ as the viscosity decreases for lower velocities. The upper bound of the branch $b = 2$ is formed because of the proportionality between the slope of the viscosity curve at the pipe entrance s and the velocity u. This case is reached if $(S\theta_{in} + Q) \to 0$ such that $\eta_{in} \gg 1$. For $\eta_{in} = 1$ the viscosity is constant for all velocities and no nonlinear flow can be observed at all, $b = 1$.

2.3.2 Heating with wall heat loss

We now turn to the discussion of results for a system with wall heat loss $N > 0$ and $Q = \theta_\infty = 0$. As soon as the assumption $N = 0$ is abandoned and the viscosity strongly depends on temperature, we discover a dramatic qualitative change in the behavior of the system. Indeed, Fig. 2.7(a) shows that for sufficiently strong heat loss the curve $u(M)$ ceases to be a monotonic function and bifurcations occur. The curve can again be divided into 3 branches. For large values of u, branch (3), the wall heat loss and Joule heat do not influence the temperature since the residence time in the pipe is too short. Due to the constant temperature the velocity u is proportional to M. The same is found for very small forces, as can be seen by inspecting branch (1) in Fig. 2.7(a). The reason for the linear behavior on branch (1) is similar to the case $N = 0$ but it involves a subtle difference resulting from the interplay between wall cooling and Joule heating. In this case the temperature decreases very fast at the entrance of the pipe. For a lower temperature the heat loss is reduced and the electrical heat production is enhanced due to a lower electrical conductivity until a temperature is reached, for which the generated heat and the lost heat are balanced. The constant pipe temperature in this branch does not depend

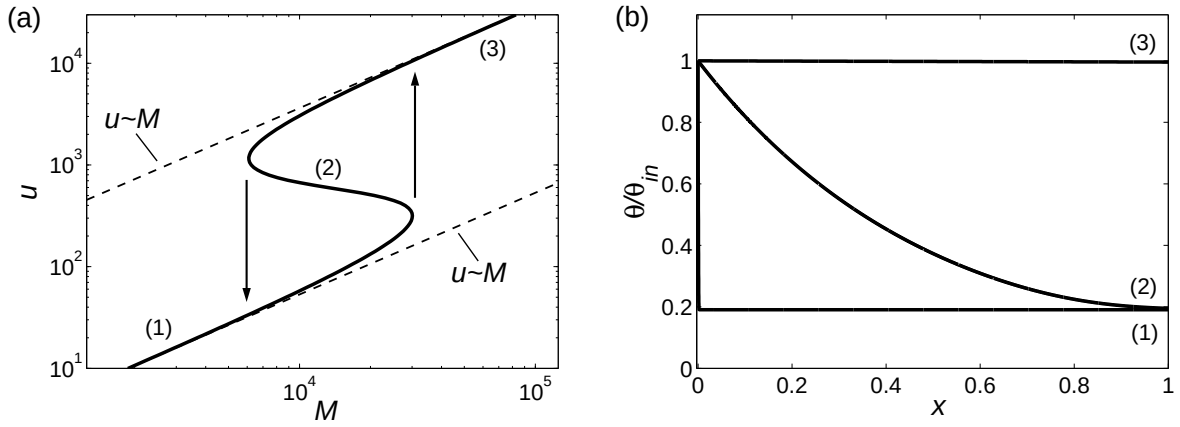

Figure 2.7: Flow regime for a pipe for the case $N = 1000$ when the wall heat loss exceeded a critical value $N_C = 52.2$ (remaining parameters: $P = S = \theta_{in} = 1$, $K = Q = 0$): (a) Velocity u as function of the forcing parameter M as obtained by solving Eqs. (2.8)-(2.9). The curve shows the development of a bifurcation and is divided into 3 branches: the stable branches (1) and (3) with $u \sim M$ and the unstable branch (2). (b) Representative relative temperature distribution $\theta(x)/\theta_{in}$ along the pipe axis x for every branch.

on the forcing parameter at all, as the left horizontal part of the curves with $N \neq 0$ in Fig. 2.8(b) shows. The constant pipe temperature just depends on the parameters P, N and θ_∞ according to $P/N \exp(1/\theta) = \theta - \theta_\infty$, see Eq. (2.9) with $d\theta/dx = 0$. Branch (2) is characterized by a continuously decreasing shape of $\theta(x)$, see Fig. 2.7(b), curve (2). Here, in contrast to branches (1) and (3), the velocity decreases with increasing forces. The reason is the temperature dependent viscosity. Indeed, a decreasing velocity leads to a decrease of the mean temperature, since the heat loss increases. The result is an increase of the mean viscosity and finally a significant increase of the driving force required to maintain the flow.

This mechanism of bifurcation, namely the effect of viscosity and temperature on the mean velocity, was already observed in previous studies, e.g. in [86], [30], [87]. But these studies consider systems which were cooled only, whereas heating was not included at all. Therefore, the lower stable branch obtained in these studies is not a result of balanced heating and cooling. There, branch (1) is reached as soon as the fluid temperature matches the ambient temperature. As a result the ambient temperature is the only parameter defining the fluid temperature and finally the flow rate for a given forcing parameter due to the temperature-dependent viscosity. Our studies show that additional heating gives a second control parameter for the fluid temperature and flow on the lower stable branch. Lange & Loch [48] have not observed the lower stable branch at all.

What would happen if we would experimentally analyze this flow? Let us therefore carry out a thought experiment. We start from branch (3) with a high force and reduce M until we reach the left inflexion point in Fig. 2.7(a). Instability will occur due to the fact that a small incidental reduction of u leads to a strong cooling. This, in turn, results in a greater viscosity and higher friction force, which reduces the velocity. The greater

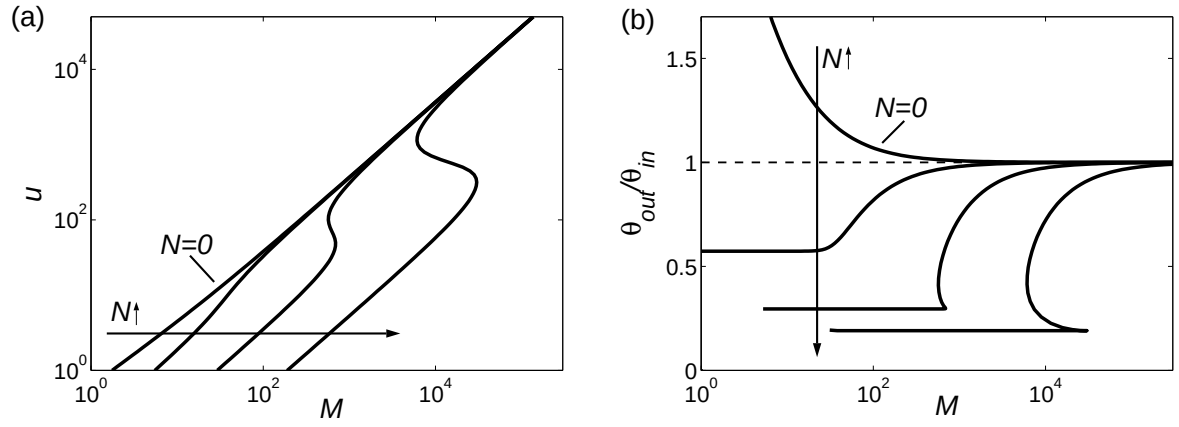

Figure 2.8: Influence of the wall heat loss parameter N: (a) Velocity u as function of the forcing parameter M as solution of Eqs. (2.8)-(2.9) for different wall heat loss parameters $N = 0, 10, 10^2, 10^3$ (remaining parameters: $P = S = \theta_{in} = 1$, $K = Q = 0$). (b) Corresponding relative exit temperature θ_{out}/θ_{in} versus acting force M.

residence time intensifies the heat loss which causes an amplification of the slowdown process. This self-induced process stops when the heat loss is equal to the increasing heat production due to the decreasing electrical conductivity of the fluid. This process appears as a jump from branch (3) to branch (1) as indicated by the left arrow in Fig. 2.7(a). We can also carry out a reverse thought experiment starting with a low force and increasing it until the right inflexion point is reached. At this point, due to the lower residence time, the fluid does not cool down immediately. Heat production and wall heat loss are not balanced anymore. With the decreasing viscosity the velocity increases which reduces the heat loss and amplifies the acceleration process. This process stops when the temperature becomes constant along the pipe and appears as a jump from branch (1) to branch (3). As already studied in [87], branch (2) is unstable in contrast to branches (1) and (3).

In Fig. 2.8 the transition from a system without heat loss to a system with heat loss for various heat loss parameters N and constant heat production is shown. A quantitatively identical picture could be given for constant heat loss and different heating parameters P. This fact nicely confirms that the temperature on the lower branch is determined by the balance of heating and cooling, see Fig. 2.8(b), left part of the curves. The higher N the lower the temperature and the lower the mean viscosity. A higher force is necessary to reach a certain velocity, as shown by the lower part of the curves in Fig. 2.8(a).

Fig. 2.9 summarizes the behavior of the system in the two-dimensional space of the control parameters $(N/P, M/P)$. Within the marked space to the right of the critical value N_C/P multiple solutions do coexist. The upper (lower) boundary of this parameter region marks the value of M for which the solution jumps from one mode to the other when M is increased (decreased). Above the upper boundary one solution of the fast mode with a constant temperature distribution exists. Below the lower boundary one solution of the slow mode with a constant temperature distribution exists due to balanced heat loss and heat production.

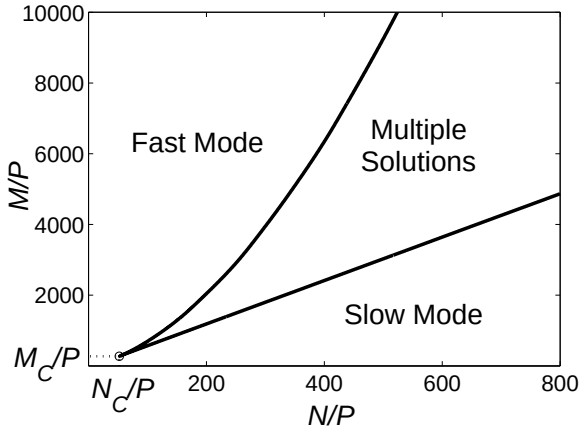

Figure 2.9: Phase diagram of laminar non-isothermal pipe flow with strongly temperature-dependent viscosity and electrical conductivity showing the different regimes as a function of the P-scaled forcing parameter M/P and the P-scaled cooling parameter N/P with $S = \theta_{in} = 1$ and $K = Q = 0$. For $N/P > N_C/P$ the parameter space is divided into three domains: (i) fast domain with constant temperature for high forces, (ii) multiple solutions coexist, (iii) slow domain with constant temperature for small forces.

2.3.3 Influence of diffusion

With heat diffusion, $K > 0$, a uniformization of the temperature takes place which smears out the temperature along the x-axis for low and moderate velocities. For low velocities conduction is the dominating heat transport mechanism whereas heat convection is negligible. In this case the temperature distribution is virtually independent of the velocity. Consequently, the balance between heat production, heat loss and diffusion gives rise to a linear flow, $u \sim M$.

For a system without cooling the mean temperature decreases with raising K (see Fig. 2.10(b)) and the mean viscosity increases. This results in a higher force M for a given velocity u as shown in Fig. 2.10(a). The branch with nonlinear flow regime is shortened. For a system with dominating cooling the viscosity decreases and leads to a smaller force M for a given velocity u, see Fig. 2.11. In general, diffusion reduces the parameter range of M leading to multiple solutions. If a certain critical value K_C is exceeded, bifurcations disappear altogether. Both figures reveal that for very high diffusion the temperature remains constant $\theta(x) = \theta_{in}$ and leads to linear laminar flow $u \sim M$ for all velocities.

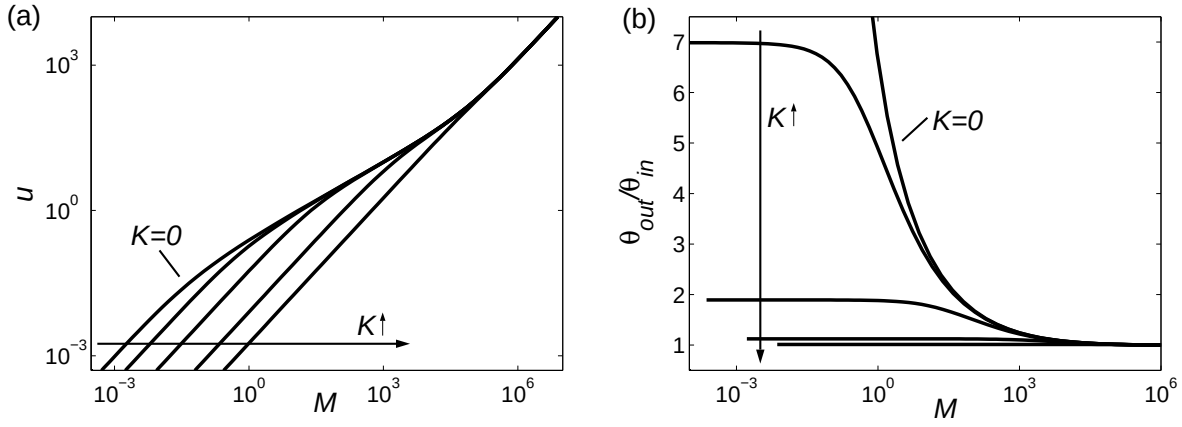

Figure 2.10: Influence of the heat diffusivity parameter K on the flow in a pipe without wall heat loss: (a) Velocity u as function of the force M as solution of Eqs. (2.8)-(2.9) for different diffusion parameters $K = 0, 0.1, 1, 10, 100$, a heating parameter $P = 1$ and $N = 0$, $S = \theta_{in} = 1$, $Q = -0.85$. (b) Corresponding relative exit temperature θ_{out}/θ_{in} versus acting force M.

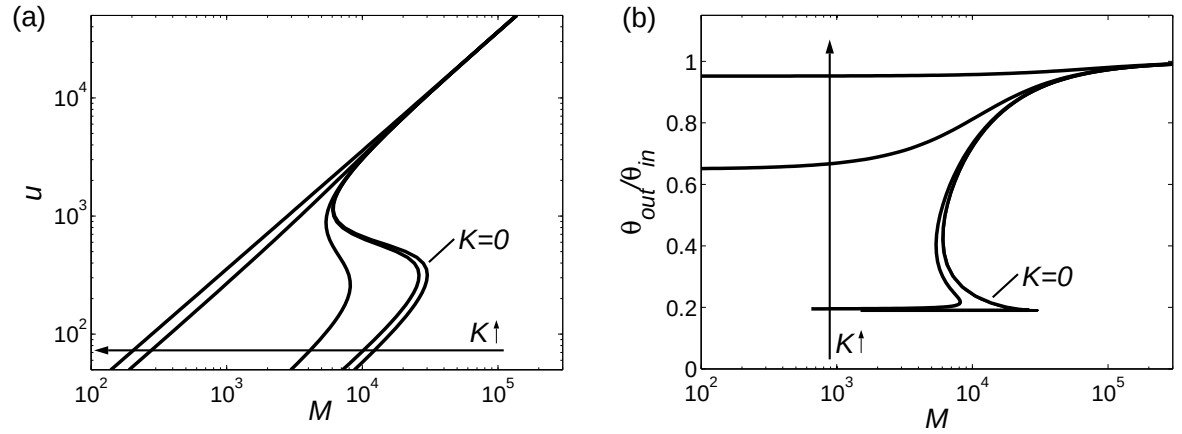

Figure 2.11: Influence of the diffusion parameter K on a system with wall heat loss: (a) Velocity u as function of the force M as solution of Eqs. (2.8)-(2.9) for different diffusion parameters $K = 0, 10, 10^2, 10^3, 10^4$, a constant heat loss parameter $N = 1000$ and $P = S = \theta_{in} = 1$, $Q = \theta_\infty = 0$. (b) Corresponding relative exit temperature θ_{out}/θ_{in} versus acting force M.

2.3.4 Sample calculations with glass melt parameters

In order to verify the usage of Lorentz forces to control glass melt flow in a pipe, we performed calculations with real glass melt parameters. We have chosen two glass types, namely *glass 1* as a standard glass used for neutral-glass tubing for pharmaceutical packaging and *glass 2* as an example for glass that is used for high-temperature applications [66]. In the temperature range from 1200 ^{o}C to 1600 ^{o}C the two glasses differ strongly in their temperature-dependence of the material parameters, see Tab. A.2. The viscos-

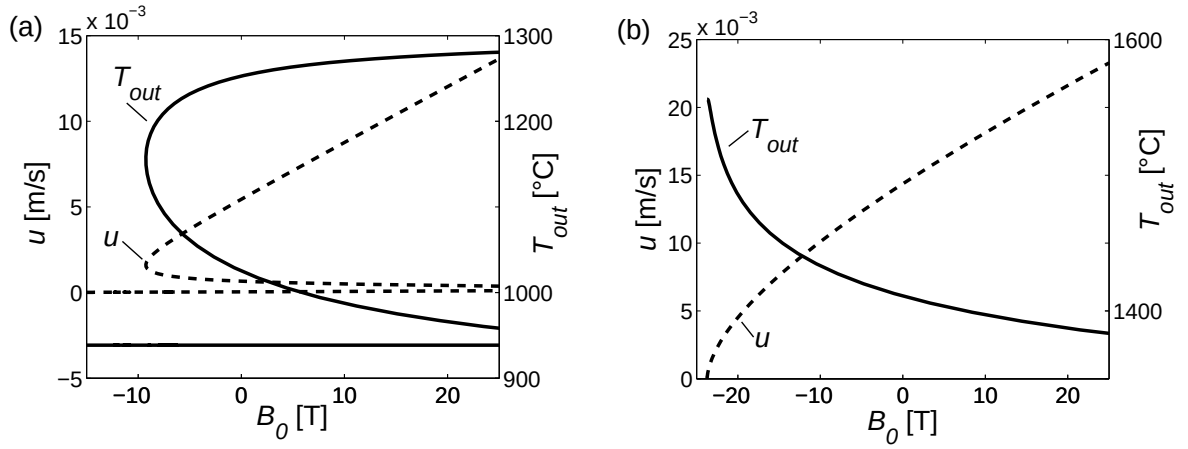

Figure 2.12: Example calculation for velocity u in m/s and exit temperature T_{out} in K as function of the magnetic field density B_0 in T for (a) *glass 1*, and (b) *glass 2* with the thermophysical properties listed in Tab. A.2 and the following set of parameters: $J_0 = 10^3$ A/m^2, $h = 10$ W/m^{2}K, $T_{in} = 13004$ ^{o}C, $T_\infty = 20$ ^{o}C, $L = 1$ m, $R = 0.025$ m. For *glass 1* heat loss dominates and bifurcation occurs. Due to the low electrical conductivity of *glass 2* heat production dominates and the solution is unique.

ity of *glass 1* varies between 700 Pas and 25 Pas and the electrical conductivity varies between 4.2 S/m and 12.6 S/m. *Glass 2* is characterized by a viscosity decrease from 2110 Pas to 6.5 Pas and a very low electrical conductivity, increasing from $2.6 \cdot 10^{-2}$ S/m to 1.2 S/m. The calculations have been performed for the following common parameters: $J_0 = 10^3$ A/m^2, $h = 10$ W/m^{2}K, $T_{in} = 1300$ ^{o}C, $T_\infty = 20$ ^{o}C for a pipe with a length of $L = 1$ m, and a radius of $R = 0.025$ m.

With this set of parameters, the wall heat loss dominates for *glass 1* and leads to bifurcation as shown in Fig. 2.12(a). If we assume an operating range of $-3\text{T} \leq B_0 \leq 3\text{T}$ the velocity of the upper stable branch can be controlled between $4.4 \cdot 10^{-3}\text{m/s} \leq u \leq 6.5 \cdot 10^{-3}$ m/s. It enables a continuous fine tuning of the mass flow rate. At the lower branch the fluid has a low constant temperature and is almost immobilized. In accordance with the theoretical results of the previous section, the velocity of these two branches varies linearly with the external magnetic field. Due to the low electrical conductivity of *glass 2* the heat production dominates and no bifurcation occurs as shown in Fig. 2.12(b). The heat production is so large that the temperature increases by more than 100 K. In order to cool the melt the applied current density can be reduced. It would lead to a small, almost negligible Lorentz force density in the melt. Alternatively the cooling of the system can be increased with an additional cooling system to balance the heat production. In both cases, however, bifurcation occurs if the cooling rate is strong enough.

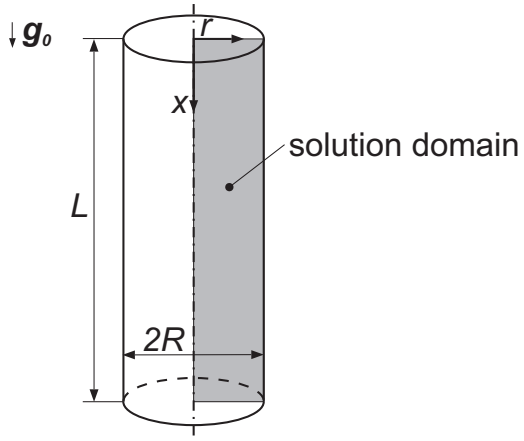

Figure 2.13: Sketch of the considered problem (not to scale). The solution domain of the two-dimensional axisymmetric simulation is highlighted by the grey shaded area.

2.4 Validation by numerical simulation

The analytical one-dimensional (1d) pipe flow model presented in the previous sections describes the variables only as function of the coordinate x, e.g. the mean viscosity is calculated exclusively with the mean temperature. Radial effects are neglected. The present two-dimensional (2d) axisymmetric simulations using the commercial software package Comsol, however, predict the dependence of u and T on two coordinates, namely the streamwise coordinate x and the radial coordinate r. As a result, a temperature- and viscosity-profile are established at every x by the additional consideration of the dependence on r. The goal of the present section is to study the effect of r on the flow and to validate the results of the 1d pipe flow model.

2.4.1 Implemented model and method

Fig. 2.13 pictures the considered pipe including the the solution domain of the two-dimensional axisymmetric simulations. We solve in Comsol the steady and incompressible Navier-Stokes equation

$$\rho_0 \mathbf{u} \cdot (\nabla \mathbf{u}) = -\nabla p + \nabla \cdot \{\eta(T)[\nabla \mathbf{u} + (\nabla \mathbf{u})^T]\}, \tag{2.17}$$

the condition of incompressibility

$$\nabla \cdot \mathbf{u} = 0, \tag{2.18}$$

and the stationary energy equation

$$\rho_0 c_P (\mathbf{u} \cdot \nabla) T = \lambda_0 \nabla^2 T + \frac{J_0^2}{\sigma(T)}. \tag{2.19}$$

With the mean velocity u_m and the constant inlet temperature T_{in} we specify the following boundary conditions

$$u_x = 2u_m \left(1 - \left(\frac{r}{R}\right)^2\right), \quad u_r = 0, \quad T(0, r) = T_{in} \text{ for } x = 0, \tag{2.20}$$

$$u_x = 0, u_r = 0, -\lambda \partial T/\partial r = h(T - T_\infty) \text{ for } r = R. \tag{2.21}$$

The remaining velocity and thermal boundary conditions are chosen to correspond to the physical model, i.e. no-slip and convective boundary condition at the pipe wall, symmetry boundary condition at $r = 0$, and convective outflow conditions at $x = L$.

First of all, we like to emphasize that the velocity field $\mathbf{u} = u_r(x, r)\mathbf{e_r} + u_x(x, r)\mathbf{e_x}$ is not only a function of the radial coordinate r. As the viscosity is a function of the temperature and therefore depends both on r and x, the velocity $\mathbf{u}$ depends on the axial position as well, e.g. $\mathbf{u} = \mathbf{u}(x, r)$. As a result the flow is not fully developed. Furthermore, the Navier-Stokes equation (2.17) does not include the Lorentz force and the gravitational force like the analytical model which is described in Sec. 2.1. These driving forces are substituted by a driving pressure gradient ∇p according to

$$\nabla p = \rho_0 \mathbf{g} + \mathbf{J_0} \times \mathbf{B_0}. \tag{2.22}$$

It enables us to define a parabolic velocity profile at the pipe inlet and to obtain as solution a driving pressure gradient. Therefore, we can access easily all stable and unstable branches of the multi-valued solutions we observed in Sec. 2.3.2.

To compare the numerical results with the results of the analytical model we mainly consider the temperature at the outlet T_{out} and the pressure difference between the inlet and the outlet of the pipe Δp, which is

$$\Delta p = L \nabla p. \tag{2.23}$$

As the flow is not fully developed, the pressure can vary over the cross-section and an integration at the in- and outlet is carried out to determine the mean pressure difference as follows

$$\Delta p = \frac{2}{R^2} \left(\int_0^R p(r, 0) r dr - \int_0^R p(r, L) r dr \right). \tag{2.24}$$

A similar definition applies for the cross-section averaged temperature at the outlet:

$$T_{out} = \frac{2}{R^2} \int_0^R T(r, L) r dr. \tag{2.25}$$

The multiphysics tool Comsol uses the finite element method to solve partial differential equations [10]. We use the direct solver Umfpack with a relative accuracy of 10^{-6}. The mesh is unstructured with a total of 4,480 basic net elements, whereas the border areas of the cylinder have a more detailed resolution. We checked our numerical model by calculating the mean velocity for a given pressure difference for an isothermal case. The result is identical to that obtained with the law of Hagen-Poiseuille [85].

In our studies the current density J_0, the heat transfer coefficient h, and the ambient temperature T_∞ are varied to verify the validity of the one-dimensional model in a wide range of parameters. The calculations are carried out for *glass 1* – SCHOTT glass nb. 8412 – with the material properties given in Tab. A.2. The examined pipe has a radius of $R = 0.025$ m, a length of $L = 0.5$ m, and an inlet temperature of $T_{in} = 1573.15$ K.

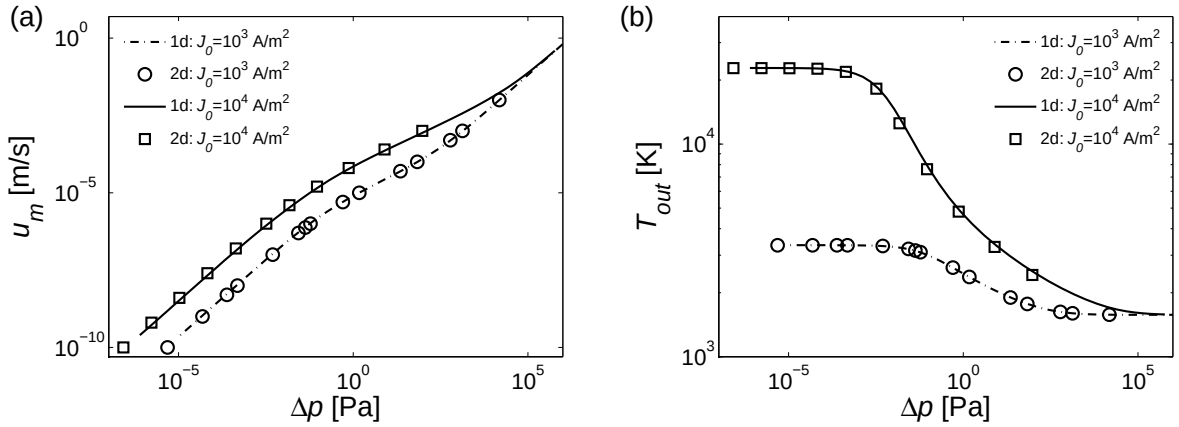

Figure 2.14: Results for heating without cooling: (a) mean velocity at the inlet u_m, and (b) mean temperature at the outlet T_{out} as functions of the driving pressure difference Δp. The markers label the numerical solutions and the lines are the solutions of the analytical model. For both applied current densities the results of both strategies are indeed in a very good agreement.

2.4.2 Results

First we examine a system with volumetric heat input due to the Joule effect and without cooling, $h = 0$ W/m^{2}K. The dependence of the mean inlet velocity u_m and mean outlet temperature T_{out} on the mean applied pressure difference Δp is shown in Fig. 2.14. We performed two analysis for $J_0 = 10^3$ A/m^2 and $J_0 = 10^4$ A/m^2, respectively. The comparison of the simulation results (markers in Fig. 2.14) with the results obtained with the one-dimensional model (lines in Fig. 2.14) shows a very good agreement. This is due to the fact that the Joule heating warms up the fluid homogenously and according to that the dependence of the temperature on r is weak. Therefore, the radial variation of η is small and the mean viscosity of the 2d simulation and the 1d model coincide.

In the next paragraph we turn to a system with cooling, $h = 10$ W/m^{2}K, and without heating, i.e. $J_0 = 0$ A/m^2. In doing so, we vary u_m as well as the ambient temperature T_∞ and calculate the mean pressure difference Δp between the inlet and the outlet and the mean outlet temperature T_{out}. The results are shown in Fig. 2.15. For a high ambient temperature of $T_\infty = 1173.15$ K we observe a pressure range in which one pressure value can be assigned to three different velocities. For a low ambient temperature of $T_\infty = 293.15$ K a double-valued solution exists. There is a minimum pressure difference Δp at which one pressure difference Δp matches unambiguously with one velocity u_m. For very small pressure differences the strong cooling leads to $T \to |B|$. As a result we have $\eta \to \infty$, see Eqs. (1.6), and no numerical solution of the governing equations (2.17)-(2.19) exists at all. Hence, the lower branch of the curve is missing. Fig. 2.15 further shows that the results obtained with the two models are in a good agreement. For the high ambient temperature the quantitative agreement is particularly noteworthy. The difference between the results of the simulations and the analytical modeling for the cooling temperature $T_\infty = 293.15$ K originates from the radial variation of the temperature

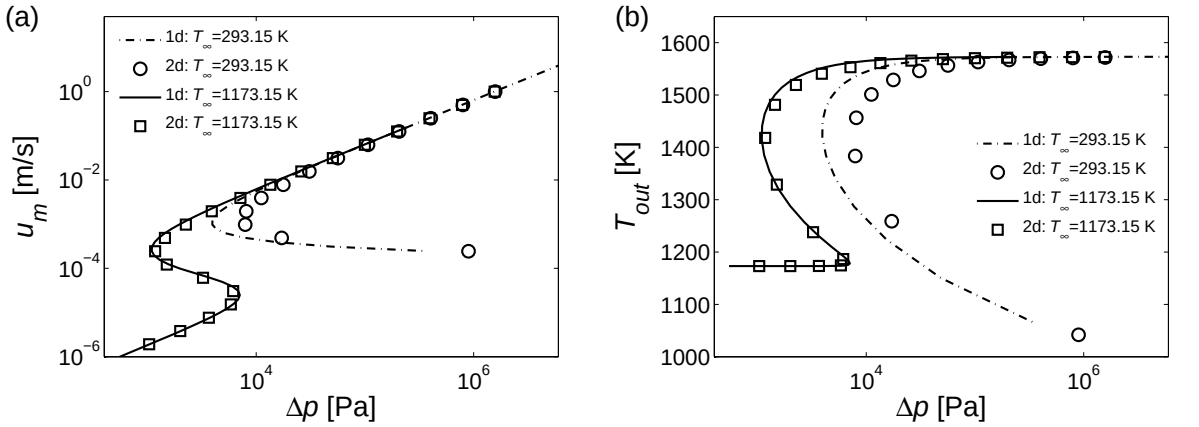

Figure 2.15: Influence of various ambient temperatures T_∞ for cooling without heating: (a) u_m, and (b) T_{out} as functions of Δp. For $T_\infty = 1173.15$ K the analytic and numerical results agree very well. In the case of $T_\infty = 293.15$ K the results of both strategies differ for moderate and small u_m, mainly close to the turning point.

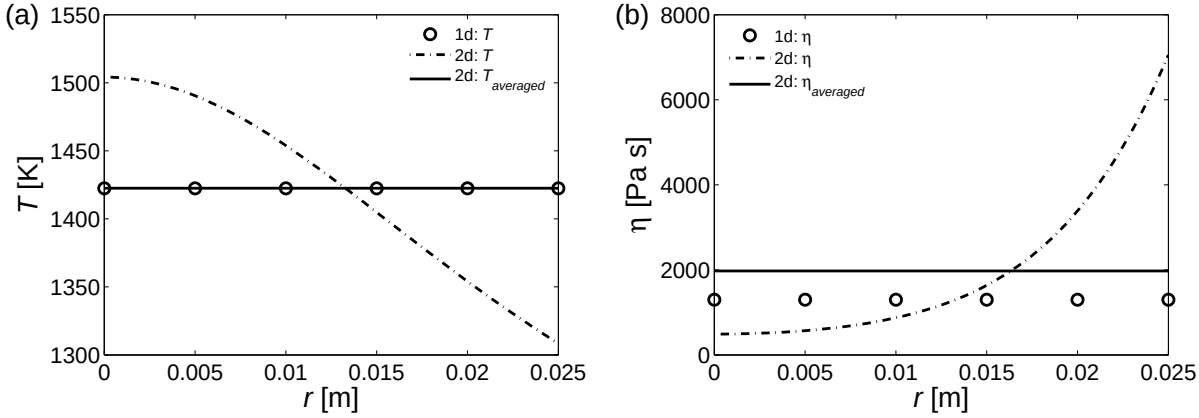

Figure 2.16: (a) Radial temperature profile, and (b) radial viscosity profile at the pipe outlet $x = L$ for $u_m = 10^{-3}$ m/s, $J_0 = 0$ A/m^2, $h = 10$ W/m^{2}K, and $T_\infty = 293.15$ K. Even though the mean temperatures obtained with the simulation and analytic model are identical, the exponential dependence of η on T leads to a significant larger mean viscosity in the simulation.

and finally the radial variation of the viscosity. In the 1d model the viscosity is calculated for the mean temperature, whereas in the 2d simulation the complete radial temperature distribution and the non-linear temperature-dependent viscosity in radial direction is considered. Fig. 2.16(a) shows that for a given velocity of $u_m = 10^{-3}$ m/s the outlet temperature predicted by the 1d model is equal to the mean outlet temperature obtained with the 2d simulation. However, in the simulation the strong cooling at the pipe wall has a significant influence. As the viscosity increases exponentially with decreasing temperature, the viscosity in the vicinity of the wall increases much more than with a linear temperature dependence. Consequently, the mean viscosity in the simulation is higher than the mean

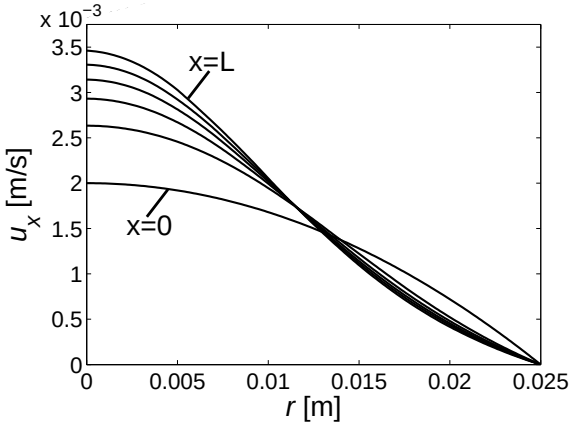

Figure 2.17: Radial profile of the axial velocity u_x at equidistant positions along the pipe axis including the inlet $x = 0$ and the outlet of the pipe $x = L$ for the case of cooling without heating with $u_m = 10^{-3}$ m/s, $T_\infty = 293.15$ K, and $h = 10$ W/m^{2}K. It pictures the modification of the flow profile due to large viscosities in the vicinity of the pipe wall.

viscosity in the 1d model as indicated in Fig. 2.16(b). For this reason a higher driving pressure difference Δp is necessary to obtain the same velocities as in the analytical 1d model. Therefore, the inflexion point is reached at a higher Δp in the 2d simulations. Because of the viscosity variation in radial and axial direction the velocity profile changes as well, see Fig. 2.17. It is readily seen that the prescribed parabolic velocity profile exists only at the inlet. With increasing cooling along the pipe axis – and hence an increasing viscosity at the pipe walls – the velocity at the edge decreases. In return, due to the condition of incompressibility the velocity increases towards the center of the pipe.

Now we deal with the general case of simultaneous Joule heating and wall cooling. In the process we vary the heat transfer coefficient h and keep all other parameters constant, i.e. the ambient temperature is set to $T_\infty = 293.15$ K and the current density is set to $J_0 = 10^3$ A/m^2. The results of the simulations are summarized in Fig. 2.18. For a heat transfer coefficient of $h = 1$ W/m^{2}K the influence of the heating is still stronger than that of the cooling. The dependence of u_m on Δp looks like the case of pure heating which we already discussed. If cooling dominates, $h = 10$ W/m^{2}K and $h = 50$ W/m^{2}K, multiple-valued solutions develop. Because of the additional heating we don't receive a two-valued solution like in the previous case. With increasing cooling of the fluid the bifurcation is more pronounced and the quantitative differences between the 2d simulation and the 1d model increases. The range in which one pressure value can be assigned to three velocities is much smaller in the 2d simulation than in the 1d model, as it can be seen in Fig. 2.18(a). An explanation for this behavior can be found in the strong cooling of the melt at the pipe wall and the accompanying increase of the viscosity, like in the case of cooling without heating.

Finally we study the general case involving cooling and heating with various heat conductivities λ_0. Again the ambient temperature is set to $T_\infty = 293.15$ K and the heat transfer coefficient is set to $h = 10$ W/m^{2}K. The heating of the fluid is accomplished by a current density of $J_0 = 10^3$ A/m^2. If we vary the heat conductivity λ_0 of the fluid, the flow

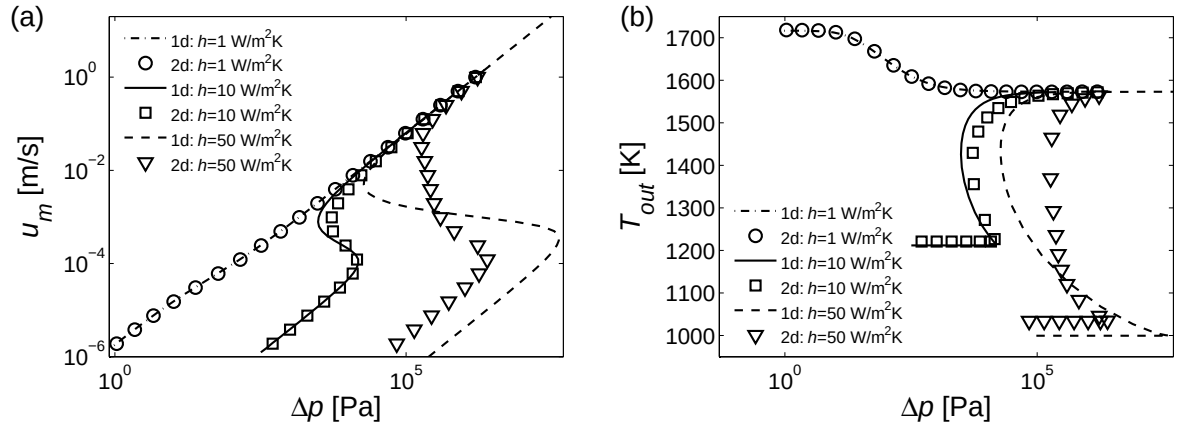

Figure 2.18: Influence of various heat transfer coefficients h for cooling and heating at the same time: (a) u_m and (b) T_{out} as function of Δp. The larger h – and hence the cooling rate – the more the solutions of both approaches diverge.

characteristics can change considerably as one can see in Fig. 2.19. In the 1d analytical model bifurcation develops if the conductivity is smaller than a certain critical value, i.e. $\lambda_0 < \lambda_{max}$. The smaller λ_0, the more distinct the bifurcation is. For $\lambda_0 = 0$ W/mK the pressure range for which one pressure value can be assigned to three velocities reaches its maximum. In contrast in the simulation we obtain a range $\lambda_{min} \leq \lambda_0 \leq \lambda_{max}$ for which the function $u_m(\Delta p)$ is not single-valued. For $\lambda_0 < \lambda_{min}$ and $\lambda_0 > \lambda_{max}$ every Δp can be assigned unambiguously to one u_m. For small values of λ_0 differences between the two approaches are obvious. The differences result from the assumption that the effects of the heat conductivity are only considered along the pipe axis x in the 1d model. Along the radial direction r the temperature is assumed to be constant and the 'radial' heat conductivity is infinity – independent of 'axial' heat conductivity λ_0. In contrast in the 2d simulation the heat conduction is acting in x- and r-direction. With increasing λ_0 the temperature profile flattens as shown in Fig. 2.20. If λ_0 has reached a certain value, the temperature in radial direction is almost constant and hence, fulfills the assumptions of the 1d model. In this regime the results of both models are in a very good agreement.

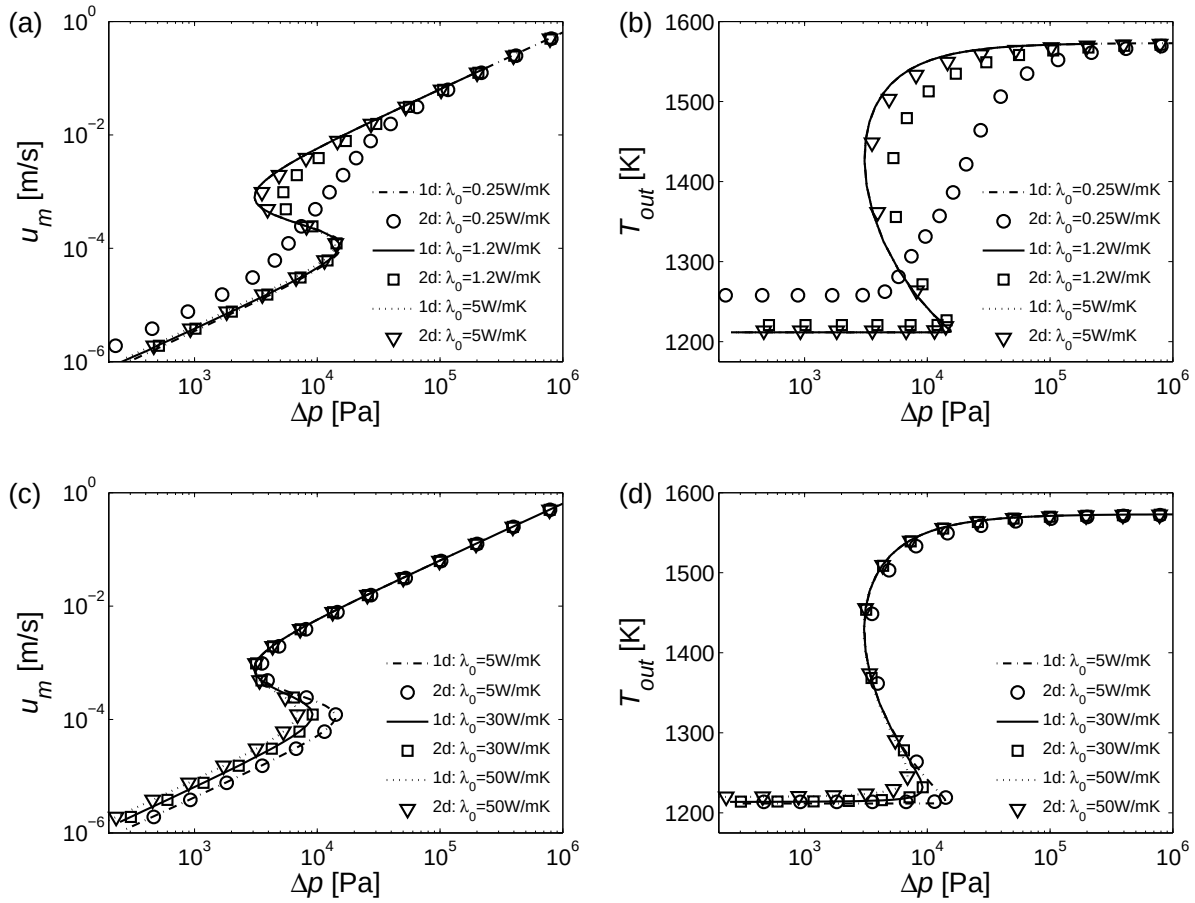

Figure 2.19: Influence of heat conductivity λ_0 for cooling and heating at the same time: (a), (c) u_m and (b), (d) T_{out} as function of Δp. For $\lambda_0 \gtrsim 5$ W/mK, (c)-(d), the results of both strategies are in excellent agreement. But for $\lambda_0 \lesssim 5$ W/mK, (a)-(b), the region of the three-valued solution increases and therefore agreement is left.

2.5 Simple experimental study of a non-magnetic case

In the following section we like to introduce a simple non-magnetic laboratory experiment of the non-isothermal pipe flow. We don't focus on an exact verification of the theory and a direct comparison. Our goal is to detect and measure the upper and lower branch of the multiple-valued solutions which we studied in Sec. 2.3.2.

2.5.1 Experimental setup and procedure

We use glycerin as working fluid which is common for so-called "cold experiments" of glass melt flows [70]. The advantage is that the dependence of the viscosity on temperature is comparable to that of glass melt at room temperature. Like in the numerical simulations we can approximate the driving Lorentz force and gravitational force by a pressure gra-

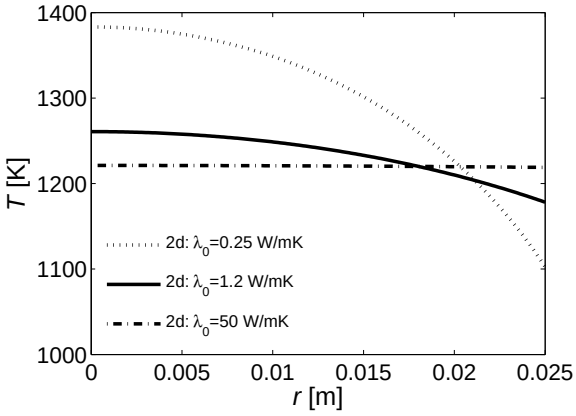

Figure 2.20: Radial temperature profile for various heat conductivities λ_0 and $u_m = 10^{-6}$ m/s, $J_0 = 10^3$ A/m^2, $h = 10$ W/m^{2}K, $T_\infty = 293.15$ K. For large λ_0 the temperature is constant over the cross section and corresponds to the assumptions of the analytical 1d model.

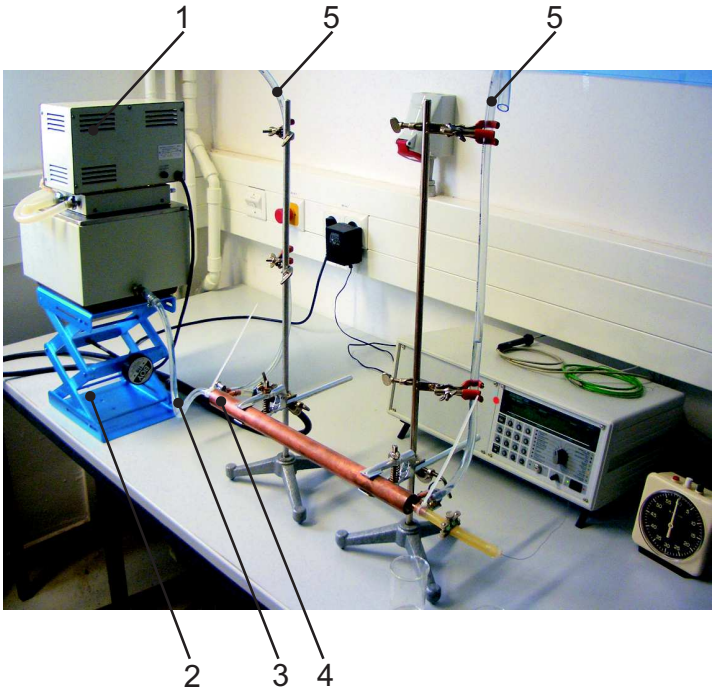

Figure 2.21: Experimental setup with 1 thermostat, 2 height adjustment, 3 flexible tube without heating jacked, 4 double pipe heat exchanger, and 5 head loss measurement.

dient along a horizontal pipe according to Eq. (2.22). Furthermore, the detection of the multiple-valued solutions just requires cooling and no direct electric heating (Heating is not restricted to direct electrical heating as it is used in the analytical model. In a simple experiment the heat can also be inserted over the wall. This procedure would not allow simultaneous heating and cooling). The configuration of the experiment is shown in Fig. 2.21. The heart of the experiment is the double-pipe heat exchanger made of copper.

The inner pipe represents our non-isothermal pipe flow with a length of $L = 0.4$ m and an inner radius of $R = 0.0025$ m. To ensure a maximum cooling rate at the inlet of the pipe the heat exchanger works in a parallel-flow arrangement. Water is used as cooling fluid and kept at an almost constant temperature T_∞. As cooper has a very high heat conductivity we can neglect the heat resistivity of the pipe wall and can assume that the convective boundary condition is fulfilled. At the inlet of the pipe we measure the temperature with a thermocouple to ensure a constant inlet temperature T_{in} of about 80^oC . The glycerin is heated in a thermostat and flows through a flexible tube to the pipe. Heat losses at the flexible tube are compensated by a heating jacked which is wrapped around the tube. The flow is driven by gravity by setting the thermostat at a given height. As the free surface of the liquid in the thermostat is large in comparison to the diameter of the pipe, and as we continuously return the outflow to the thermostat, we can assume a constant driving pressure.

The goal is to measure the temperature at the outlet T_{out} and the mean velocity u for a given pressure difference Δp. We determine the actual static pressure drop over the pipe with two liquid columns just before and just after the pipe. With the head loss h_f the pressure difference can be calculated easily according to $\Delta p = h_f g \rho$ with $\rho = \rho(T_{out})$. We use a thermocouple to measure the temperature at the outlet T_{out}. Like the thermocouple at the inlet we fix its tip in the center axis of the pipe by forming a spiral. The systematical measurement error of both thermocouples is ± 1.5 K. Furthermore we determine the mass of glycerin m which flows out in a certain time t to calculate the mass flow rate $\dot{m} = m/t$. We are able to measure the mass with an accuracy of ± 0.05 % and the time with an accuracy of ± 1 %. With $u = \dot{m}/(\pi R^2 \rho(T_{out}))$ we obtain the mean velocity of the flow in the pipe.

In experiments the bifurcation is reflected by a hysteresis in the graphs $u(\Delta p)$ and $T_{out}(\Delta p)$. For a given Δp we can reproduce the upper and the lower stable branches (indicated as (1) and (3) in Fig. 2.7), but we can not reproduce the unstable middle branch (indicated as (2) in Fig. 2.7). To detect both stable branches we use two different experimental procedures. The experiments for the lower stable branch start with a small driving pressure. Then the pressure is gradually increased and Δp, T_{out}, and $\dot{m}$ are recorded as soon as the system has settled at a steady state. At a steady state Δp is constant and the thermal conditions are adjusted. A couple of tests showed that the adjustment of thermal conditions requires approximately 30 minutes. For each measuring point the measured values of u and T_{out} are taken to be equal to the average of a finite sample of 10 repeat measurements. This procedure is repeated until the maximum possible driving pressure is reached. To record the data for the upper stable branch, the experiments started with the largest possible driving pressure which is then gradually decreased. For this procedure it is essential to avoid that the inlet temperature T_{in} becomes smaller than 80^oC as a lower inlet temperature supports the onset of the transition from the upper to the lower branch.

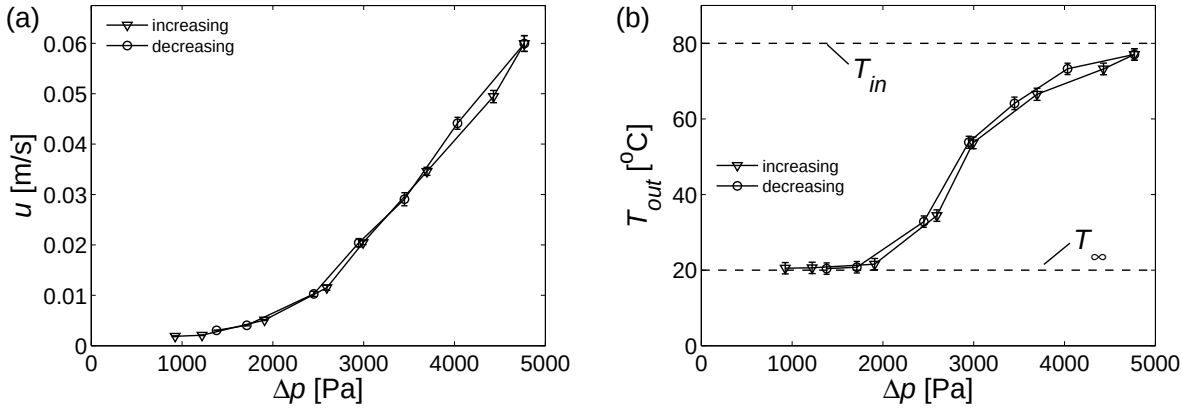

Figure 2.22: Measured data for a cooling temperature of $T_\infty = 20^o$C: (a) mean velocity u, and (b) outlet temperature T_{out} as functions of the pressure loss over the pipe Δp for $-\bigtriangledown-$ increasing and $-$o$-$ decreasing driving pressure. For the chosen cooling temperature we don't detect the desired regime of bifurcation.

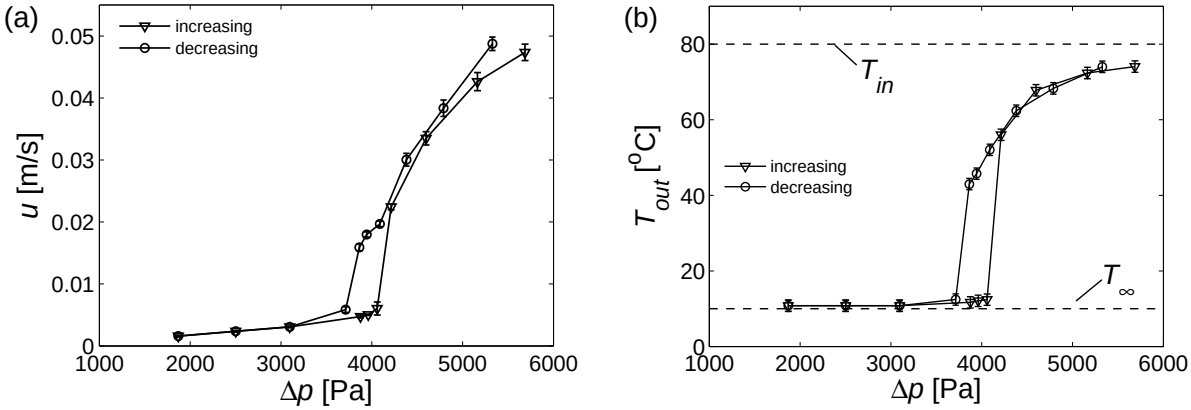

Figure 2.23: Measured date for a cooling temperature of $T_\infty = 10^o$C: (a) $u(\Delta p)$, and (b) $T_{out}(\Delta p)$. In a small band of about 300 Pa we are able to obtain two measuring values for one Δp. It shows that bifurcation exists for $T_\infty = 10^o$C and the prescribed conditions.

2.5.2 Results

The experiments are conducted for two cooling temperatures, namely $T_\infty = 20^o$C and $T_\infty = 10^o$C. The results are pictured in Figs. 2.22 and 2.23. For $T_\infty = 20^o$C it is particularly obvious that we do not measure two different mean velocities and two different outlet temperatures for one given Δp. The curves for an increasing and a decreasing driving pressure are almost identical. However, for $T_\infty = 10^o$C we get two measuring values for one Δp in a small band of about 300 Pa. As predicted by the theory, T_{out} of the lower branch is almost identical to the cooling temperature. Just after passing the lower inflexion point by slightly increasing Δp from 4060 Pa to 4200 Pa, T_{out} changes from

12^oC up to 56^oC. The transition from the upper to the lower branch is characterized by a significant jump of the outlet temperature as well. While decreasing Δp from 3860 Pa to 3710 Pa, T_{out} changes from 43^oC to 12^oC.

To our knowledge, the bifurcation based on temperature-dependent viscosity has been detected only by only Whitehead & Helfrich [86]. Whitehead & Helfrich got inspired by lava flow and used corn sirup as working fluid. Even though they observed the hysteresis, the experimental setup and procedure was quiet different. The syrup was driven by the filling height of a reservoir and flowed from the reservoir through a tube immersed in a chilled bath. The filling height of the reservoir oscillated with time. The oscillations produced a close curve in the height-velocity space indication the bifurcation as two-velocities could be obtained for one filling height.

2.6 Summary and discussion

We have formulated an one-dimensional analytical model which describes the interplay between friction force, gravity, Lorentz force, heat generation, heat loss, heat transport and heat diffusion in a circular pipe. The model takes into account the exponential temperature-dependence of the viscosity and the electrical conductivity. It is a simplified representation of electromagnetically controlled glass melt flow in a feeder. Our analysis reveals that the flow characteristics are strongly affected by the variation of the material parameters along the pipe. For a heated system without heat loss a variation within the temperature field leads to a velocity u which is not in general a linear function of the acting force M. If the viscosity at the pipe entrance has not reached the lowest possible value $\eta_{in} > 1$, we found a non-linear flow regime such as $u^b \sim M$ with $1 < b \leq 2$. For a system with additional dominating heat loss three velocities for one given driving force can be observed. The velocity ceases to be a single valued function of the acting force and bifurcations exist for a wide range of parameters. Three regimes allow the fluid to have constant material parameters and therefore lead to a known laminar flow characteristic with linear proportionality between the velocity and acting force $u \sim M$: (i) the velocity is high, the residence time within the pipe and therefore the temperature change is low; (ii) the temperature is very high so that the viscosity reaches its lowest possible value; (iii) the heat loss and heat generation are balanced.

We have validated the one-dimensional model with two-dimensional axisymmetric simulations using the commercial software Comsol. For heating without cooling we found a very good agreement between the results of both approaches. The monotonic, non-linear flow behavior has been predicted correctly by the one-dimensional model. The bifurcation, which develops for dominating cooling, has been reproduced by both methods. But for this case we found quantitative differences which are a result of larger temperature gradients and the non-linear increase of the viscosity with decreasing temperature. Furthermore, the two-dimensional simulations showed an excellent quantitative agreement with the prediction of the analytical model for moderate and high heat conductivities λ_0. For this case the temperature is almost constant along the cross section in the simulations and therefore fulfils an important assumption of the analytical model. However, for low

heat conductivities differences develop. In the one-dimensional model bifurcation exists for all $\lambda_0 \leq \lambda_{max}$. But in the simulations bifurcation also disappears for very small λ_0. Here, bifurcation exists only in a limited range with $\lambda_{min} \leq \lambda_0 \leq \lambda_{max}$. Additionally, we conducted a simple non-magnetic laboratory experiment to measure the stable branches of the bifurcation.

During our studies of the presented model we focused on the description and explanation of the new laminar flow characteristics. We did not particularly emphasize the importance of the results for the flow control. Now we will catch up on this briefly. To increase the velocity of a heated system by factor a, the driving force has to be increased by factor a^b with $1 \leq b \leq 2$. In this regime the change of forces is higher than for linear laminar flow. The observed bifurcation for a system with dominant cooling provide a new way of flow control. In the vicinity of the two inflexion points a weak change of the acting force leads to a significant change of the velocity. The coexistent temperature jump which is the reason for the bifurcation may lead to significant and unintended material changes. However, we observed that one stable branch is reached for a balance of cooling and heating. Hence, the heating can be used to control the position of the lower stable branch. This mechanism enables the active external regulation of the development of the bifurcation and therefore the characteristics of the temperature and velocity jumps in the vicinity of the inflexion points. Furthermore, we identified various regimes in which the velocity is a linear function of the driving force - hence the imposed Lorentz force. This linear functionality allows for a precise and simple electromagnetic control of the glass melt flow.

3 Electromagnetically controlled flow in a crucible

Now we leave the subject of electromagnetically controlled forced convection in a pipe and concentrate on free convection in a small scale crucible which is influenced by the imposed Lorentz force. The electromagnetically controlled free convection is relevant for glass processing as it provides new possibilities to increase mixing and to improve the temperature homogenization. We consider a setup which was used for experimental studies by Krieger and co-workers [35], [42]. They have visualized the flow pattern and have proven the influence of the imposed Lorentz force e.g. by temperature measurements at a limited number of positions within the melt. However, the experiments are not able to answer the following questions: How is the transition from a purely buoyant driven flow to a mainly Lorentz force driven flow characterized and how are the flow pattern and temperature distribution influenced by the Lorentz force? Moreover, one would like to know the scale relations between the velocity, temperature, and Lorentz force and whether the temperature-dependent material properties of glass melts influence the flow characteristic. In the following we will give answers to these questions by means of three-dimensional (3d) numerical parameter studies in Sec. 3.1 and one-dimensional (1d) analytical modeling in Sec. 3.2. In Sec. 3.3 we perform some sample calculations to compare the numerical, analytical, and experimental results.

3.1 Three-dimensional numerical simulation

The present approach is to study systematically the electromagnetically controlled thermal convection of glass melt in a small scale cylindrical crucible. The current density is generated by two rod electrodes, which are immersed into the melt. Therefore, papers on mathematical modeling of electric furnaces are relevant for our numerical studies, which number is limited. In the following we will briefly introduce these papers. In his pioneering work Curran [12] studied the effects of different electrode configurations in a 2d model followed by Austin & Bourne [1], and Mardorf [50] who included a feeding rate of the batch. Chen & Goodson [6] presented 3d results assuming constant material properties except in the buoyancy term. Between 1986 and 1988 some papers about 3d simulations of industrial all-electric furnaces were published [7], [78] [79], [80], [8]. The authors of these papers focused on the arrangement and orientation of multiple electrodes. Furthermore, they included the pull rate of the batch and the temperature-dependent material properties. Due to the limited computational power at that time the grid refinement was extremely limited. With combined experimental and three-dimensional numerics Hiejima

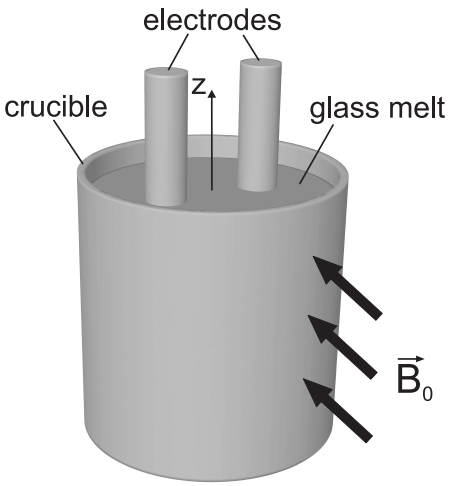

Figure 3.1: Sketch of the considered problem (not to scale).

[31] studied the possibilities to control the glass convection with various electric boosting conditions, heat loss through the walls, and the charged glass batch. Recently, the setup of a small scale cylindrical crucible was modeled numerically by Cepite and co-workers in [5]. The authors used idealized and unrealistic thermal boundary conditions to meet the experimental data of [35], [42]. Even more, they did not perform any systematic variations of the Lorentz force magnitude and can not give any answer to the questions we just posed.

3.1.1 Formulation of the problem

The small scale crucible which we consider is sketched in Fig. 3.1. The inner radius of the laboratory crucible is $R = 0.04$ m and the fill level of the molten glass is $H = 0.08$ m. Two rod electrodes with a diameter of $D = 0.013$ m are symmetrically immersed 0.06 m into the melt from the top at $(x, y) = (-0.0165 \text{ m}, 0 \text{ m})$ and at $(x, y) = (0.0165 \text{ m}, 0 \text{ m})$. The prescribed setup has two symmetry planes, namely the plane $x = 0$ m and the plane $y = 0$ m which are shown in Fig. 3.2.

The glass melt is assumed to be Newtonian with a constant heat capacity c_P and the viscosity $\eta(T)$ and the electrical conductivity $\sigma(T)$ being exponential functions of the temperature T according to Eqs. (1.6) and (1.7), respectively. Furthermore, the density $\varrho(T)$ is assumed to be a linear function of the temperature and the heat conductivity $\lambda(T)$ is approximated by a quadratic function of the temperature.

Between the electrodes a constant electric potential difference U_E is applied. As a result we obtain a current density distribution $\mathbf{J}$ which is heating the melt due to the Joule effect with the volumetric heat input J^2/σ. As we have heat losses at the surface and the crucible walls, temperature and density gradients develop in the melt. Thus, with the

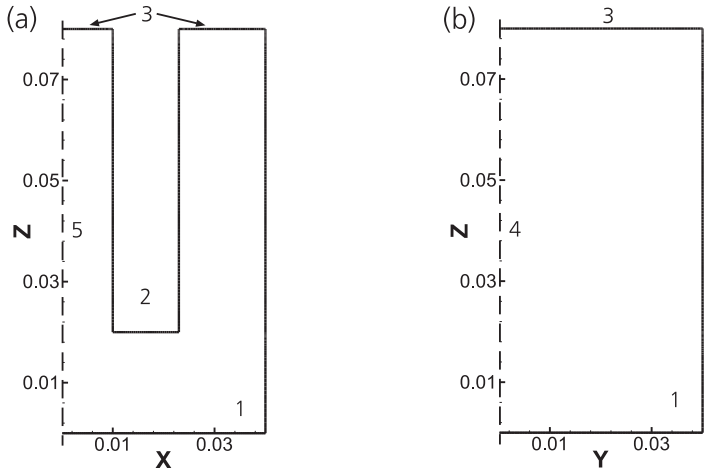

Figure 3.2: Views of the symmetry planes of the glass bath at (a) $y = 0$ m, and (b) $x = 0$ m with 1 being the crucible wall, 2 the electrode surface, 3 the free surface of the melt, 4 the symmetry plane $y = 0$ m, and 5 the symmetry plane $x = 0$ m.

acceleration of gravity $\mathbf{g} = g\mathbf{e_z}$, the gravitational force

$$\mathbf{f_b} = \varrho g \mathbf{e_z},$$

leads to buoyancy which is driving the flow. Such buoyancy driven convection is the basis of so-called all-electric furnaces and already well studied. In this chapter we focus on the question, how thermal convection can be influenced by Lorentz forces $\mathbf{f_L}$. In practical applications one would like to know, how the homogeneity or mixing rate can be improved with such an additional force. To generate Lorentz forces we suppose that a homogenous and steady magnetic flux density $\mathbf{B_0} = B_0\mathbf{e_y}$ is given for the whole crucible as indicated in Fig. 3.1. With the definition of $\mathbf{B_0}$ the imposed Lorentz force simplifies to

$$\mathbf{f_L} = f_{Lx}\mathbf{e_x} + f_{Lz}\mathbf{e_z} = J_z B_0 \mathbf{e_x} - J_x B_0 \mathbf{e_z}. \tag{3.1}$$

Hence, we have one Lorentz force component acting in $\mathbf{e_x}$-direction and one component acting in $\mathbf{e_z}$-direction, namely f_{Lx} and f_{Lz}. The model for constant U_E and B_0 holds also for a low frequency electric potential and a magnetic flux density of the same frequency as the skin depth is large in comparison to the crucible dimensions at low frequencies. Low frequency electromagnetic fields would be used in practice to minimize corrosion.

In our considerations we neglect effects of induced currents and viscous heating which is usually valid for the flow of glass melts. To estimate these effects we take the following parameter values: $\sigma_0 \sim 1 - 10$ S/m, $\eta_0 \sim 1 - 10$ Pas, $\lambda_0 \sim 1$ W/mK, $c_P \sim 1000$ J/kgK, $\rho_0 \sim 3000$ kg/m^3, a thermal expansion coefficient of $\beta \sim 10^{-4}$ 1/K, a typical length scale of $L_0 \sim 0.04$ m, a typical velocity of $u_0 = 10^{-4} - 10^{-2}$ m/s and a typical temperature difference of $\Delta T \sim 100$ K. For this scales the induced currents $\sigma(\mathbf{u_0} \times \mathbf{B_0})$ are negligible because of a small Hartmann number

$$\mathrm{Ha} = B_0 L_0 \sqrt{\frac{\sigma_0}{\eta_0}} \ll 1,$$

which describes the ratio between induced electromagnetic force and the friction force [14]. The viscous heating is negligible compared to the heat conduction since the ratio of both, the Brinkman number, is

$$\mathrm{Br} = \frac{\eta_0 u_0^2}{\lambda_0 \Delta T} \ll 1.$$

Furthermore, we do not take into account internal radiative heat transfer as the considered glass is almost completely non-transparent even for thin layers.

During our studies we only model the glass bath and assume laminar and steady flow. This assumption is valid due to the Rayleigh number Ra of the system, which is

$$\mathrm{Ra} = \frac{g\beta\Delta T L^3 \rho_0^2 c_P}{\eta_0 \lambda_0} < 10^5.$$

The three-dimensional steady flow is governed by the mass conservation equation

$$\nabla \cdot (\varrho \mathbf{u}) = 0, \tag{3.2}$$

and the Navier-Stokes equation

$$\nabla \cdot (\varrho \mathbf{u}\mathbf{u}) = -\nabla p + \nabla \cdot \left[\eta \left(\nabla \mathbf{u} + \nabla \mathbf{u}^T\right)\right] + \varrho g \mathbf{e_z} + (J_z \mathbf{e_x} - J_x \mathbf{e_z}) B_0, \tag{3.3}$$

with the following boundary conditions

$$\mathbf{u} = 0 \quad \text{at the electrodes and crucible wall,} \tag{3.4}$$

$$\mathbf{u} \cdot \mathbf{n} = 0, \quad \nabla(\mathbf{u} \cdot \mathbf{t}) \cdot \mathbf{n} = 0 \quad \text{at the free surface,} \tag{3.5}$$

where $\mathbf{n}$ denotes the normal vector, and $\mathbf{t}$ the tangential vector of the considered boundary faces. The left hand-side of the Navier-Stokes equation (3.3) represents inertia, whereas the right hand-side represents the body forces. The driving forces are the buoyancy and the imposed Lorentz force. The velocity boundary conditions are chosen to correspond to the physical model, i.e. no slip boundary condition at the crucible wall and the electrodes, Eq. (3.4), and free slip boundary condition at the free surface, Eq. (3.5).

The energy equation is solved to determine the temperature T of the melt. With the prescribed assumptions the equation for T is then

$$c_P \nabla \cdot (\mathbf{u} \varrho T) = \nabla \cdot (\lambda \nabla T) + \frac{J^2}{\sigma}, \tag{3.6}$$

with the boundary conditions

$$-(\lambda \nabla T) \cdot \mathbf{n} = h(T - T_\infty) \quad \text{at the crucible wall,} \tag{3.7}$$

$$-(\lambda \nabla T) \cdot \mathbf{n} = \epsilon \sigma_{sb}(T^4 - T_\infty^4) \quad \text{at the free surface,} \tag{3.8}$$

$$(\nabla T) \cdot \mathbf{n} = 0 \quad \text{at the electrodes,} \tag{3.9}$$

with the ambient temperature T_∞, the emissivity ϵ, and the Stefan-Boltzmann constant σ_{sb}. The energy equation (3.6) expresses the balance between heat convection on the

left hand-side and heat conduction and heat production on the right hand-side. The heat transfer coefficient h specifies the convective heat transfer at all crucible walls, Eq. (3.7). Under the assumption that h is constant and equal for the whole crucible wall, we evaluated h theoretically. The derivation of h is given in the Appendix A.3. At the free surface of the melt we assume radiative heat transfer being expressed by the law of Stefan-Boltzmann, Eq. (3.8), where ϵ has to be determined experimentally. The heat flux $(\nabla T)\cdot\mathbf{n}$ is assumed to be zero at the electrodes to be consistent with adiabatic conditions.

To calculate the heat input and the imposed Lorentz force we evaluate the Laplace equation for the scalar field of the electric potential ϕ, which is

$$\nabla\cdot(-\sigma\nabla\phi)=0. \tag{3.10}$$

Eq. (3.10) results from $\nabla\cdot\mathbf{J}=0$ and $\mathbf{J}=-\sigma\nabla\phi$. The electrodes and the crucible wall are made of platinum with an electrical conductivity five orders of magnitudes higher than that of glass melt. Basically, we can assume that the electrodes and the crucible wall are equipotential surfaces with a constant electric potential, i.e. we define

$$\phi=\pm U_E/2 \quad \text{at the electrodes,} \tag{3.11}$$

$$\phi=0 \quad \text{at the crucible wall.} \tag{3.12}$$

For the model the planes $x=0$ m and $y=0$ m are also the symmetry planes of the physical model. Firstly, the boundary conditions are applied symmetrically and secondly, the Rayleigh number does not exceed the critical Rayleigh number for symmetry breaking. We verified this assumption with simulations of the whole crucible for various parameter settings. Therefore, we model only a quarter of the glass melt in the crucible. We define the free slip boundary condition, Eq. (3.5), and the adiabatic boundary condition, Eq. (3.9), at both symmetry planes. If we have $\phi=-U_E/2$ at one electrode, $\phi=U_E/2$ at the other electrode, and $\phi=0$ at the crucible wall, the symmetric electric field gives us

$$\phi=0 \quad \text{at the plane x=0 m,} \tag{3.13}$$

$$(\nabla\phi)\cdot\mathbf{n}=0 \quad \text{at the plane y=0 m.} \tag{3.14}$$

An analysis of the governing Eqs. (3.2)-(3.10) shows that the system is highly coupled. Beside the well known coupling of the velocity and the temperature field due to buoyancy in Eq. (3.3) and the heat convection in Eq. (3.6) we have a coupling with the Laplace Eq. (3.10) because of the Lorentz force and the volumetric heat input in Eqs. (3.3) and (3.6), respectively. Overall, the strong variation of the physical properties of the glass melt leads to a strong coupling as well.

The main focus is to evaluate the governing Eqs. (3.2)-(3.10) and to obtain the unknowns of the system, which are the velocity $\mathbf{u}$ and temperature T. We like to obtain an understanding of the Lorentz force distribution and its effects on the flow. For this purpose we systematically vary the magnetic flux density B_0 and the electric potential difference U_E.

Parameter	Value
Heat transfer coefficient h	$4\ \frac{\mathrm{W}}{\mathrm{m^2K}}$
Emissivity ϵ	0.6
Ambient temperature T_∞	1393.15 K
Stefan-Boltzmann constant σ_{sb}	$5.67 \cdot 10^{-8}\ \frac{\mathrm{W}}{\mathrm{m^2K^4}}$

Table 3.1: Remaining parameter settings. The derivation of h is sketched in the Appendix A.3 and the value of T_∞ meets the ambient temperature of the experiment [42].

3.1.2 Implementation and numerical model

The calculations were performed for the *glass 3* whose thermophysical properties are given in Tab. A.2. *Glass 3* is characterized by a low viscosity, e.g. $\eta = 1.2$ Pas at a temperature of 1450 K. The composition results in a nearly black glass melt for which the internal heat transfer by radiation is negligible. In Tab. 3.1 the remaining parameters of the present study are summarized.

The coupled set of equations (3.2)-(3.10) has been solved using the commercial software Fluent which was developed to calculate coupled thermohydrodynamic effects. Furthermore, it is possible to solve the transport equation for scalar fields, which we used to solve the Laplace equation (3.10). With User Defined Functions the Joule heating and the Lorentz force were calculated and introduced to the Navier-Stokes equation (3.3) and the Energy equation (3.6).

The discretisation of the governing equations is done by the finite volume method [19]. For our calculations we have chosen the implicit method with second-order accuracy. The pressure and velocity were linked by the Simple algorithm. We have used the default setting for the under-relaxation factors except for the energy equation, which we have set to 0.97 as the strong coupling may led to unintended oscillations if we would have strong temperature variations. The calculations terminated if the residuals of the continuity and the velocity field were smaller than 10^{-6} and those of the energy and the scalar field were smaller than 10^{-9}. Furthermore, the convergence has been tested for each set of parameters by comparing the volumetric heat input with the heat loss over the crucible walls and the surface of the melt. If the difference between both was smaller than 10^{-3} we have assumed convergence, which was the case for all presented results.

The mesh was generated with Gambit and consists of about $6.13 \cdot 10^5$ elements. The surface of the melt was meshed using the boundary layer option for the crucible wall and the electrode. In the remaining area an unstructured face mesh was created which consists of quadrilateral mesh elements. The mesh node pattern of this source-face was projected through the volume with the Cooper meshing algorithm [20]. We have performed studies to validate the mesh quality. The mesh study is described in the Appendix A.4. Fig. A.2 shows views of the mesh, which was used for all presented calculations.

3.1.3 Results

During our simulations we vary the magnetic flux density between -120 mT $\leq B_0 \leq$ 120 mT and the electric potential difference between 3 V $\leq U_E \leq$ 18 V. This is the order of magnitude of effective magnetic flux densities one can generate for low frequencies as it is used in the laboratory experiment [42]. For the chosen parameter range of U_E we are in a thermally stable regime and can perform steady calculations. Larger values of U_E lead to a thermally unstable regime and would require time-dependent calculations. The experimental results presented by Krieger [42] are conducted in a thermally unstable regime. The heat input is kept constant by continuous regulation of U_E between 19 V and 20 V. Therefore, we can not meet the experimental boundary conditions. The steady numerical simulations presented by Cepite and co-workers [5] reach the temperature range of the experiment with $U_E > 18$ V. On the first sight this seems to be a contradiction to the statement about thermal instability just given. But the physical model of the numerics in [5] contains a rough simplification as the authors define a constant temperature at the crucible wall. This boundary condition imposes a certain temperature range and avoids thermal instability. But the presented flow pattern looks like the flow in so-called Hedly cells, as the fluid is flowing downwards at all parts of crucible wall. In our opinion the chosen boundary condition is not correct. In reality the temperature at the wall is not controlled to a defined value. Instead, the heat transport at the wall is dominated by convection at the outer surface. Therefore, the direct comparison of the simulation and the experiment given in [5] is not possible and does not contribute to a better understanding of the physical phenomena in electromagnetically controlled convection of glass melt.

Before we discuss the influence of the Lorentz force on the velocity and temperature field let us have a closer look at the Lorentz force distribution itself.

Lorentz force distribution

Both components of the Lorentz force, $f_{Lx} = \mathbf{f_L} \cdot \mathbf{e_x}$ and $f_{Lz} = \mathbf{f_L} \cdot \mathbf{e_z}$, see Eq. (3.1), can be rewritten in terms of the electric potential ϕ and become

$$f_{Lx} = -\sigma(T) B_0 \frac{\partial \phi}{\partial z} \quad \text{and} \quad f_{Lz} = \sigma(T) B_0 \frac{\partial \phi}{\partial x}.$$

The sign of f_{Lx} and f_{Lz} – and hence the orientation – can basically be defined by the constant magnitude of the magnetic flux density B_0 and the gradient of the electric potential $\nabla\phi$. As the orientation of $\nabla\phi$ is fixed by the boundary condition at the electrodes, Eq. (3.11), we reverse the direction of f_{Lx} and f_{Lz} with the sign of B_0.

The spatial distribution of the Lorentz force is specified by the temperature-dependent electrical conductivity $\sigma(T)$ and the gradient of the electric potential $\nabla\phi$. An example for the isolines of ϕ is shown in Fig. 3.3 in the planes $y = 0$ m and $z = 0.04$ m. At $z \geq 0.02$ m we mainly find components of $\partial\phi/\partial x$ (f_{Lz}), whereas the intensity of $\partial\phi/\partial z$ (f_{Lx}) is high below the electrodes with $z < 0.02$ m, see Fig. 3.3(a). High values of both Lorentz force components can be expected around the electrodes due to the very close isolines of ϕ. As the electrical conductivity σ is a function of the temperature, the temperature distribution

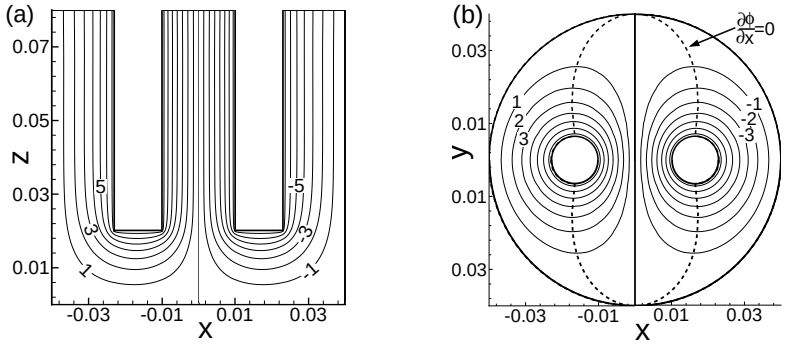

Figure 3.3: Distribution of the electric potential ϕ in V for $U_E = 15$ V in the plane (a) $y = 0$ m and (b) $z = 0.04$ m.

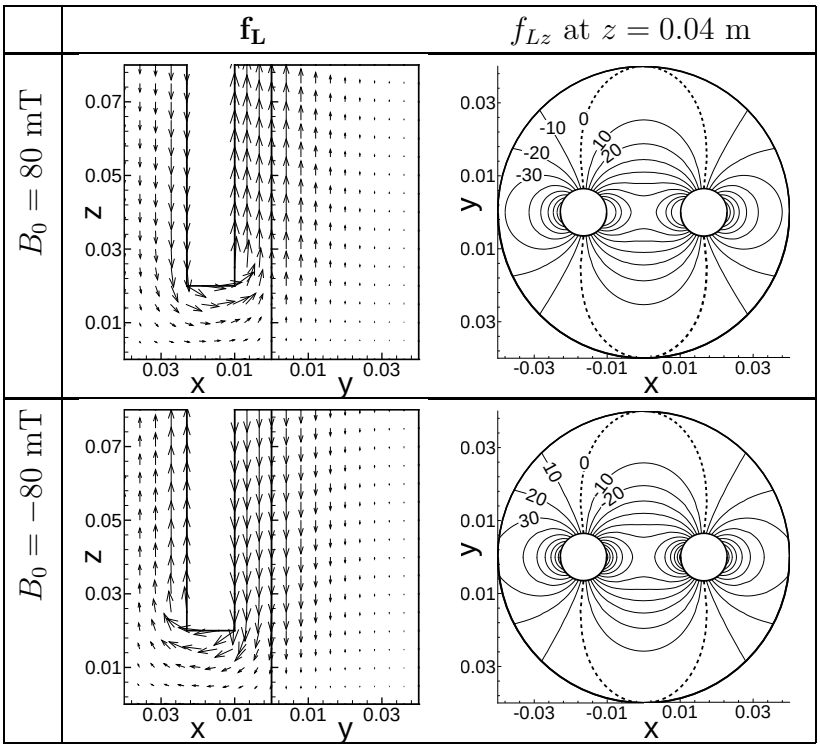

Figure 3.4: Lorentz force distribution for $B_0 = 80$ mT (first row) and $B_0 = -80$ mT (second row) with $U_E = 15$ V. The left diagrams give the vector field of the imposed Lorentz force $\mathbf{f_L}$ at the planes $y = 0$ m and $x = 0$ m. The right diagrams give the isolines of the z-component of the Lorentz force $f_{Lz} = \mathbf{f_L} \cdot \mathbf{e_z}$ at $z = 0.04$ m.

has also an impact on the magnitude of the Lorentz force. In hot regions the increasing value of $\sigma(T)$ leads to an amplification of the Lorentz force.

The left diagrams in Fig. 3.4 give the vector field of $\mathbf{f_L}$ in the symmetry planes $x = 0$ m and $y = 0$ m for $B_0 = 80$ mT (first row) and $B_0 = -80$ mT (second row). We like to emphasize that the impact of both components f_{Lx} and f_{Lz} is supportive and does not conflict. The view of the plane $z = 0.04$ m in the right diagrams of Fig. 3.4 shows f_{Lz}. As expected we find the largest values in the vicinity of the electrodes along $y = 0$ m

and a reversing orientation at the dashed lines which correspond to the dashed lines in Fig. 3.3(b). The isolines of $B_0 = 80$ mT (first row) and $B_0 = -80$ mT (second row) have slightly different paths. It is a result of the unequally distributed temperature-dependent electrical conductivity.

Velocity and temperature distribution

Before we discuss the influence of the imposed Lorentz force let us shortly look at the velocity and temperature fields of the pure thermal convection with $B_0 = 0$ T and $U_E = 15$ V which are shown in the first row of Fig. 3.5. In the left and right diagrams of Fig. 3.5 the vector field of the velocity $\mathbf{u}$ and the temperature T are given for both symmetry planes, namely the plane $y = 0$ m, ranging from 0 m $\leq x \leq$ 0.04 m, and the plane $x = 0$ m, ranging from 0 m $\leq y \leq$ 0.04 m. The diagrams in the middle of Fig. 3.5 show the z-component of the velocity $u_z = \mathbf{u_z} \cdot \mathbf{e_z}$ in the plane $z = 0.04$ m. The positive values of u_z indicate that the upward streams are located around the electrodes for pure thermal convection. We have the largest velocities in the center of the crucible with $x = y = 0$ m. The fluid flows downward in the remaining parts at the crucible wall for $|y| \gtrsim 0.018$ m (indicated by the dashed lines). In the left diagram one can clearly see that the pure thermal convection mainly involves the fluid at the level of the electrodes with $z \geq 0.02$ m. Below the electrodes there is no driving buoyancy force due to the well stratified temperature layers with hot fluid close to the electrodes and cold fluid close to the crucible bottom. Consequently, the melt hardly flows in this region and therefore is badly stirred. In the vicinity of the electrodes the fluid is heated up while it is flowing upwards and we find the highest temperatures just below the surface of the melt. The fluid cools down at the surface and the crucible wall. As the heat loss by radiation at the surface is larger than the convective heat transfer at the crucible wall we obtain large temperature gradients at the free surface.

Starting from a system with pure thermal convection we increase B_0 stepwise with $B_0 > 0$ T and $U_E = 15$ V. In the second and third row of Fig. 3.5 diagrams for $B_0 = 40$ mT and $B_0 = 80$ mT are given. The vector plots of $\mathbf{u}$ (left) and the contour plots of u_z (middle) show that the vertical component of the Lorentz force f_{Lz} in the center amplifies $\mathbf{u}$ significantly. The downward Lorentz force between the crucible wall and the electrode leads to a change of the flow direction in this part of the crucible already for $B_0 = 20$ mT (not shown here). But not only the velocity at the level of the electrodes is affected. The horizontal component of the Lorentz force f_{Lx} controls the fluid flow below the electrodes. The significant increase of $\mathbf{u}$ in this region is illustrated in Fig. 3.6(a). It gives the velocity magnitude $u = |\mathbf{u}|$ measured in terms of velocity magnitude without Lorentz force $u_0 = u(B_0 = 0$ T) along the centerline of the crucible with $x = y = 0$ m. Already at the level of the electrodes u increases by a factor of two for $B_0 = 40$ mT and by a factor of approximately 3.5 for $B_0 = 120$ mT. Close to the bottom u multiplies by almost a factor of four ($B_0 = 40$ mT) up to eight ($B_0 = 120$ mT), thanks to f_{Lx}. The Lorentz force does not only increase the overall velocity, it captures also a region which is not affected by the buoyancy force and therefore leads to a strong improvement of the stirring. We can state that the Lorentz force distribution $\mathbf{f_L}$ is mainly taken over by the velocity field $\mathbf{u}$. The increase of u with B_0 results in a better temperature homogenization as the values of the

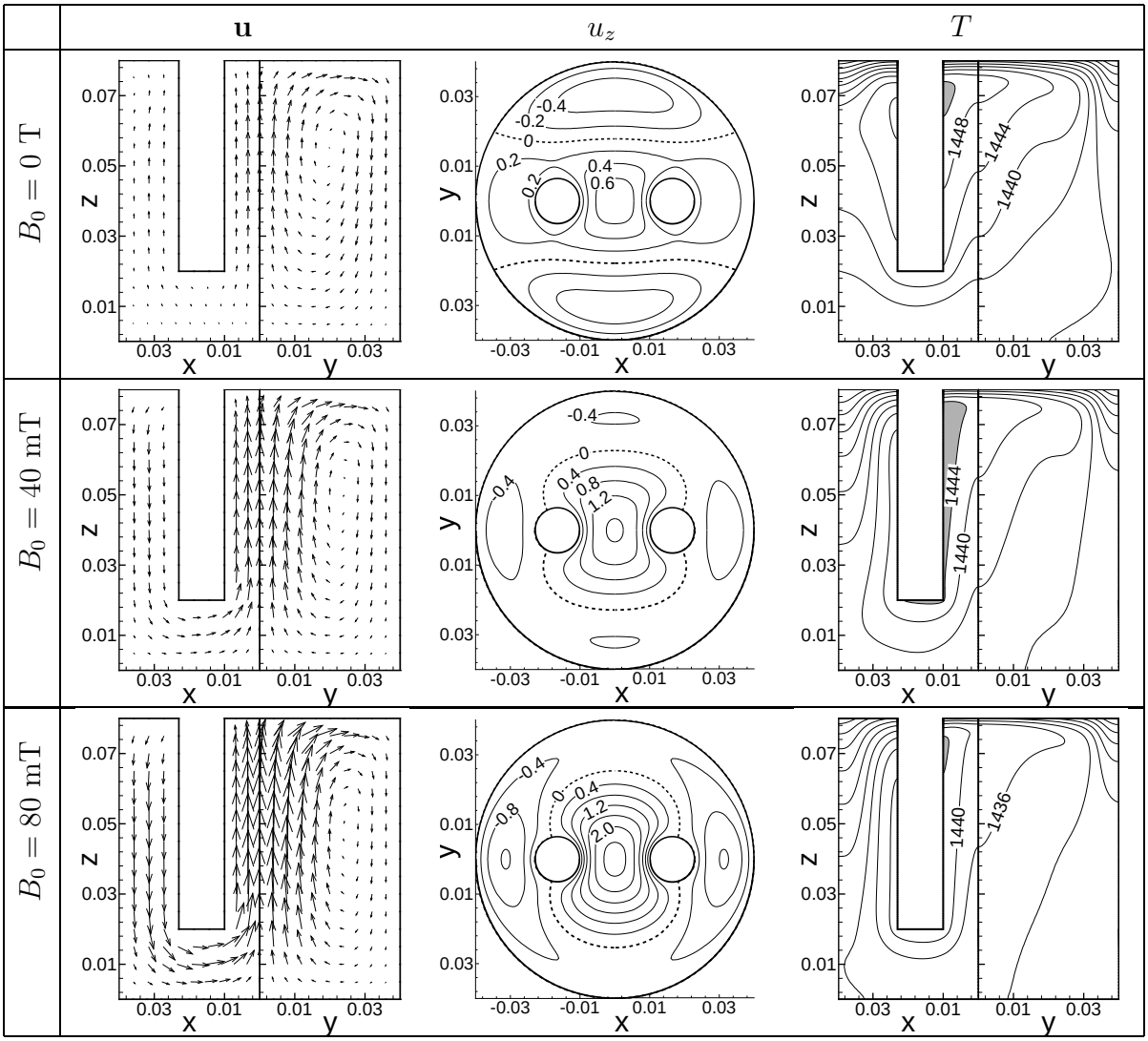

Figure 3.5: The vector field of the velocity $\mathbf{u}$ (left), isolines of the z-component $u_z = \mathbf{u} \cdot \mathbf{e_z}$ in mm/s (middle) and the temperature T in K (right) for $B_0 = 0$ T, $B_0 = 40$ mT, $B_0 = 80$ mT (starting from the first row) and $U_E = 15$ V. The velocity field $\mathbf{u}$ and the temperature T are shown for both symmetry planes, namely the plane $y = 0$ m and the plane $x = 0$ m. The z-component of the velocity u_z is plotted in the plane $z = 0.04$ m. The region with the largest temperature, so-called hot spots, are highlighted in grey.

highest temperature decrease. Fig. 3.6(b) illustrates the temperature homogenization on the basis of the temperature along $x = y = 0$ m. A similar temperature homogenization for $B_0 > 0$ T was observed experimentally by Krieger [42]. The results differ only in the temperature range due to the different heat inputs.

In the following we reverse the direction of the magnetic field and decrease the magnetic field stepwise starting again from $B_0 = 0$ T. First let us look at cases with $B_0 = -40$ mT and $B_0 = -70$ mT which are shown in the second and third row in Fig. 3.7. Now the vertical component of the Lorentz force f_{Lz} supports the thermally driven upward flow between the crucible wall and the electrodes as u_z increases, compare u_z for $B_0 = 0$ T with u_z for $B_0 = -40$ mT and $B_0 = -70$ mT in Fig. 3.7. Again, f_{Lx} controls the flow below the

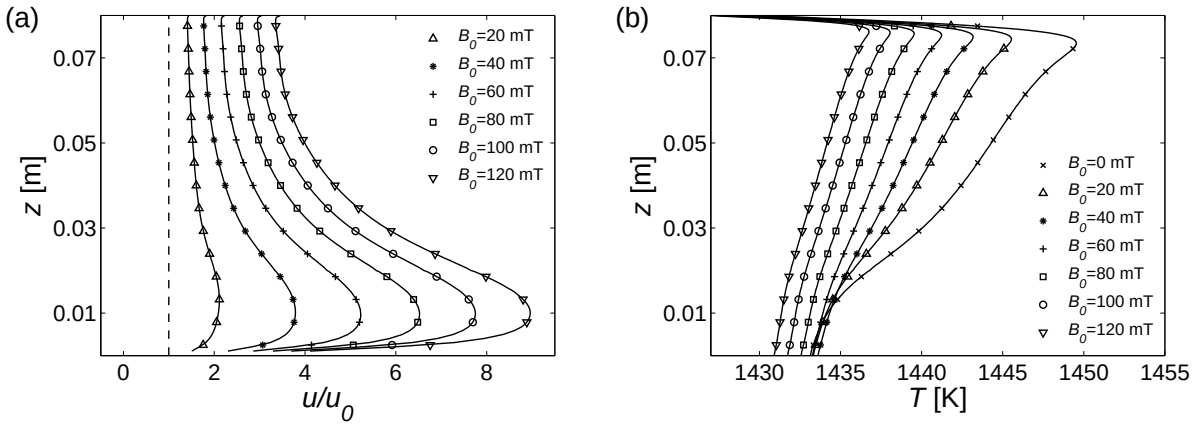

Figure 3.6: (a) The velocity ratio u/u_0 gives the proportion of the velocity magnitude $u = |\mathbf{u}|$ with Lorentz force for $B_0 > 0$ T in comparison to that without Lorentz force $u_0 = u(B_0 = 0\text{T})$ in the centerline of the crucible ($x = y = 0$ m) and $U_E = 15$ V corresponding to Fig. 3.5. The dashed line gives $u = u_0$. In (b) the corresponding temperature distribution is shown.

electrodes. Between the electrodes the downward acting Lorentz force does not lead to an abrupt overall change of the flow direction. At the upper half level of the electrodes u_z is still positive. But the magnitude of the velocity is reduced significantly compared to the thermally driven flow with $B_0 = 0$ T (first row in Fig. 3.7). The upward stream is driven by buoyancy due to the large temperature gradients just below the surface. Just the fluid below $z \approx 0.03$ m ($B_0 = -70$ mT) flows downward with a very small magnitude driven by the Lorentz force. However, the small magnitudes of the velocity are an indicator for almost equal forces – nether the buoyancy nor the Lorentz force is clearly dominating in the center of the crucible. As a result, the region of the almost stagnant flow regime close to the bottom of the center expands. On the one hand $\mathbf{f_L}$ leads to a better motion below the electrodes and larger velocities at the crucible wall. On the other hand the motion between the electrodes slows down and leads to an almost stagnant flow region. Fig. 3.8(a) shows the reduction of u in the centerline for $B_0 = -20$ mT, -40 mT, and -60 mT in comparison to $u_0 = u(B_0 = 0$ T). Especially for $z \leq 0.03$ m u reduces dramatically and tends to zero. Due to the low velocities in the centerline the temperatures between the electrodes and the temperature differences increase significantly as it is shown in Fig. 3.8(b).

If we now slightly change the magnetic flux density from $B_0 = -70$ mT to $B_0 = -71$ mT we observe a drastic change in the flow pattern and temperature distribution, compare third and forth row of Fig. 3.7. In the centerline buoyancy can not compensate f_{Lz} which leads to a change of flow direction with large changes of the velocity magnitude. Now the fluid in the vicinity of the centerline is flowing downwards, moving below the electrodes to the crucible wall and between the crucible wall and the electrode to the surface. The velocity magnitude in the center, especially for $z < 0.03$ m, is now again a multiple of the velocity magnitude without Lorentz forces as indicated by the curves with $B_0 = -80\text{mT}, -100\text{mT}, -120\text{mT}$ in Fig. 3.8(a). For $B_0 \leq -71$ mT the qualitative picture of the velocity field $\mathbf{u}$ corresponds to the distribution of the Lorentz force $\mathbf{f_L}$ and

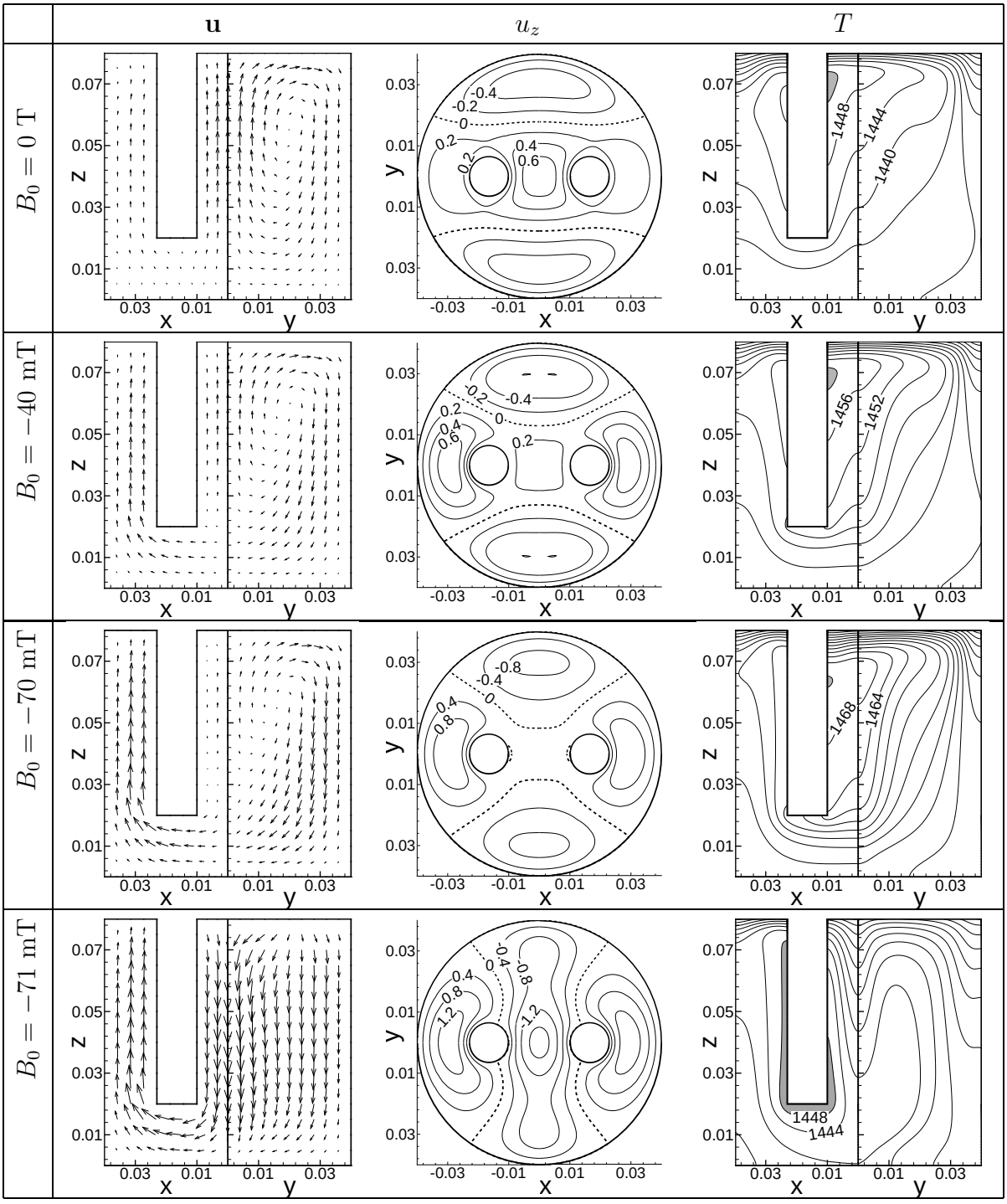

Figure 3.7: The vector field of the velocity $\mathbf{u}$ (left), isolines of the z-component $u_z = \mathbf{u} \cdot \mathbf{e_z}$ in mm/s (middle) and the temperature T in K (right) for $B_0 = 0$ T, $B_0 = -40$ mT, $B_0 = -70$ mT, $B_0 = -71$ mT (starting from the first row) and $U_E = 15$ V. The results are obtained by starting from a system with $B_0 = 0$ T and reducing B_0 stepwise. Always a converged solution is used as starting condition for the calculation.

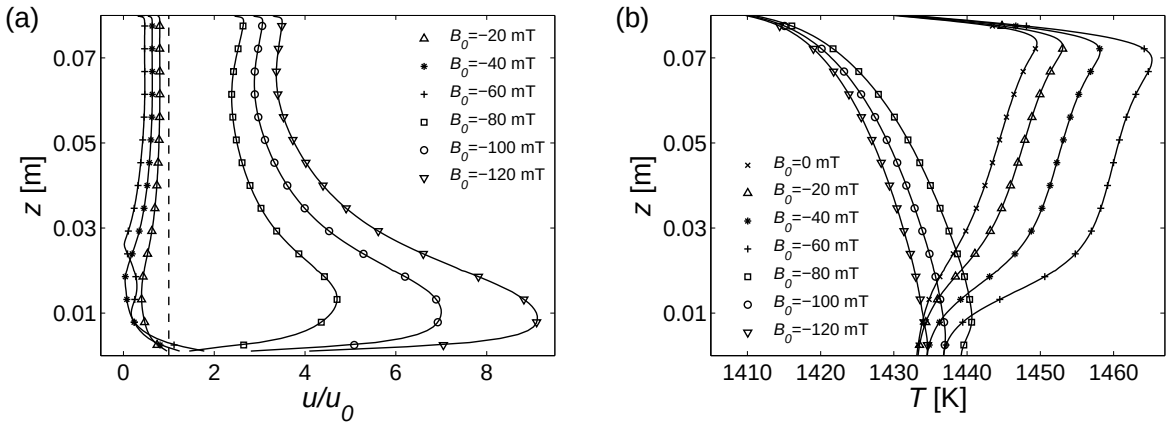

Figure 3.8: Profile for downward Lorentz force in the center of the crucible of (a) the velocity ratio u/u_0 and (b) the temperature distribution T for $B_0 < 0$ T and $U_E = 15$ V. For $u/u_0 < 1$ the velocity u is smaller than the velocity without Lorentz force u_0.

hence, is now opposite to that of $B_0 > 0$ T. Still we find the largest temperature in the vicinity of the electrodes, but now at their bottom as the fluid is heated up while it is flowing downwards between the electrodes.

Now we start at a converged solution with $B_0 \leq -71$ mT and increase B_0 stepwise. The transition of the flow pattern takes place at different B_0. We pass through a hysteresis for which we obtain two different steady solutions with unequal flow patterns for one set of parameters depending on the starting condition of the calculations. The cases with a dominating upward stream between the electrodes we name 'upper branch' of the hysteresis and the cases with dominating downward stream we name 'lower branch'. Let us stress that the transition from the upper to the lower branch is characterized by an abrupt change of the flow pattern even if we change B_0 just per 1 mT. For all U_E we studied the transition of the flow patterns is identical to the discussed transition for $U_E = 15$ V. In contrast, qualitative differences for the transition from the lower to the upper branch of the hysteresis exist depending on U_E.

Let us first look at the transition from the lower to the upper branch for $U_E = 15$ V given in Fig. 3.9. Here, converged solutions of the lower branch are used as starting condition for a system with increasing B_0. The first row of Fig. 3.9 gives the solution for $B_0 = -70$ mT which we obtained using the converged solution for $B_0 = -71$ mT (last row in Fig. 3.8) as starting condition. The differences between the flow pattern and temperature distributions of the solutions of the upper branch (third row of Fig. 3.8 with $B_0 = -70$ mT) and the lower branch (first row of Fig. 3.9 with $B_0 = -70$ mT) are obvious. If we reduce the Lorentz force by increasing B_0 to -50 mT (second row in Fig. 3.9), the motion decelerates in general and buoyancy becomes more relevant in some regions of the melt. As shown in the plane $x = 0$ m the temperature gradients just below the surface lead to an enormous deceleration of the downward motion. The same holds for the region between the electrodes with $z \lesssim 0.04$ m. A further reduction of the Lorentz force results in a change of the flow direction in these regions. The flow splits

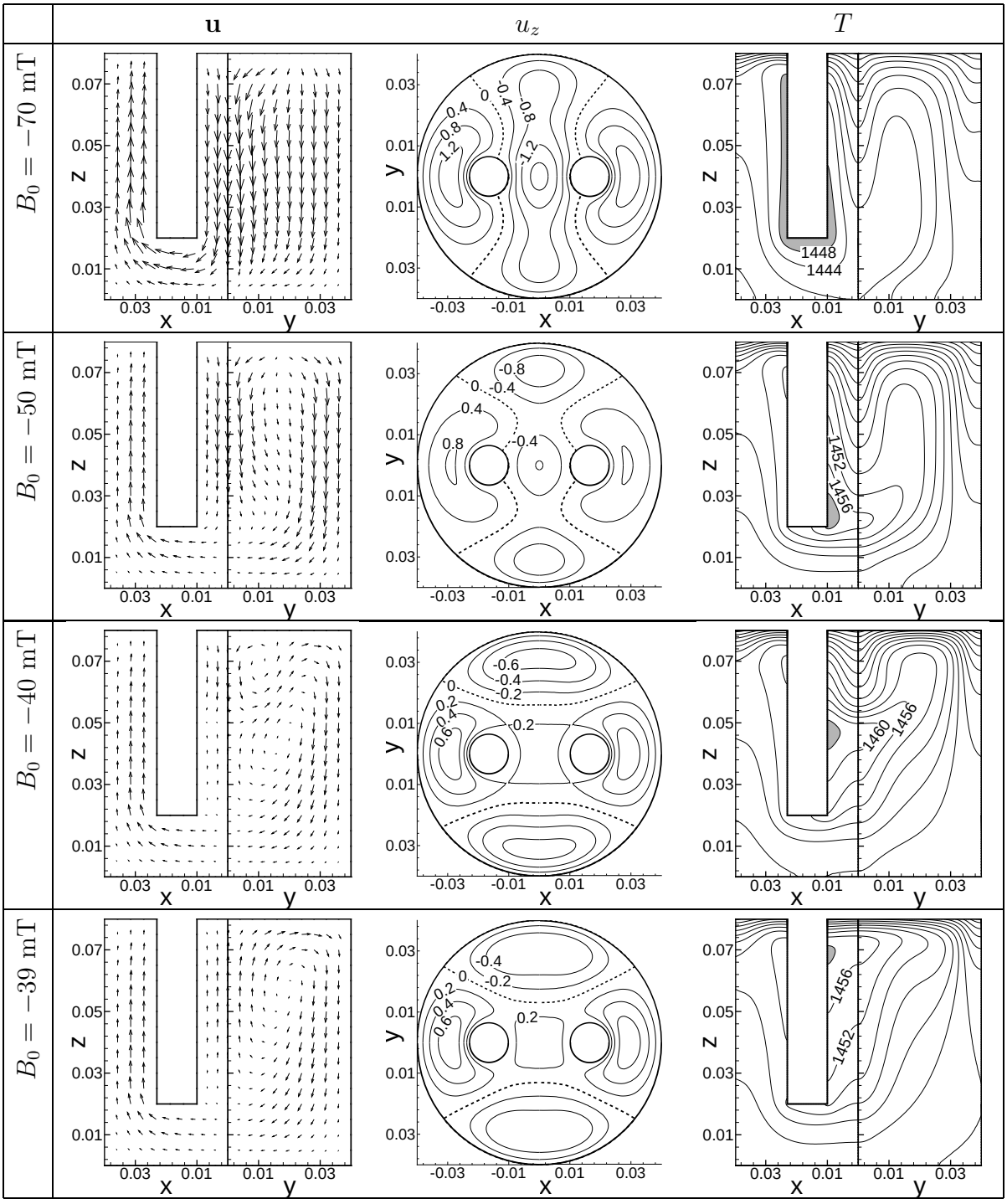

Figure 3.9: Velocity and temperature distribution for a system with $U_E = 15$ V and stepwise increased B_0 ($B_0 = -70$ mT, -50 mT, -45 mT, -40 mT, -39 mT) starting with the converged solution for $B_0 = -71$ mT .

into several vortices which can be seen in the plane $x = 0$ m for $B_0 = -40$ mT (third row of Fig. 3.9). For $z < 0.05$ m the fluid flows up with the lower vortex having a very small magnitude. For $z > 0.05$ m the motion is still dominated by the Lorentz force and flows downwards. The isolines of u_z show that the downward flow between the electrodes

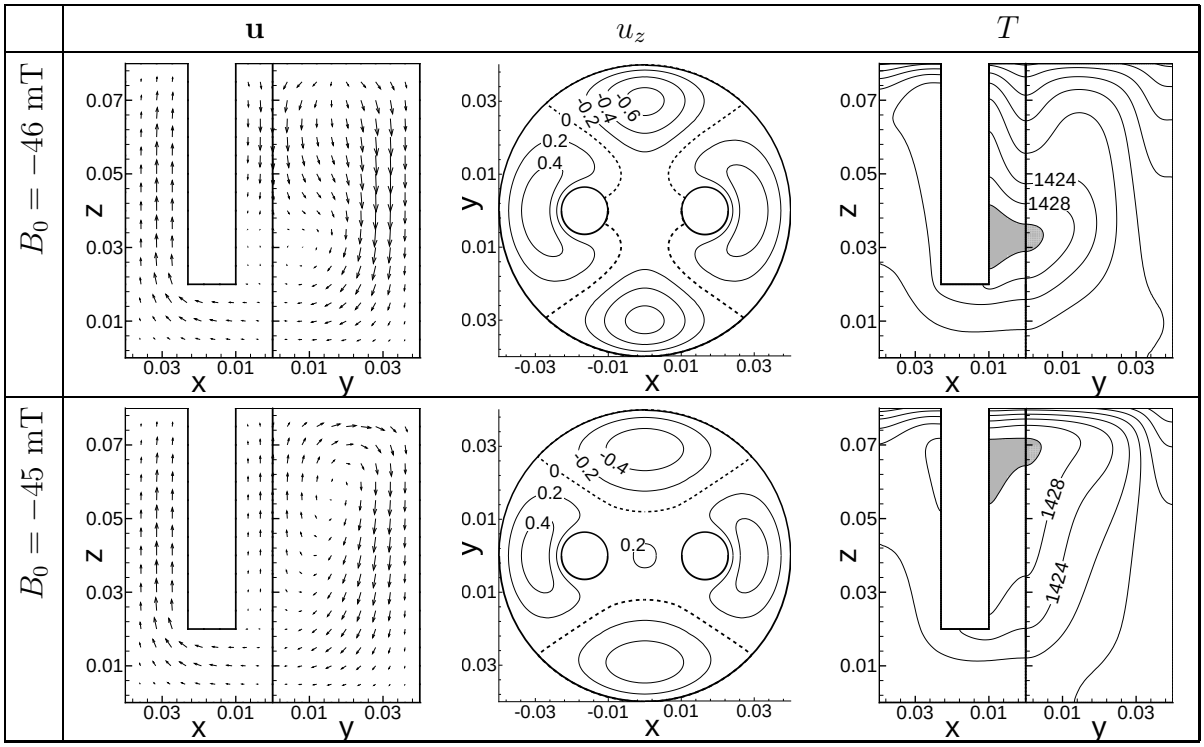

Figure 3.10: Velocity and temperature distribution showing the transition from the lower to the upper branch for $U_E = 12$ V.

is limited to a small region (bounded by the dashed lines). But in the centerline the velocity magnitude of the downward flow is still larger than the magnitude of the upward flow. While we increase B_0 from -70 mT up to -40 mT the hot spot in the vicinity of the electrodes moves from the bottom of the electrodes ($B_0 = -70$ mT) to the region between the electrodes. There, the hot spot is moving from $z \approx 0.023$ m ($B_0 = -50$ mT) to $z \approx 0.048$ m ($B_0 = -40$ mT). The downward stream between the electrodes disappears completely for $B_0 = -39$ mT as shown in the last row of Fig. 3.9. Thus, the transition from the lower to the upper branch is characterized by the merging of the two vortices to a single vortex in the centerline.

Fig. 3.10 illustrates the transition from the lower to the upper branch for $U_E = 12$ V. Just before the transition, $B_0 = -46$ mT, buoyancy leads to a reversing of the flow direction only in the centerline with $z \leq 0.032$ m. The temperature gradient below the surface does not lead to upward streams and hence, the flow does not split into several vortices.

One possibility to illustrate the regime of the two-valued solutions and the transition of the flow pattern is to look at the maximum z-component of the velocity at $x = y = 0$ m, which we label u_{zmax}. The transition of the flow pattern is characterized by a shift of the sign of u_{zmax}, whereas u_{zmax} is greater than zero at the upper branch and smaller than zero at the lower branch. In Fig. 3.11(a) u_{zmax} is given as a function of B_0 for various U_E. The right diagram gives a detailed view of the region with two solutions. First of all, the region of two-valued solutions $u_{zmax}(B_0)$ depends on U_E. As summarized in Tab. 3.2 we obtain two solutions between -58 mT $\leq B_0 \leq -46$ mT for $U_E = 9$ V. This range expands to -71 mT $\leq B_0 \leq -46$ mT if we consider $U_E = 12$ V. A further increase of

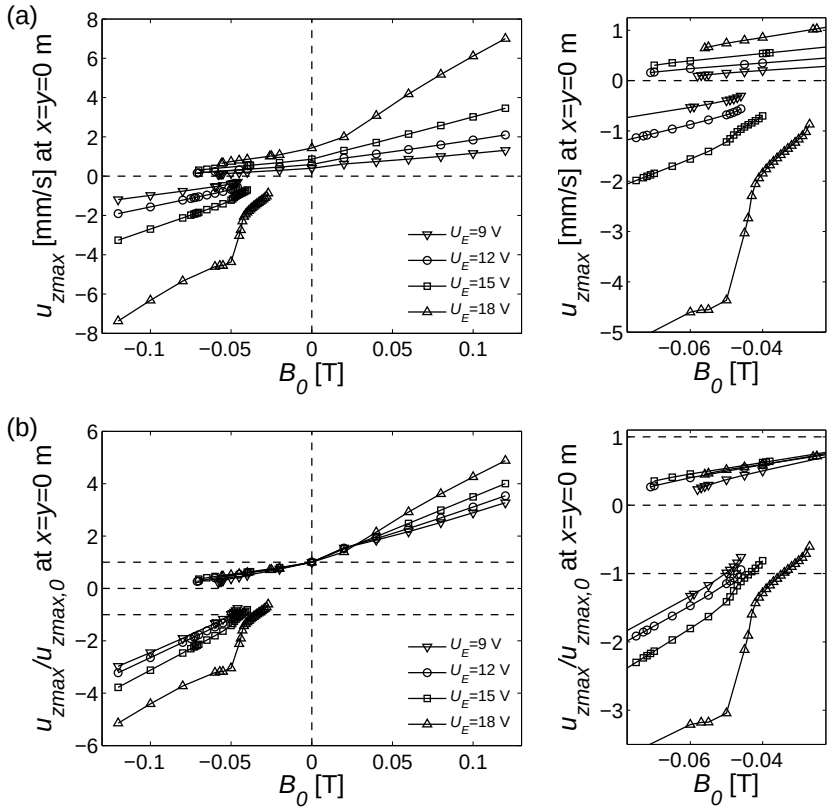

Figure 3.11: (a) Maximum z-velocity of the velocity in the centerline of the crucible u_{zmax} as a function of B_0 for various U_E. In (b) the ratio between u_{zmax} and $u_{zmax,0} = u_{zmax}(B_0 = 0$ T) is given. The detailed views (right) show that the range of two-valued solutions $u_{zmax}(B_0)$ depends significantly on U_E.

U_E	B_0 Range of two-valued solution
9 V	-46 mT ... -58 mT
12 V	-46 mT ... -71 mT
15 V	-40 mT ... -70 mT
18 V	-27 mT ... -56 mT

Table 3.2: Range of magnetic flux densities B_0 for which we obtain two different solutions depending on the starting conditions of the calculations. The range of B_0 varies with the electric potential difference U_E.

the electric potential difference to $U_E = 15$ V leads only to a similar parameter range of two solutions, which is -70 mT $\leq B_0 \leq -40$ mT. For $U_E = 18$ V the change from $u_{zmax} > 0$ to $u_{zmax} < 0$ happens if we start at a steady solution with $B_0 = -56$ mT and apply $B_0 = -57$ mT. Therefore, the parameter range with two steady solutions changes to -56 mT $\leq B_0 \leq -27$ mT. In Fig. 3.11(b) u_{zmax} is measured in terms of the maximum

z-component of the velocity without Lorentz force, $u_{zmax,0} = u_{zmax}(B_0 = 0)$. The diagram $u_{zmax}/u_{zmax,0}(B_0)$ confirms that the velocity increases almost linearly with B_0 for $B_0 > 0$ T. The deceleration of the motion in the upper branch with $B_0 < 0$ T is reflected in Fig. 3.11(b) as $0 < u_{zmax}/u_{zmax,0} < 1$.

Maximum stretching function

For the application not only the effects of the Lorentz force on the temperature distribution and velocity field are important. Especially the effect on the homogenization – how the mixing in laminar flow can be improved – is of interest. Laminar mixing is characterized by molecular diffusion on the interfaces between two fluids or inhomogeneities. It is based on the interface increase by deformation of fluid volumes. Different definitions exist to quantify the mixing effect [59]. Typically deformations of infinitesimal elements, lines, surfaces, and volumes are used which are based on the stretching function. The stretching function is a measure of the deformation velocity of an element. Its theoretical maximum value α is given by [68]

$$\alpha = \sqrt{\mathbf{D} : \mathbf{D}}, \tag{3.15}$$

where $\mathbf{D} = 1/2(\nabla\mathbf{u} + (\nabla\mathbf{u})^T)$ is the symmetric stretching tensor. As pure rotation does not contribute to the deformation of fluid volumes the antisymmetric vorticity tensor is not part of the definition of α. α can be obtained easily from the presented simulation data of the velocity field. Large α lead to large deformations and an increase of the interface between the fluid volumes. The goal of each mixing techniques is to maximize the deformation and hence, to maximize α in the whole volume. It is a first step towards the evaluation of the influence of the Lorentz force on laminar mixing.

Fig. 3.12 shows isolines of α for pure thermal convection (first row) and for Lorentz force dominated flows with $B_0 = 80$ mT (second row) and $B_0 = -80$ mT (third row). Due to low velocities below the electrodes and close to the bottom for $B_0 = 0$ T, α is very small in this region as indicated by the grey shaded areas. We find larger values of α around the electrodes and for $y \geq 0.035$ m in the plane $x = 0$ m because of the additional isolines. In Lorentz force dominated regimes (second and third row of Fig. 3.12) α increases significantly as the grey shaded areas almost disappear, especially close to the bottom for $z \leq 0.02$ m. We can observe some differences in the α distribution for $B_0 = 80$ mT and $B_0 = -80$ mT even though the magnitudes of both magnetic flux densities are equal and the flow is dominated by the Lorentz force. For $B_0 = 80$ mT α hardly changes for $y \geq 0.025$ m. But for $B_0 = -80$ mT we observe a slight increase of α in this region due to closer isolines. We find the largest values of α in the vicinity of the electrodes for both signs of B_0. In the case of $B_0 = 80$ mT the isoline density is largest between the electrodes. In contrast, the isoline density is largest between the crucible wall and one electrode for $B_0 = -80$ mT.

Slight differences also exist between the solutions of the upper and the lower branch of the two-valued regime which are obtained with the same set of parameters. As shown in Fig. 3.13 for $B_0 = -40$ mT α differs in the region between the electrodes. Due to the split of the flow in vortices α is larger for the solutions of the lower branch (second row

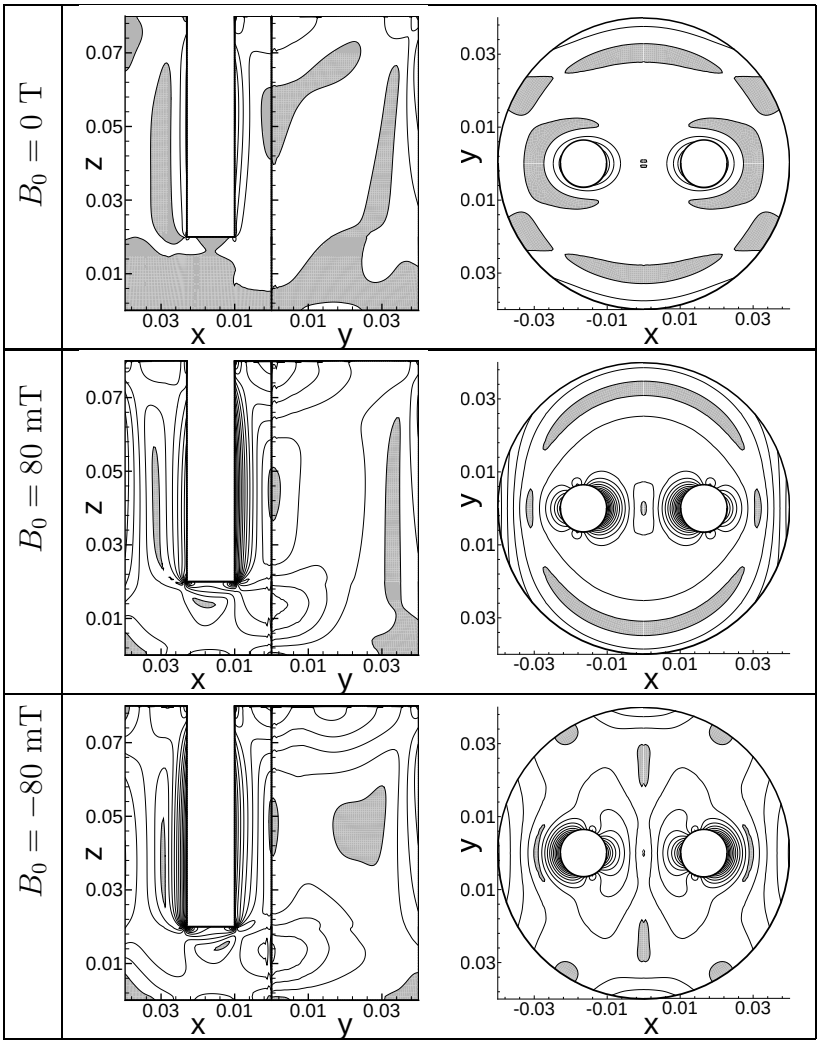

Figure 3.12: Isolines of the maximum stretching function α in s^{-1} in the planes $y = 0$ m, $x = 0$ m (left) and $z = 0.04$ m (right) for $U_E = 15$ V. In the first row α is given for pure thermal convection. The second ($B_0 = 80$ mT) and third row ($B_0 = -80$ mT) show α for Lorentz force dominated flows. The grey shading highlights areas with $\alpha \leq 0.02$ s^{-1}. Between the isolines the difference of α is 0.04 s^{-1}.

in Fig. 3.13) than for the solutions of the upper branch (first row in Fig. 3.13) of the hysteresis.

Global analysis

During the discussions in the previous section we gained a good insight into the electromagnetically flow control by studying flow pattern, temperature distributions, variations of local velocities and temperatures, and the distribution of the maximum stretching function. In the following paragraphs a coarse measure of the overall influence of the imposed Lorentz force on the flow can be given with volume-averaged quantities.

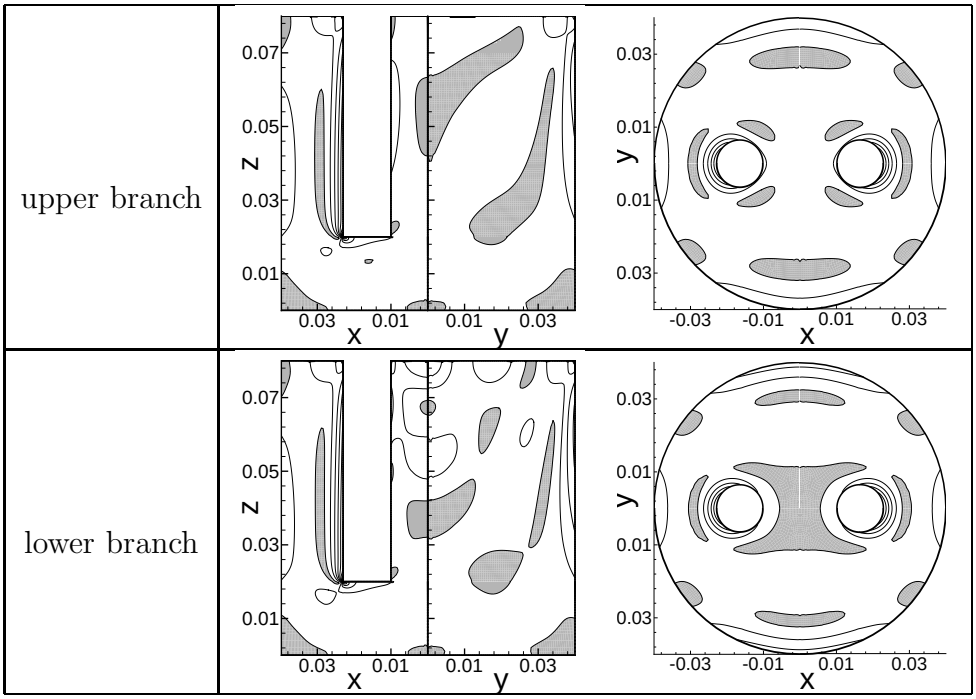

Figure 3.13: Like in Fig. 3.12 the isolines of α are shown for $U_E = 15$ V. Here both plots are obtained for $B_0 = -40$ mT, whereas the first row belongs to the upper branch of the hysteresis with $u_{zmax} > 0$ and the second row belongs to the lower branch with $u_{zmax} < 0$.

First of all we define the volume-averaged velocity magnitude $\overline{u}$ according to

$$\overline{u} = \sqrt{\int |\mathbf{u}|^2 dV/V}. \tag{3.16}$$

In Fig. 3.14 $\overline{u}$ is given in terms of $\overline{u_0} = \overline{u}(B_0 = 0\ \text{T})$. Note that $\overline{u}/\overline{u_0}$ is never smaller than unity except for $B_0 = -20$ mT and $U_E = 15$ V. It indicates, that the Lorentz force leads to an overall increase of the kinetic energy for almost all considered cases. For $B_0 \geq 20$ mT $\overline{u}$ is almost a linear function of B_0 and can become a multiple of $\overline{u_0}$, e.g. $\overline{u} \approx 2\overline{u_0}$ for $U_E = 15$ V, $B_0 = 60$ mT and $\overline{u} \approx 3\overline{u_0}$ for $U_E = 15$ V, $B_0 = 100$ mT. In general, the larger U_E and B_0 become, the larger is the ratio $\overline{u}/\overline{u_0}$. For $B_0 < 0$ T the discontinuous transition of the flow pattern from $u_{zmax} > 0$ to $u_{zmax} < 0$ is reflected by a jump in the graph $\overline{u}/\overline{u_0}(B_0)$. Again, after the change of the flow direction $\overline{u}/\overline{u_0}$ is a linear function of B_0. Interestingly, in the linear regime with $B_0 < 0$ T the ratio $\overline{u}/\overline{u_0}$ is larger than for the same magnitude of B_0 with $B_0 > 0$ T. For example we have $\overline{u}/\overline{u_0} \approx 4.5$ for $U_E = 18$ V, $B_0 = 120$ mT and $\overline{u}/\overline{u_0} \approx 5$ for $U_E = 18$ V, $B_0 = -120$ mT. Before reaching the linear regimes (small magnitudes of B_0) buoyancy is still present and influences the flow. The Lorentz force does not completely control the motion and hence, the slope of the graph $\overline{u}/\overline{u_0}(B_0)$ is smaller than in the linear regimes. Especially for $B_0 = -20$ mT the kinetic energy hardly increases as $1.00 \leq \overline{u}/\overline{u_0} \leq 1.04$. If the flow pattern is identical to the Lorentz force distribution we can observe the linear relation between $\overline{u}$ and B_0. The right diagrams in Fig. 3.14 give detailed views of the two-valued regime.

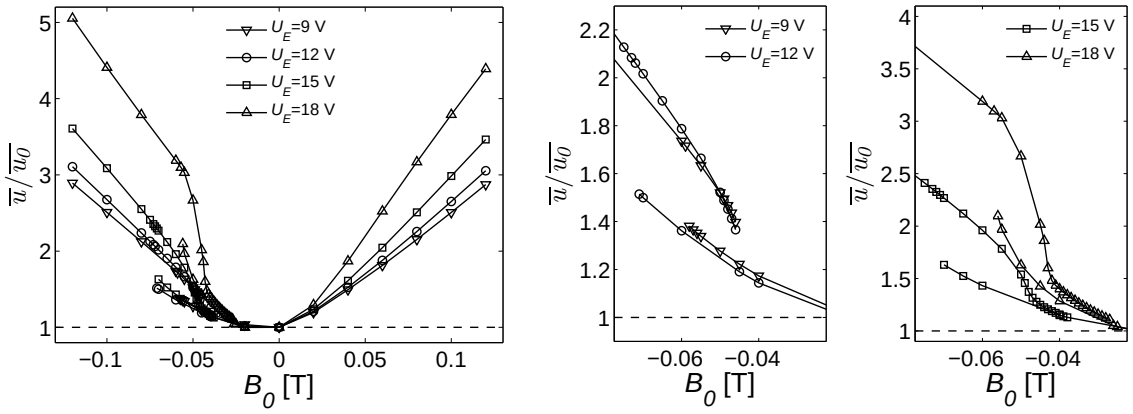

Figure 3.14: Ratio $\overline{u}/\overline{u_0}$ as function of B_0 being a coarse global measure of the overall influence of the Lorentz force. The volume averaged velocity $\overline{u}$ is defined by $\overline{u} = \sqrt{\int |\mathbf{u}|^2 dV/V}$ and $\overline{u_0} = \overline{u}(B_0 = 0\text{T})$ is the volume averaged velocity for pure thermal convection without Lorentz force. The Lorentz force increases the kinetic energy in the system, as $\overline{u}/\overline{u_0} > 1$ for almost all $B_0 \neq 0$.

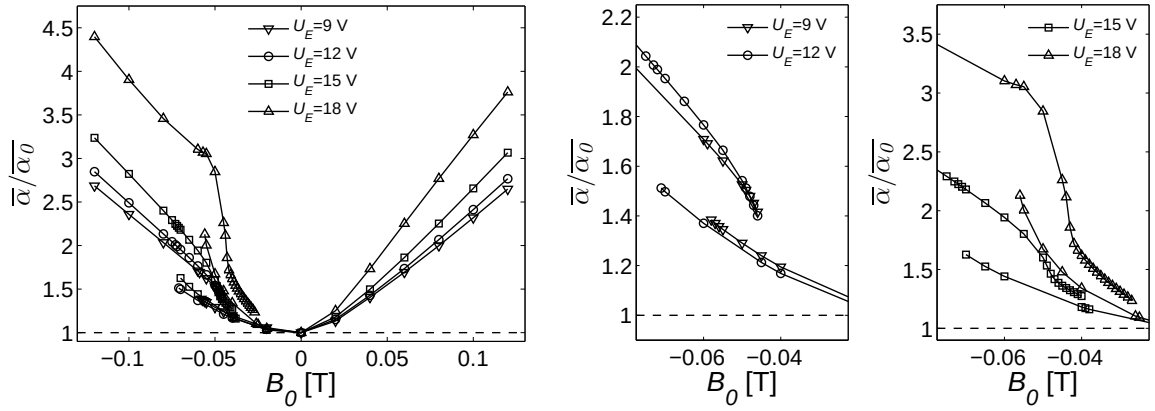

Figure 3.15: Volume averaged maximum stretching function $\overline{\alpha} = \int \alpha dV/V$ measured in terms of $\overline{\alpha_0} = \overline{\alpha}(B_0 = 0$ T) as function of B_0.

We can also define a volume averaged maximum stretching function

$$\overline{\alpha} = \int \alpha dV/V, \tag{3.17}$$

being a coarse measure of the overall mixing rate. A comparison of Figs. 3.14 and 3.15 shows that the development $\overline{\alpha}/\overline{\alpha_0}(B_0)$ is almost identical to that of $\overline{u}/\overline{u_0}(B_0)$. For a wide range of values of the imposed Lorentz force the maximum stretching function – and hence the mixing – increases significantly.

The effect on the temperature and the temperature homogenization can be illustrated by the maximum temperature in the melt T_{max} and the difference of the maximum and

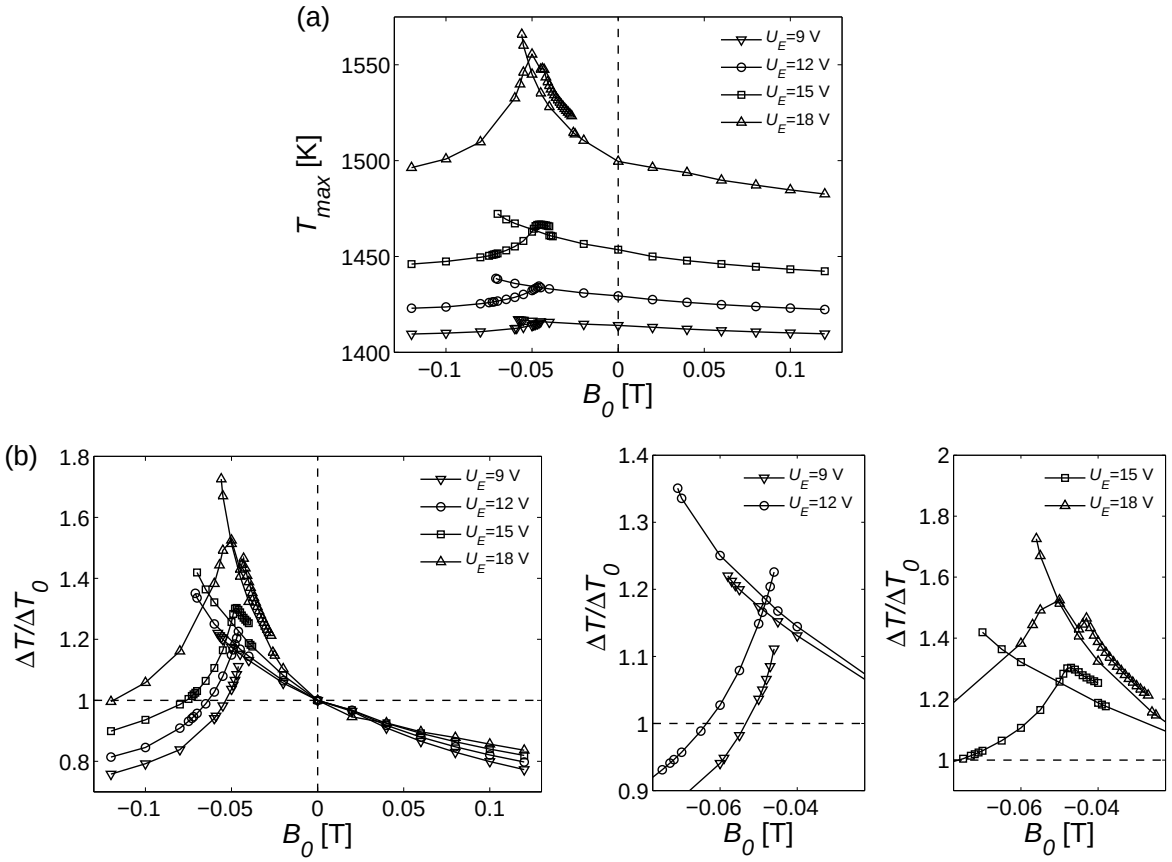

Figure 3.16: (a) The maximum temperature in the melt T_{max} as function of B_0. In (b) the ratio of the temperature difference $\Delta T = T_{max} - T_{min}$ and the temperature difference of the pure thermal convection $\Delta T_0 = \Delta T(B_0 = 0\ \mathrm{T})$ is given. The temperature homogenization improves with B_0 if $\Delta T/\Delta T_0 < 1$ and changes to the worse for $\Delta T/\Delta T_0 > 1$.

minimum temperature in the melt

$$\Delta T = T_{max} - T_{min}. \tag{3.18}$$

In Fig. 3.16(a) $T_{max}(B_0)$ and in Fig. 3.16(b) $\Delta T/\Delta T_0(B_0)$ with $\Delta T_0 = \Delta T(B_0 = 0\ \mathrm{T})$ are given. For $B_0 > 0$ T and all U_E we have $\Delta T/\Delta T_0 < 1$ – the temperature homogenization improves. The smaller U_E the smaller $\Delta T/\Delta T_0$ becomes. If we look at $B_0 < 0$ T and decrease B_0 starting from $B_0 = 0$ T we observe that $\Delta T/\Delta T_0$ significantly increases. It indicates a worse temperature homogenization than without Lorentz force. For $U_E = 9$ V we have a maximum of $\Delta T/\Delta T_0 \approx 1.22$, but if we double U_E the maximum temperature difference in the melt is $\Delta T/\Delta T_0 \approx 1.73$ which is reached just before the change of flow direction. Also the transition from the lower to the upper branch of the hysteresis is characterized by $\Delta T/\Delta T_0 > 1$.

Finally, let us have a look at the overall volume-averaged Lorentz force

$$\overline{f_L} = V^{-1} \int |\mathbf{f_L}| dV, \tag{3.19}$$

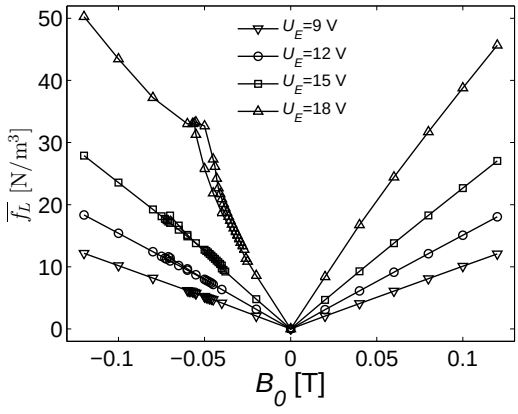

Figure 3.17: Volume averaged Lorentz force $\overline{f_L} = V^{-1} \int |\mathbf{f_L}| dV$ as function of the magnetic flux density B_0 for various electrode potentials U_E.

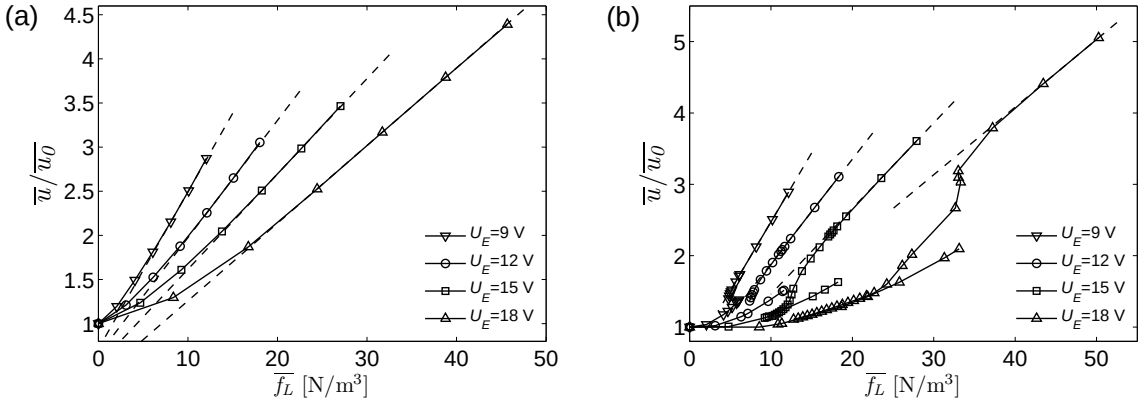

Figure 3.18: The ratio $\overline{u}/\overline{u_0}$ as a function of $\overline{f_L}$ for (a) $B_0 \geq 0$ T, and (b) $B_0 \leq 0$ T. It is a global but coarse indicator for how the Lorentz force influences the kinetic energy. The dashed straight lines identify the regions in which $\overline{u}/\overline{u_0}(\overline{f_L})$ is almost a linear function.

which is given in Fig. 3.17 as a function of B_0 for various U_E. First of all, for $B_0 > 0$ T and $U_E = 9$ V, 12 V, and 15 V $\overline{f_L}$ increases almost linearly with B_0. The parameters lead to a temperature range, in which the electrical conductivity is hardly changing with the temperature. Therefore, the electric current density is almost independent of the flow – and $\overline{f_L}$ is a linear function of B_0. The impact of temperature-dependent electrical conductivity can be seen for $U_E = 18$ V and $B_0 > 0$ T. Here we have a larger temperature range, in which a reduction of T leads to a reduction of $\sigma(T)$ and $\mathbf{J}$. As a result $\overline{f_L}$ slightly deviates from linearity. A deviation from linearity also exists in the parameter space in which we obtain two solutions. It can been seen already for $U_E = 12$ V, 15 V and is eyecatching for $U_E = 18$ V.

Fig. 3.18 gives an answer to the question wether the velocity depends linearly on the Lorentz force in a three-dimensional configuration. The regions in which $\overline{u}/\overline{u_0}(\overline{f_L})$ is almost a linear function are highlighted by the dashed straight lines. Again we identify

two regions of linearity: for $B_0 > 0$ T shown in Fig. 3.18(a) and for solutions of the lower stable branch after the transition from the upper branch with $B_0 < 0$ T shown in Fig. 3.18(b).

3.2 One-dimensional analytical model

The numerical studies presented in Sec. 3.1 reveal the influence of the Lorentz force on the flow structures in glass melt. However, such three-dimensional computations require long simulation times. Therefore, they are restricted to a limited number of parameters. In Sec. 3.1 we have varied electric potential between the electrodes U_E and the magnetic flux density B_0 to study the influence of the imposed Lorentz force. We performed the calculations for one specific glass melt and failed to reveal the difference between the role of the temperature-dependent viscosity and the temperature-dependent electrical conductivity.

One possibility to perform extensive parameter studies and to obtain a deeper understanding of the basic physics is to develop simplified models which can be studied at low computational cost. The formulation of such a model is the goal of the present section. The large convection rolls which arise in the melting furnace suggest to formulate such models on the basis of the assumption that the fluid is confined to an annular loop which contains heating, cooling, and forcing zones. Such assumption enables us to study an one-dimensional form of the fluid flow and to obtain a better understanding of the flow behavior in a convection roll under the influence of an imposed Lorentz force.

More specifically, our present work is inspired by previous studies on natural circulation loops which consist of at least one heat source and one higher elevated heat sink connected by pipes. The convection in such loops is driven by buoyancy only. These systems have various important applications in energy conservation systems for example solar heaters and cooling systems of nuclear reactors and have been the subject of a large number of theoretical and experimental studies. Reviews of the wide applications are given by Zvirin [88] and Greif [28]. This field of research was pioneered by Keller [41] and Welander [84] who used natural circulation loops to model geothermal and geophysical processes. The Lorenz-like chaotic alternations of flow directions were also experimentally observed and theoretically analyzed for example by Creveling et al. [11] and Ehrhard & Müller [16]. Beside the most common analytical approach to average the governing equations over the pipe cross section, Desrayaud et al. [15] performed two-dimensional time-dependent analysis showing the influence of radial components on the flow characteristic. In a few works the fluid of the loop was considered to be electrically conducting. In the presence of a transverse magnetic field eddy currents and a Lorentz force can be induced and can lead to a damping of the motion. Poddubnaya & Shaidurov [61] studied two hydrodynamically connected vertical pipes heated from below and showed that the onset of convection is a function of the magnetic flux density. Ghaddar analyzed in [21] and [22] the influence of the magnetic field density on the flow characteristic for similar geometries over a wide range of parameters.

To our knowledge, no analytical studies about the influence of temperature-dependent

material properties on the flow characteristic of a loop exist in the literature. We already showed in Chapter 2 that the temperature-dependent viscosity modifies the flow significantly and can lead to non-linear flow characteristics, instabilities, and multi-valued solutions even in simple geometries like pipes. Furthermore, experimental and numerical investigations of Rayleigh-Bénard convection cells with large viscosity variations exist in the literature which have been motivated by the Earth's mantle convection. Already the pioneering works of Torrance & Turcotte [75] and Booker [4] showed the modification of heat transfer and flow structures due to the temperature-dependent viscosity. For extremely large viscosity variations a stagnant lid developed in the uppermost coldest part. The transition regimes were studied numerically by Ogawa et al. [56] for a 3d configuration and have been extended for a wide range of Rayleigh numbers and viscosity contrast up to 10^{14} for a 2d square cell by Moresi & Solomatov [53]. This overview shows that already the investigation of the flow of a fluid with temperature-dependent viscosity in a loop – even without imposed Lorentz force – represents a useful generalization of previous works.

The present work is a direct continuation of our previous paper [25] which dealt with an analytical model for a circular loop including a Lorentz force as an additional parameter. This model, like the present one, was motivated by the convection of glass melt in a crucible under the influence of the imposed Lorentz force. The Lorentz force in [25], henceforth referred to as GT5, was generated by an electric current injected directly into the melt and a perpendicularly acting magnetic field density, whereby both fields were assumed to be independent of the flow in the loop. The fluid in the loop was considered to be driven by strongly localized heating and cooling sections. For a wide range of conditions instabilities were found which led to multiple-valued solutions. Furthermore, this model, in spite of its simplicity, revealed the significant influence of the Lorentz force on the flow. However, this model did not include some key attributes of convection rolls in glass melts, namely (i) the strong dependence of viscosity and electrical conductivity on the temperature which, in practice, can lead to variations by more than one order of magnitude; (ii) the non-circular shape of the convection rolls (cf. the experiments [36] and numerical simulations [27], Sec. 3.1); (iii) the absence of isothermal regions in convection rolls.

We now focus on the mentioned characteristics for convection rolls of glass melt (i)–(iii) and present a new model for the highly viscous fluid in a closed loop. Besides the imposed Lorentz force we will study the influence of the variation of electrical conductivity and viscosity on the flow. We will show how the setup of the loop – ranging from two hydrodynamically connected vertical branches to almost circular loops – can modify the flow as well. We will discuss separably the role of Lorentz force, temperature-dependent electrical conductivity and temperature-dependent viscosity.

3.2.1 Formulation of the problem

We consider a tube of circular cross section with the uniform radius R and the length $L \gg R$ bent to a closed loop with two vertical branches of the length l. The two branches are connected by two circular arcs with the arc radius r as shown in Fig. 3.19(a). We

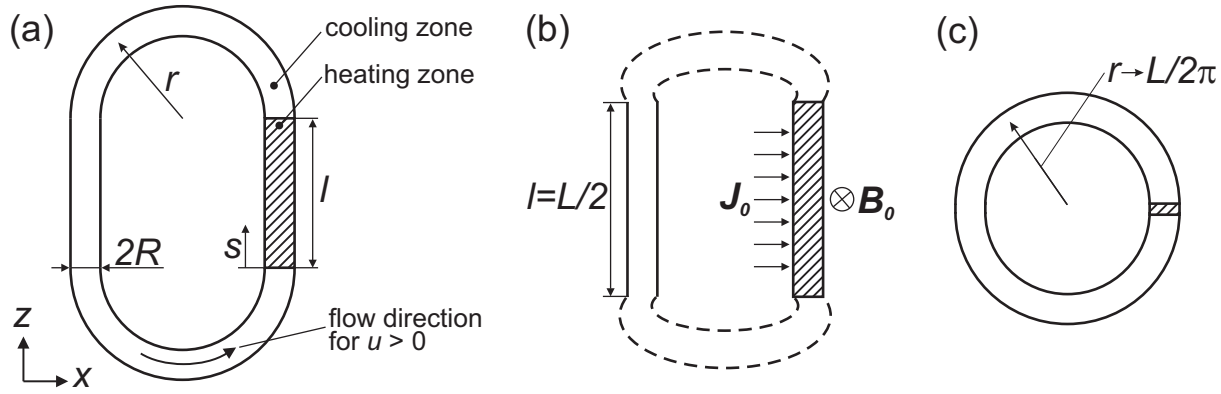

Figure 3.19: Sketch of the considered problem for (a) a loop with two vertical branches of the length l connected by two circular arcs with the arc radius r, (b) two hydrodynamically connected vertical branches with $r = 0$ and (c) a circular loop with $l \to 0$.

define the coordinate $s \in [0, L]$ with $L = 2l+2\pi r$ as the distance along the loop starting at the bottom of the right vertical branch. The variability of the aspect ratio r/l enables us to study loops of different shape including the limiting cases of two hydraulically connected vertical branches ($r = 0$ and $l = L/2$, see Fig. 3.19(b)) as well as a circular loop ($l \to 0$ and $r \to L/2\pi$, see Fig. 3.19(c)).

The loop is filled with a viscous fluid with constant heat capacity c_P representing molten glass. We invoke the generalized Boussinesq approximation and assume that the density of the fluid is constant in all governing equations except for the buoyancy term in the Navier-Stokes equation. Here it is assumed to depend linearly on temperature and to obey $\rho = \rho_0(1 - \beta T)$ with β representing the expansion coefficient and $T > 0$. This linearized equation of state is a good approximation for glass melts. Our temperature scale is defined in such a way that its zero corresponds to the freezing temperature of the glass melt under consideration. Although glass melts do not have a clearly defined freezing point, the motivation for our choice $T = 0$ as the freezing temperature will become clear shortly. We parenthetically note that we use the term *generalised Boussinesq approximation* in order to distinguish the present model which involves temperature-dependent viscosity and electrical conductivity (to be discussed below) from the usual meaning of the term Boussinesq approximation which implies that density is the only temperature-dependent property.

Glass melt is characterized by a highly non-linear temperature-dependent viscosity $\eta(T)$ and electrical conductivity $\sigma(T)$, where $\eta(T)$ is decreasing and $\sigma(T)$ is increasing with temperature. In glass science and engineering it is common to approximate these material parameters as exponential functions of the temperature being proportional to $\exp(1/T)$, Eqs. (1.6) and (1.7), respectively. But other functions like power laws fit the material property data equally well. Hence, we are free to choose the functional form of $\eta(T)$ and $\sigma(T)$ such that our analysis becomes most convenient. For reasons given below we use

$$\eta(T) = \eta_0 \left(\frac{T}{T_i}\right)^m, \quad m \leq 0, \tag{3.20}$$

with the viscosity parameters η_0 and m depending on the glass type. The normalization factor T_i is set to 1 K to assure that η_0, which does not have a physical meaning, is measured in units of the viscosity. Since $\eta \to \infty$ for $T \to 0$ it becomes clear that the temperature $T = 0$ can be regarded as the freezing temperature of the melt. Hence, the viscosity law, eq. (**??**), only makes sense for $T > 0$. We further assume

$$\sigma(T) = \sigma_0 \left(\frac{T}{T_i} \right)^n, \quad n \geq 0, \tag{3.21}$$

again with constant parameters σ_0 and n specific to the considered glass melt. For $m = n = 0$ the fluid has a constant viscosity, $\eta = \eta_0$, and a constant electrical conductivity, $\sigma = \sigma_0$, respectively. The advantage of our power laws is their convenient algebraic handling when integrations are necessary. By contrast, the more common models involving the temperature dependence $\exp(1/T)$ do not yield to an analytic integration.

On the right vertical branch of the loop, $0 \leq s \leq l$, a constant electric current density $\mathbf{J_0} = J_0 \mathbf{e_x}$ is applied and leads to a volumetric heat production according to J_0^2/σ. This part of the loop is referred to as the *heating zone*. In the remaining part of the loop, $l \leq s \leq L$, a constant heat transfer coefficient h is prescribed at the pipe walls. Therefore this branch is named *cooling zone*. The resulting temperature gradient along s leads to buoyancy driven convection in a counterclockwise direction. We further assume that a time-independent external magnetic flux density $\mathbf{B_0} = B_0 \mathbf{e_y}$, which is acting perpendicular to $\mathbf{J_0}$ in the right vertical branch, leads to a Lorentz force density $\mathbf{f_L} = J_0 B_0 \mathbf{e_z}$ in the melt. Depending on the direction of $\mathbf{B_0}$, the Lorentz force either reinforces or counteracts the thermal convection. For reasons given in Sec. 3.1.1, we neglect the induced current density and effects of viscous dissipation.

The aim of this work is to derive a simplified model that predicts the cross-section averaged velocity u and the cross-section averaged temperature distribution $T(s)$ in the loop. Since we assume that our glass melt is incompressible, u does not depend on s. By virtue of our assumption $L \gg R$, the one-dimensional model of the flow and heat transfer to be derived below, is expected to be sufficiently accurate, similar to previous works about thermal convection loops e.g. by [84], [16] and pipe flow e.g. presented in Chapter 2.

In general, the steady low-Reynolds number flow at hand is governed by the three-dimensional (3d) Stokes equation including Lorentz force and the 3d energy equation. For $L \gg R$ however, these equations can be reduced to a mathematical model that contains the coordinate s only. Since this approach has been extensively used in the past, we will not present the full derivation of the model here and refer the interested reader to the references [84], [16], [25] and [23]. The tangential component of the stationary cross-section averaged Stokes equation

$$\frac{dp}{ds} = (\mathbf{f_v} + \mathbf{f_b} + \mathbf{f_L}) \cdot \mathbf{e_s} \tag{3.22}$$

is the relevant source of information to derive our model. This equation expresses the balance between the viscous $\mathbf{f_v}$, buoyancy $\mathbf{f_b}$, and Lorentz $\mathbf{f_L}$ force densities on the one hand, and the pressure gradient dp/ds on the other hand. $\mathbf{e_s}$ is the unit vector tangential to the loop. Assuming a Poiseuille velocity profile, the viscous friction force becomes

$\mathbf{f_v} = -8u\eta(T(s))/R^2\mathbf{e_s}$. The buoyancy force is given by the equation $\mathbf{f_b} = \rho_0\beta g T(s)\mathbf{e_z}$, where g denotes the acceleration of gravity. The Lorentz force acts only within the heating zone ($0 \leq s \leq l$) and reads $\mathbf{f_L} = J_0 B_0 \mathbf{e_z}$.

To eliminate the pressure we integrate Eq.(3.22) from $s = 0$ to $s = L$. Making use of the uniqueness of the pressure expressed by $p(s + L) = p(s)$ we obtain

$$\frac{8u}{R^2}\int_0^L \eta(T(s))ds = \rho_0\beta g\int_0^L T(s)\mathbf{e_z}\cdot\mathbf{e_s}ds + J_0B_0l. \tag{3.23}$$

Eq.(3.23) expresses the balance between the integrated viscous friction on the left-hand side and the driving buoyancy and Lorentz force on the right-hand side. The integrated buoyancy term has to be evaluated separately for each branch as buoyancy acts along the gravitational field in $\mathbf{e_z}$-direction. In detail, the buoyancy term takes the form

$$\begin{aligned}\int_0^L T(s)\mathbf{e_z}\cdot\mathbf{e_s}ds \;=\; &\int_0^l T(s)ds + \int_l^{l+\pi r} T(s)\cos\left(\frac{s-l}{r}\right)ds \\ &- \int_{l+\pi r}^{2l+\pi r} T(s)ds - \int_{2l+\pi r}^{L} T(s)\cos\left(\frac{s-(2l+\pi r)}{r}\right)ds.\end{aligned}$$

To derive an equation for the one-dimensional temperature distribution $T(s)$ the heating and cooling zones have to be considered separately. In the heating zone there is no heat loss to the environment. Instead, the increase of the heat flux carried by the mean flow is equal to the volumetric heating due to the Joule effect. Neglecting effects of heat diffusion, the steady-state energy equation for the heating zone is thus

$$\rho_0 c_P u\frac{dT}{ds} = \frac{J_0^2}{\sigma(T)} \;\text{ for }\; s \in [0, l]. \tag{3.24}$$

In the cooling zone the decrease of the heat flux carried by the mean flow is equal to the heat loss through the side wall. This is expressed by the differential equation

$$\rho_0 c_P u\frac{dT}{ds} = -\frac{2h}{R}(T - T_\infty) \;\text{ for }\; s \in [l, L], \tag{3.25}$$

where T_∞ represents the ambient temperature. In the present work we set $T_\infty = 0$ to keep the model as simple as possible. With this simplification our model is a good approximation for the behavior of a streamline which passes through the immediate vicinity of a (cold) outer wall of a melting crucible which involves strong cooling. However, the present analysis can be generalized to nonzero values of T_∞. Such model would be appropriate to describe the behavior of an internal stream line with weak heat transfer. But nonzero values of T_∞ would restrict us to a numerical treatment of the basic equations (3.23)-(3.25) instead of an algebraic solution which is one goal of the present work and reachable with $T_\infty = 0$. As T_∞ of the 3d simulation in Sec. 3.1 is equal to 1393.15 K, the temperature T in the loop model represents an offset temperature. In comparison to the simulation it gives the difference between the temperature of the melt and $T_\infty = 1393.15$ K.

To match the first order differential Eqs. (3.24) and (3.25) the condition of continuity between the cooling and heating zone at $s = 0$ and $s = l$ has to be fulfilled for T. Once these equations have been solved for $T(s)$ we are able to evaluate the integrals in the Stokes equation (3.23), which then becomes an algebraic equation to determine u.

We non-dimensionalize the governing Eqs. (3.23)-(3.25) using the loop length L as a measure for all geometry parameters, i.e.:

$$s = s'L, r = r'L, l = l'L \text{ and } R = R'L.$$

Furthermore we use following scales for the velocity u and temperature T:

$$u = u'u_0, \text{ with } u_0 = \frac{8\eta_0 L}{R^2\rho_0} \text{ and } T = \theta T_0, \text{ with } T_0 = \left(\frac{J_0^2 R^2 T_i^n}{8\eta_0\sigma_0 c_P}\right)^{\frac{1}{1+n}}.$$

After substituting these definitions in Eqs. (3.23)-(3.25) and dropping the primes, we obtain the Stokes equation in the form

$$u\int_0^1 \theta^m(s)ds = \mathrm{Gr}\int_0^1 \theta(s)\mathbf{e_z}\cdot\mathbf{e_s}ds + M, \tag{3.26}$$

where

$$\mathrm{Gr} = \frac{\beta g\rho_0^2 R^4 T_0}{64\eta_0^2 L}\left(\frac{T_0}{T_i}\right)^{-m} \tag{3.27}$$

is the modified Grashof number which represents the ratio of the square of the viscous diffusion timescale to the square of the free-fall velocity timescale. Moreover,

$$M = \frac{J_0 B_0 l R^4 \rho_0}{64\eta_0^2 L^2}\left(\frac{T_0}{T_i}\right)^{-m} \tag{3.28}$$

is the modified interaction parameter which can be regarded as the ratio of the Lorentz force to the viscose force. Let us stress that Gr and M already include the dependence of viscosity and electrical conductivity on temperature as these parameters are proportional to $(T_0/T_i)^{-m}$. The energy equation for the heating zone becomes simply

$$u\frac{d\theta}{ds} = \theta^{-n}, \tag{3.29}$$

and the energy equation for the cooling zone becomes

$$u\frac{d\theta}{ds} = -N\theta, \tag{3.30}$$

where

$$N = \frac{hR}{4\eta_0 c_P} \tag{3.31}$$

is the wall heat loss parameter of the cooling zone. The integration of the non-dimensional energy equations (3.29) and (3.30) gives the solution for the temperature distribution

$$\theta(s) = \left[(g\exp\varepsilon)^{n+1} + \frac{n+1}{u}s\right]^{\frac{1}{n+1}} \quad \text{for } s \in [0, l], \tag{3.32}$$

$$\theta(s) = g \exp\left\{-\frac{N}{u}(s-l)\right\} \quad \text{for} \quad s \in [l,1], \tag{3.33}$$

with

$$\epsilon = -\frac{N}{u}(2\pi r + l), \quad g = \left\{\frac{l(n+1)}{u(1-(\exp\epsilon)^{n+1})}\right\}^{\frac{1}{n+1}}.$$

The substitution of Eqs. (3.32) and (3.33) in Eq. (3.26) leads, after some elementary calculations, to the following algebraic form of the momentum equation

$$\begin{aligned} ug^m \left\{\frac{n+1}{n+m+1} l \frac{1-(\exp\epsilon)^{n+m+1}}{1-(\exp\epsilon)^{n+1}} + \frac{u}{mN}\left[1-(\exp\epsilon)^m\right]\right\} \\ = \mathrm{Gr} g \left\{\frac{Nr^2/u}{(Nr/u)^2+1}\left[1+\exp\epsilon_1 - \exp\epsilon_2 - \exp\epsilon\right] + \frac{u}{N}\left[\exp\epsilon_2 - \exp\epsilon_1\right]\right. \\ \left. + \frac{n+1}{n+2} l \frac{1-(\exp\epsilon)^{n+2}}{1-(\exp\epsilon)^{n+1}}\right\} + M, \end{aligned} \tag{3.34}$$

with $\epsilon_1 = \exp(-Nr\pi/u)$, and $\epsilon_2 = \exp(-N(r\pi + l)/u))$. Eq. (3.34) expresses the balance between the braking friction force on the left hand-side and the buoyancy and Lorentz force on the right hand-side. As $\mathrm{Gr} \geq 0$, the buoyancy force drives the fluid always into a counterclockwise direction which corresponds to $u > 0$. The interaction parameter M can have both, positive or negative sign. Therefore, the Lorentz force reinforces buoyancy for $M > 0$ with $u > 0$ or counteracts the buoyancy when $M < 0$. The algebraic equation (3.34) is our desired model which we can use to calculate easily the velocity u as a function of the modified Grashof number Gr, the interaction parameter M, the cooling parameter N, the electrical conductivity parameter n, the viscosity parameter m, and the aspect ratio r/l with $2\pi r + 2l = 1$.

The rest of the present section is devoted the treatment of Eq. (3.34). We apply a simple root finding procedure on Eq. (3.34) to obtain u.

3.2.2 Results

The purpose of our investigation is to understand how buoyancy driven flow of a fluid with constant material properties is modified if (i) a Lorentz force is applied, (ii) the electrical conductivity, and (iii) the viscosity become temperature-dependent, respectively. In practice, all these three effects are present simultaneously. However, we believe that in order to develop a systematic understanding of the interplay of these effects it preferable to study first the effect of Lorentz force on a fluid with constant material properties and then investigate the effects of temperature-dependent electrical conductivity and viscosity separately. This will be done next.

Influence of Lorentz force

First we investigate a system with constant material properties, $n = m = 0$, and study the influence of the Lorentz force. In Fig. 3.20(a) the mean velocity u is given as a

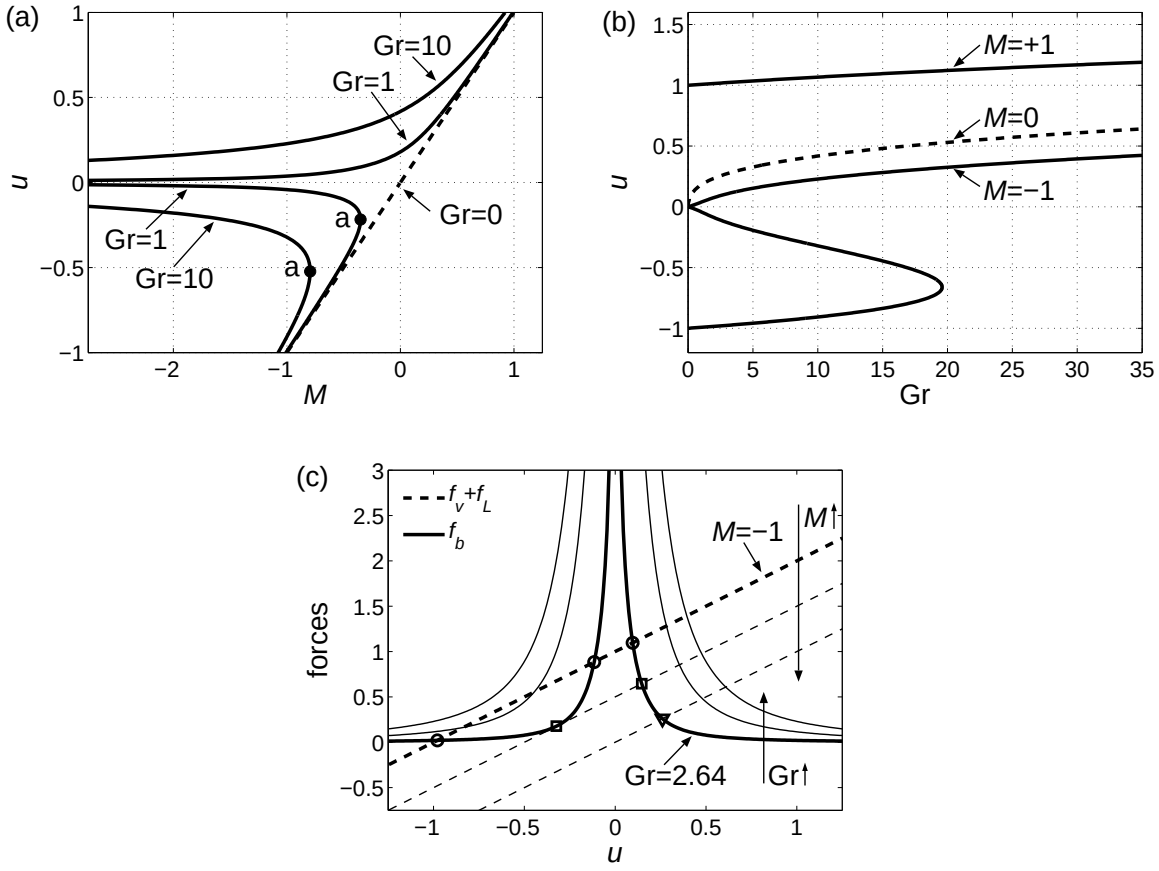

Figure 3.20: Influence of the Lorentz force on a system with constant material properties $n = m = 0$ and $l = 0.25$: the mean velocity u is plotted (a) as a function of the interaction parameter M for different Grashof numbers Gr and (b) as a function of Gr. (c) The intersection points of the buoyancy force f_b and the Lorentz and friction force $(f_v + f_L)$ give the solution of our governing eq. (3.34) for $\mathrm{Gr} = 2.64, 15, 30$ and $M = -1, -0.5, 0$. Depending on M we have one ($\bigtriangledown$), two ($\square$) or three (o) intersection points and therefore one, two or three solutions for the velocity u for a given set of parameters. For $M = 0$ we have no Lorentz force and for $M > 0$ ($M < 0$) Lorentz force and buoyancy act in the same (opposite) direction.

function of the interaction parameter M for different Grashof numbers Gr. If we neglect buoyancy, $\mathrm{Gr} = 0$, Eq. (3.34) reduces to $u = M$. This trivial solution which corresponds to electromagnetically driven flow of an isothermal fluid is shown by the dashed line in Fig. 3.20(a). The picture changes significantly if we "switch on" buoyancy ($\mathrm{Gr} > 0$), as was already found in GT5 for a circular loop. Indeed, $u(M)$ is now a multiple valued function for some values of the interaction parameter.

Let us first consider a system with positive velocities. (Remember that positive velocity corresponds to a flow in counterclockwise direction.) The key to the understanding of this phenomenon is the observation that for small positive velocities strong temperature gradients build up within the loop and lead to intensive buoyancy forces. In order to highlight this effect we plot the nondimensional buoyancy force as a function of the velocity

as a solid line in Fig. 3.20(c). This figure shows that f_b has a singularity for $u = 0$. The singularity of the buoyancy force for $u \to 0$ occurs for two reasons, namely neglect of heat conduction along the loop and the linearized density-temperature relationship used in the Boussinesq approximation. Indeed, since heat cannot be conducted in longitudinal direction and cannot escape from the insulated heating section, heat builds up without bound for $u \to 0$ which leads to $\theta \to 0$. If the exact relation $\rho(\theta)$ would have been used, ρ would tend to a small but finite value as $\theta \to \infty$ leaving the buoyancy force finite. Since we use the linearized relation $\rho = \rho_0(1 - \beta\theta)$, instead, $\rho \to \infty$ as $\theta \to \infty$ which gives rise to an infinite buoyancy force. Consequently, the behavior of $u(Gr, M)$ in Figure 3.20(a) should be considered as unphysical in the limit $M \to \infty$. If longitudinal heat conduction and non-Boussinesq effects were taken into account, the branches $u > 0$ and $u < 0$ for large negative M would be smoothly connected. Nevertheless it is interesting to see that a Lorentz force counteracting the buoyancy force cannot easily stop the flow. The solution $u(M)$ of eq. (3.34) shown in Fig. 3.20(a) can be graphically interpreted as the intersection of the curves f_b and $f_v + f_L$ as functions of u. As indicated in Fig. 3.20(c), an intensification of the counteracting Lorentz force (M < 0) leads to a shift of the intersection points along the right branch of f_b, but not to a change of the flow direction.

Let us now look at the regime with large and negative velocities which evolves from the dashed straight line in 3.20(a) for $M < 0$, if we switch on buoyancy. If we start from strong negative M and decrease the magnitude of this parameter, the magnitude of the mean velocity decreases also until the influence of buoyancy becomes relevant. For $u \to 0$ we find hot fluid just below and inside the heating zone and cold fluid in the cooling zone, hence a large buoyancy force builds up acting opposite to the flow direction. To obtain a stable system the driving Lorentz force has to increase very strongly. As a result we find a turning point in $u(M)$ for $u < 0$, labeled as a in Fig. 3.20(a). Altogether, for Gr > 0 the curve $u(M)$ splits into two branches: One the upper branch with $u > 0$, the velocity asymptotically reaches $u \to 0$ for $M \to -\infty$ and $u = M$ for $u \to \infty$. The lower branch with $u < 0$ runs from $u = M$ for $u \to -\infty$ over the turning point a to $u \to 0$ for $M \to -\infty$. For $M < M(a)$ three steady solutions for the velocity can be found for one set of parameters. The velocity as a function of Lorentz force was already studied in GT5 for $u \geq 0$ and a circular loop. A comparison shows that the results of both models agree quantitatively. The physical behavior is reproduced by both models. The results for negative velocities can not be compared as this parameter range has not been studied in GT5.

The multiple-valued character of u for M < 0 can also be observed if the mean velocity is plotted as a function of the Grashof number Gr as shown in Fig. 3.20(b). The curve for M = −1 develops two turning points and there exists a range of Gr numbers over which three steady states can be found. Between the two turning points we observe a counterintuitive behavior – the magnitude of the clockwise buoyancy force increases as well. On the upper branch we have $u > 0$ for all Gr > 0. On the lower branch we have $u < 0$ as the clockwise acting Lorentz force is the dominating driving force. Here the absolute value of the velocity decreases with Gr as buoyancy increases until the turning point is reached. If we incidentally increase Gr, buoyancy predominates $f_b > f_L + f_v$ and no equilibrium is reached, see e.g. Fig. 3.20(c). The fluid slows down, buoyancy increases as the temperature gradient increases and leads to an amplification of the slow down

process. After the change of the flow direction buoyancy decreases with velocity until the balance between the forces is reached. This change of flow direction appears in $u(\mathrm{Gr})$ as a jump from the inflexion point of the lower branch with $u < 0$ to the upper branch with $u > 0$. The upper and the lower branches of the curve $u(\mathrm{Gr})$ are stable while the middle branch is unstable. This can be explained with reference to Fig. 3.20(c) as follows. Consider a state located on the downward sloping branch of the curve $u(Gr)$ for $M = 1$ which corresponds to clockwise motion. Let us assume that an external perturbation leads to slight shift of u in positive direction (i.e. from u to $u + du$ with $du > 0$) which corresponds to a weak 'kick' in counterclockwise direction. As the curve $f_b(u)$ in Fig: 3.20(c) shows, the buoyancy force will then change from f_b to $f_b + df_b$ with $f_b > 0$. This implies that the fluid will experience a force in positive (counterclockwise) direction which brakes the clockwise motion further. This closed-loop interaction reinforces the deviation of u from its initial state even further and signifies an unstable branch.

Temperature-dependent electrical conductivity

Now we turn our discussion to a circular loop, $2l \ll 1$, with temperature-dependent electrical conductivity, $n > 0$, and constant viscosity, $m = 0$. Fig. 3.21(a) shows u as a function of M for $\mathrm{Gr} = 10$ and various electrical conductivity parameters n. Let us first note that the dashed curve with $n = 0$ in Fig. 3.21(a) and the curve for $\mathrm{Gr} = 10$ in Fig. 3.20(a) follow the same characteristics and pertain to similar physical situations. However, the numerical values of both curves are not identical. This quantitative difference originates from the reduction of the length of the heating zone from $l = 0.25$ ($\mathrm{Gr} = 10$ in Fig. 3.20) to $l = 0.005$ ($n = 0$ in Fig. 3.21) which leads to a reduction of the heat input and hence, to a reduction of buoyancy. As a result, the velocity becomes smaller in a buoyancy dominated regime (e.g. $\mathrm{M} = 0$) and the turning point shifts to velocities with a smaller magnitude for the present system with $l = 0.005$.

Furthermore, Fig. 3.21(a) shows that the temperature-dependent electrical conductivity leads to a dramatic change of the flow characteristic $u(M)$. In the case $M < 0$ are regions where there exist three solutions for u. Such a multiple-valued solution can also be found if we plot u as function of the Grashof number Gr as it is done in Fig. 3.21(b). If the Lorentz force acts against buoyancy, $M < 0$, and M reaches a certain critical value, there is a range of Grashof numbers over which three steady states can be found for positive velocities, see the curve with $M = -1$ in Fig. 3.21(b). The curve develops two turning points, which are labeled with a and b in Fig. 3.21(b). We note that between these two points there are solutions for which the velocity decreases as the Grashof number increases. Without Lorentz forces, $M = 0$ (dashed line in Fig. 3.21(b)), u is a monotonic non-linear function of Gr and u increases with n as buoyancy increases, see Fig. 3.21(a).

An explanation of the triple-valued solution can be given with the help of the acting forces as functions of u. In Fig. 3.21(c) the sum of the braking friction and Lorentz force $f_v + f_L$ (dashed line) and the driving buoyancy f_b (solid line) for different Gr numbers are given. For $u/|M| > 1$ the friction force gives the dominating contribution to the braking forces $f_v \gg f_L$ with $f_v = u$. For $u/|M| < 1$ we have $f_L = M$ as the Lorentz force dominates $f_L \gg f_v$. Interestingly, however, buoyancy $f_b(u)$ turns out to be not a monotonically

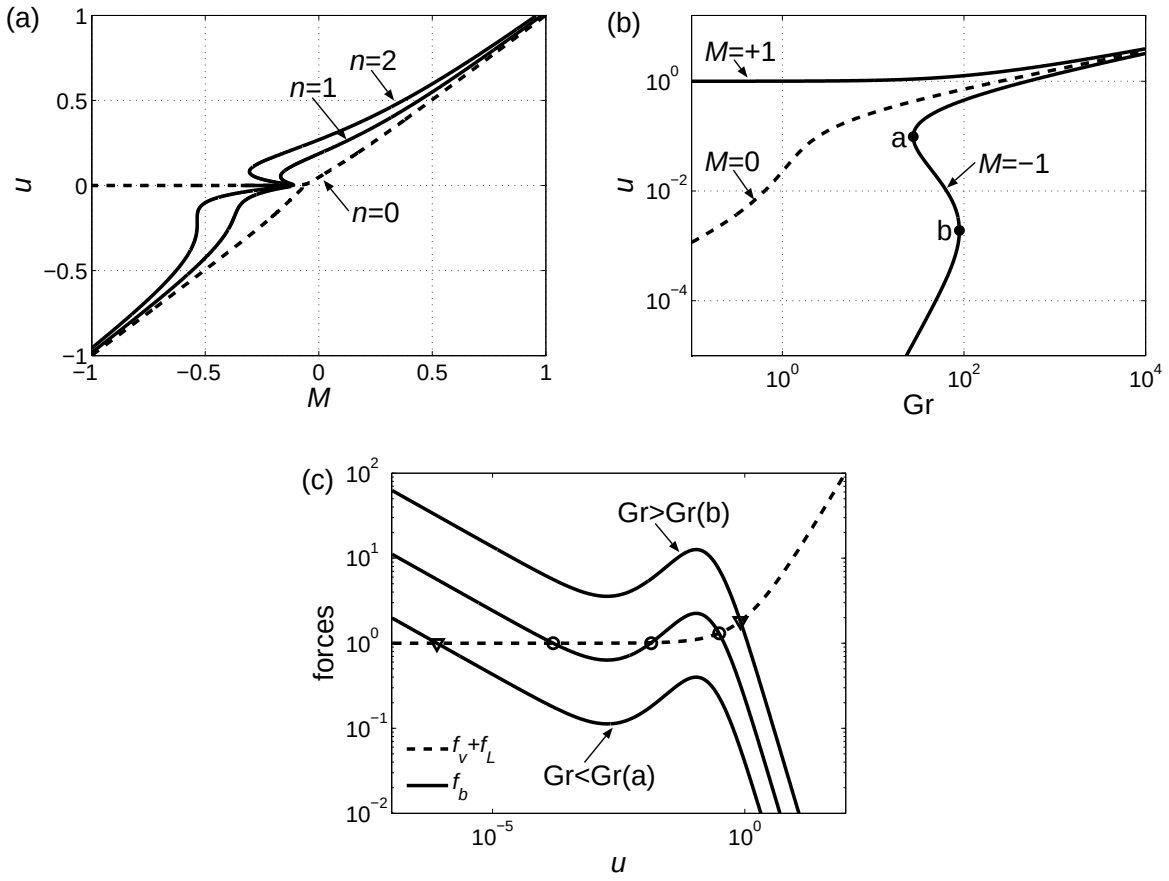

Figure 3.21: The flow characteristics (a) $u(\mathrm{Gr})$ and (b) $u(\mathrm{Gr})$ show the influence of the Lorentz force on a nearly circular loop with $l = 0.005$ and temperature dependent electrical conductivity. We have chosen the values for $N = 1$ and (a) $\mathrm{Gr} = 10$, (b) $n = 2$. For counteracting Lorentz force, $M < 0$, multiple-valued solutions can be observed. (c) The intersection points of the driving buoyancy force f_b (-) and the braking forces friction and Lorentz $f_v + f_L$ (- -) with $M = -1$.

decreasing function of u. Instead we find $f_b(u)$ increasing with u for a certain limited range of u. Depending on Gr, which leads to a shifting of the curve $f_b(u)$, we have one or three intersection points, as shown in Fig. 3.21(c).

To reveal those parameters with dominant influence upon the characteristics of the buoyancy force, let us study the asymptotic expression of $f_b(u)$ for $u/N \ll 1$. It can be readily verified that this expression is

$$f_b(u) = \left(l\frac{n+1}{u} \right)^{\frac{1}{n+1}} \left(\frac{n+1}{n+2} l + \frac{u}{N} \right). \tag{3.35}$$

For $l(n+1)/(n+2) \gg u/N$ we have $f_b \sim u^{-\frac{1}{n+1}}$. In this regime the fluid is cooled down to the ambient temperature as soon as it enters the cooling section at $s = l$. Therefore we have "hot" fluid in the heating zone and "cold" fluid in the cooling zone.

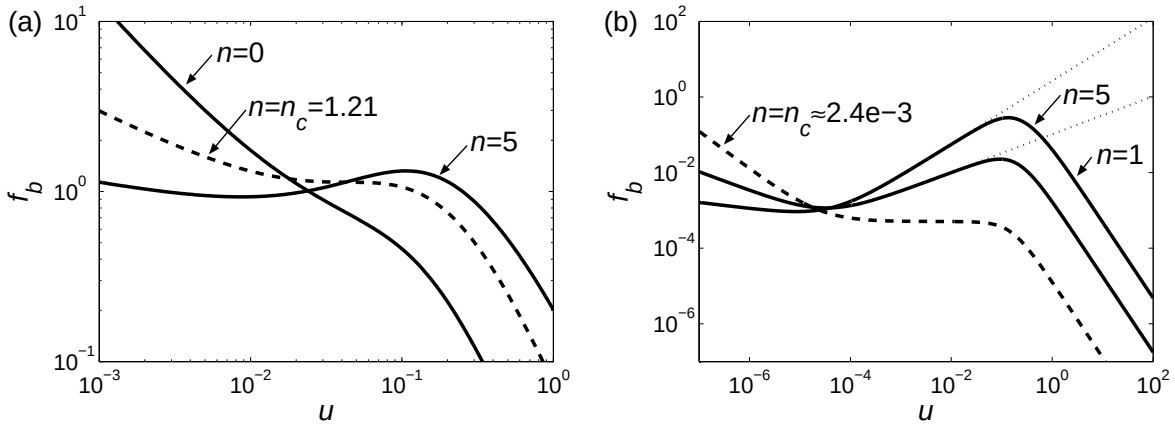

Figure 3.22: The buoyancy force density f_b as a function of the dimensionless velocity u is given for various electrical conductivity parameters n and different length of the heating section, namely (a) $l = 0.05$ and (b) $l = 1e-5$. For n exceeding a critical value n_c buoyancy increases with u, whereas $n_c \to 0$ for circular loops with $l \to 0$, Fig. (b). In this case we find the relation $f_b \sim u^{\frac{n}{n+1}}$ for all $n > n_c$ (dotted lines).

Buoyancy is mainly determined by the temperature at the outlet of the heating section $\theta(l)$, which scales as $\theta(l) \sim u^{-\frac{1}{n+1}}$ for all $u/N \ll 1$ as well. The temperature $\theta(l)$ – and hence the buoyancy – decreases with increasing u as the heat input in the heating zone decreases. As the heat input increases with n due to the stronger dependence of the electrical conductivity on temperature, the function $\theta(l, u)$ – and hence also $f_b(u)$ – flattens with increasing n, see left part of the curves in Fig. 3.22.

With the increase of u/N, we reach a regime, where the fluid is not cooled to the ambient temperature as soon as it enters the cooling section. We find "warm" fluid in the upper half-circle of the loop $l \le s \le l + r\pi/2$ which has an additional contribution to the buoyancy force. Therefore $f_b(u)$ flattens and the proportionality $f_b \sim u^{-\frac{1}{n+1}}$ is left. If we now assume $l \ll 1$, the condition $l(n+1)/(n+2) \ll u/N \ll 1$ is satisfied and Eq. (3.35) simplifies to $f_b \approx [l(n+1)/u]^{1/(n+1)} \cdot u/N$. For a nearly circular loop we find an increase of buoyancy according to $f_b \sim u^{\frac{n}{n+1}}$. In this case the additional buoyancy in the circular arcs is larger than the reduction of buoyancy due to the decrease of $\theta(l)$ with u.

This mechanism of increasing buoyancy is the result of the delicate interplay between (i) temperature-dependent heat input, which is mainly described by n, and (ii) the aspect ratio of heating and cooling zones r/l, with $2\pi r + 2l = 1$, which can be described by l, and (iii) the cooling rate, which is described by N. As the buoyancy in the cooling section is proportional to the temperature reduction of $\exp(-N/u)$ and the length of the circular arcs, and $\theta(l) \sim u^{-\frac{1}{n+1}}$, the electrical conductivity parameter n needs to exceed a certain critical value n_c for a given N and l. Fig. 3.22(a) shows the influence of n on f_b for $l = 0.05$. For $n < n_c = 1.21$ the curve $f_b(u)$ flattens, but $f_b(u)$ does not increase with u. For $n > n_c$ $f_b(u)$ grows with u, but the relation $f_b \sim u^{\frac{n}{n+1}}$ is not fulfilled as we do not have $l \ll 1$. The case $l = 1e-5 \ll 1$, representing a circular loop with $n_c = 2.38e-3 \approx 0$, is given in Fig. 3.22(b). The electrical conductivity only needs to depend slightly on

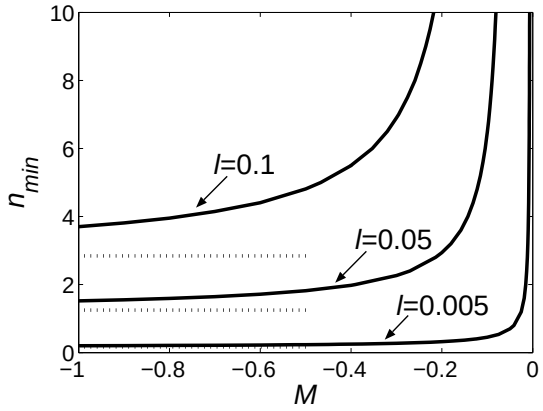

Figure 3.23: The minimum electrical conductivity parameter n_{min} required to give multiple solutions is plotted as function of the interaction parameter M for different values of the length of the heating section l with $N = 1$. The dotted lines indicate n_c for each l.

temperature and we find an increase of buoyancy. The scaling $f_b \sim u^{\frac{n}{n+1}}$ is also fulfilled as indicated by the dotted lines. In general, the smaller l the smaller n_c as the influence of buoyancy in the upper circular arcs increases. Besides the increase of buoyancy, we need to have counteracting Lorentz force to obtain multiple solutions. We can not achieve three intersection points between buoyancy f_b and friction f_v as $f_v \sim u$ and the upper bound for the increase of f_b is $f_b \sim u^{\frac{n}{n+1}}$ with $u^{\frac{n}{n+1}} < u$. Therefore, the intersection parameter M is an additional parameter which has influence on the onset of the non-unique flow behavior.

In order to better understand the parameter dependence of the bifurcations we have numerically evaluated the smallest electrical conductivity parameter n_{min} that will give rise to multiple solutions as a function of the interaction parameter M for various length of the heating section l. The results are shown in Fig. 3.23. For $l = 0.1$ a strong non-linear dependence of the electrical conductivity on temperature and high absolute values of counteracting Lorentz forces |M| are required to achieve non-unique behavior. In contrast, for a nearly circular loop ($l \to 0$), non-unique solutions can be obtained for small n_{min} and small |M|. The dotted lines give the critical value n_c above which buoyancy increases with u. For $\mathrm{M} \to -\infty$ the minimum electrical conductivity parameter n_{min} reaches n_c for all $l < 0.5$.

Temperature-dependent viscosity

In the present paragraphs we concentrate our attention on a system with temperature-dependent viscosity, $m < 0$. In this case only the structure of the friction force changes from $f_v = u$ for $m = 0$ to $f_v = u f_1(u, N, n, m)$ for $m < 0$ with $f_1 \sim 1 - \exp(-N/u)^m$, see Eq. (3.34). For about $u/N < 10^{-3}$ the value of $\exp(-N/u)$ is less than the smallest value we can represent with the used code. Therefore, our studies for temperature dependent viscosity are restricted to $u/N > 10^{-3}$.

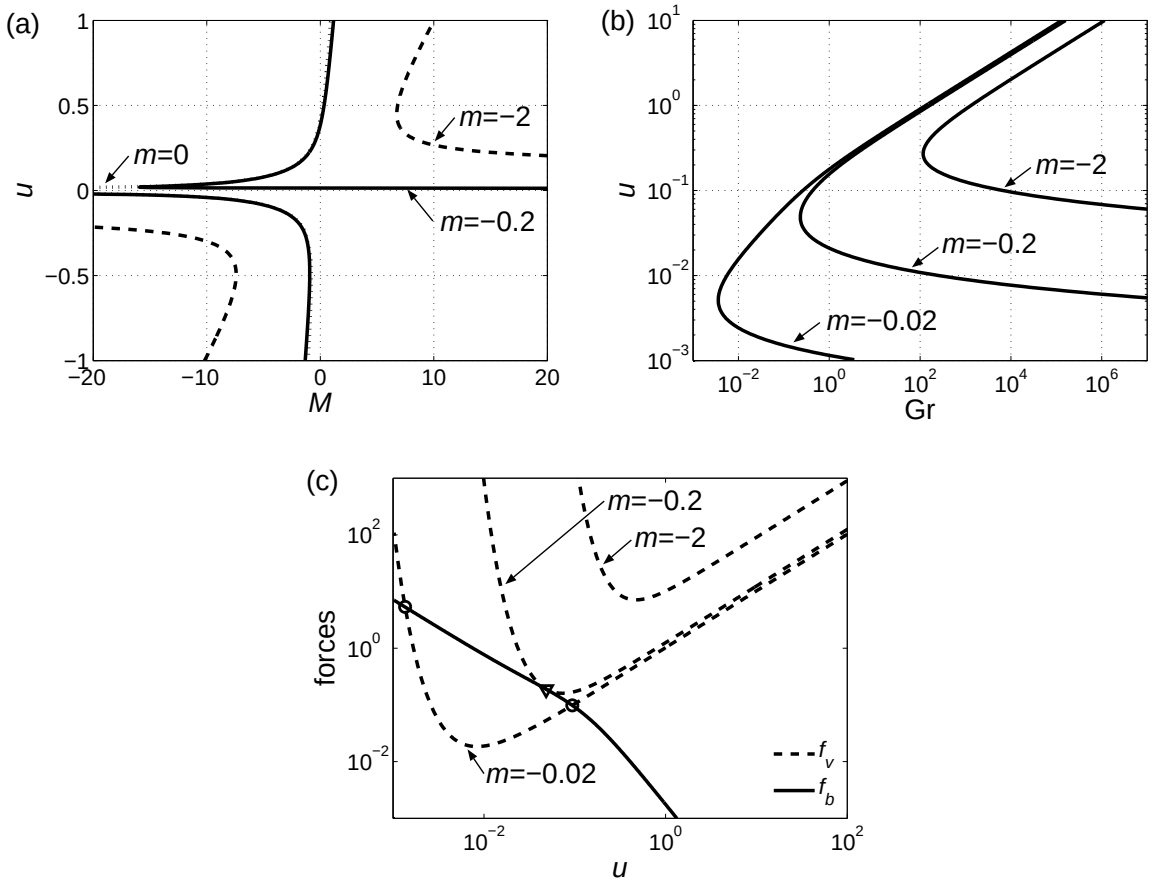

Figure 3.24: The dimensionless velocity u as a function of (a) the interaction parameter M with $\mathrm{Gr} = 10$ and (b) the Grashof number Gr for a system without Lorentz force $M = 0$ for different values of the viscosity parameter m with $n = 0$, $N = 1$, $l = 0.25$. (c) The corresponding force distribution for (b) of the the driving buoyancy f_b (-) and braking friction force f_v (- -) for $\mathrm{Gr} = 0.23$ as function of u for different viscosity parameters m. As the friction force has a parabolic-like profile we obtain two (o), one ($\bigtriangledown$) or no intersection points between f_b and f_v.

If the regime of constant viscosity with $m = 0$ is left, $u(M)$ changes qualitatively as it is shown in Fig. 3.24(a). For moderate m (e.g. $m = -0.2$) there is virtually no difference between the temperature-dependent and the constant viscosity on the lower branch with $u < 0$. By contrast, on the upper stable branch with $u > 0$ we find a turning point such that $u \to 0$ for $M \to +\infty$ and we have four values for u for one M. If the dependence of viscosity on temperature is strong (e.g. $m = -2$), the graph resembles a hyperbola. For a given Gr we need a certain $|M|$ to obtain a solution.

To understand this observation, let us study the mean velocity u as function of Gr for different viscosity parameters m and no Lorentz force ($M = 0$). Fig. 3.24(b) shows that the temperature dependent viscosity separates the parameter space into three regimes: (i) the stagnant regime, (ii) the single-valued regime and (iii) the double-valued regime. The single-valued regime – characterized by a single velocity as solution for a given set of parameters – can only be obtained for a certain Grashof numbers, which we also denote as

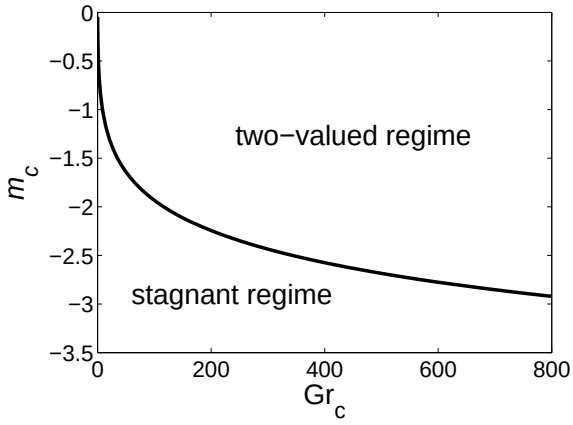

Figure 3.25: The phase diagram gives the region of parameters in which the fluid is immobilized – stagnant regime – and in which two solutions do coexist – two-valued regime – for $M = n = 0$, $N = 1$ and $l = 0.25$. Both regimes are separated by the one valued regime which is characterized by critical Grashof number $\mathrm{Gr_c}$ (solid line).

the critical Grashof number $\mathrm{Gr_c}$. This point in the parameter space forms the overturning point of $u(\mathrm{Gr})$. If the Grashof number exceeds this critical value, i.e. $\mathrm{Gr} > \mathrm{Gr_c}$, we reach the double-valued regime and obtain two velocities for one given Gr. Here, for large velocities, u is a increasing function of Gr as it is known from thermal convection. For small velocities, however, u decreases with increasing Gr. For $\mathrm{Gr} < \mathrm{Gr_c}$ we did not found a solution at all. The phase diagram in Fig. 3.25 summarizes the region of parameters for all three regimes (i)-(iii).

The reason for the stagnant regime is the shape of the friction force given in Fig. 3.24(c). For large velocities we have small temperature differences and therefore small viscosity differences within the loop. The friction force is proportional to u. In the case of small velocities the temperature in the cooling zone tends to $\theta \to 0$ and hence, the viscosity leads to $\eta \to \infty$. Thus, the friction force f_v strongly increases with decreasing u. As a result $f_v(u)$ has a parabola-like shape with a minimum friction force. As the buoyancy curve is monotonically decreasing with u, we obtain two, one or none intersection points and therefore two, one or no solution as shown in Fig. 3.24(c).

From the two intersection points only the right one is stable and hence, only the upper branch of the two-valued solution is stable. Any u that is slightly above the lower branch will drive the system to the upper stable branch while any u slightly below the lower branch will initiate freezing of the system. Such freezing is not necessarily a contraction. It has been observed for forced convection of glass melt in a pipe in industrial processing and was confirmed theoretically [48], [24]. In practice freezing typically occurs if the melt is cooled by room temperature (for which $\eta \to \infty$) and if the velocity is below a critical value. In a convection cell, a stagnant layer develops and the motion shifts away from the cold walls. In glass processing such a behavior is used in cold induction crucibles to minimize corrosion at the crucible wall. As the fluid motion in the model is restricted to a defined path, the loop can not reflect the structural modification of convection cells which is a limit of the thermosyphon approach in general. However, a second stable branch of

u(Gr), Fig. 3.24(a), exists theoretically. We would be able to calculate this branch, if η would have a finite value for θ_∞. This could be realized for example with the present viscosity law, equation (**??**), and $\theta_\infty > 0$. In this case the friction law $f_v(u)$ would obtain a third branch for $u \to 0$ for which f_v is a linear function of u and one would obtain 1 to 3 intersection points.

3.3 Comparison between numerical, analytical, and experimental results

In the previous sections 3.1 and 3.2 we have presented parameter studies for electromagnetically driven convection of molten glass in a crucible by three-dimensional numerical simulations and by one-dimensional modeling. Now we compare the results of these two approaches with each other. Furthermore, we link the results with the experimental data obtained by Krieger, which are published in [42]. The comparison between the experiment and the numerical simulation is straight forward as the geometry and the boundary conditions of the numerical model meet the experimental setup. But the comparison with the results of the analytical model requires some adjustments of the model parameters and the transformation of the material property laws from the common exponential formulation, Eqs. (1.6), (1.7), into the power law formulation, Eqs. (3.20) and (3.21). Therefore, we first describe these adjustments and then present some results of glass melt flow in the one-dimensional loop given in SI units. Afterwards, we compare all approaches with each other.

3.3.1 Adjustment of model parameters and material property laws

Even though the 1d analytical loop model is inspired by the 3d crucible configuration and captures the main physics of the system, the reduction from the 3d setup to the 1d system leads to some differences between both approaches and requires the adjustment of some parameters. These parameters are the geometry parameters of the loop which represents the vortex flow in the crucible. We also have to adjust the current density J_0, the magnetic flux density B_0, and the heat transfer coefficient h. In the loop model J_0 and B_0 are applied in the heating zone only, whereas the current density J and B_0 capture the total volume of the melt of the 3d configuration. Additionally, J_0 is constant in the 1d model whereas J varies within the melt of the 3d configuration. Furthermore, the heat transfer to the surrounding is realized by convective cooling only. But in the 3d setup we have radiative heat transfer at the free surface beside convective transfer at the crucible wall. Therefore, the heat transfer coefficient has to be modified to meet roughly the overall heat loss of the 3d configuration. For a detailed comparison of the geometry and model parameters we refer to Figs. 3.1, 3.2, 3.19 and Secs. 3.1.1, 3.2.1, respectively. Overall, many possibilities exist to adjust the mentioned model parameters of the loop. In the following we sketch the possibility which we have used for our calculations. We do not claim that it is the one and only parameter adjustment.

We have performed the calculations with the following loop geometry parameters: length of the heating zone $l = 0.04$ m, arc radius $r = 0.02$ m, and inner diameter of the pipe $d = 0.02$ m.

For the estimation of J_0 we start with the requirement that the total heat input $Q = J^2V/\sigma$ is equal for all approaches. We then assume that σ is the same in all approaches. In addition, the volume-averaged current density $\overline{J} = \int JdV/V$ is known. Consequently, we can approximate J_0 by the following relation:

$$J_0 = \sqrt{\frac{V}{V_0}} \cdot \overline{J} = 2.77\overline{J}, \tag{3.36}$$

with V being the volume of the melt in the 3d crucible, and V_0 being the volume of the heating zone. $\overline{J}$ can be calculated easily in the numerical simulation. From the experiment we just know the magnitudes of the current I and U_E which are applied at the electrodes. Here we propose to calculate $\overline{J}$ on the basis of the total heat input $Q = IU_E$ according to $\overline{J} = \sqrt{Q\sigma/V}$. Due to its dependence on the temperature the electrical conductivity σ is the critical parameter of this relation. Only the knowledge of the operating temperature range can lead to a coarse estimation of σ.

Furthermore, we propose a volume-weighting of the magnetic flux densities for the adjustment of B_0. To distinguish between the magnetic flux densities of the 1d and the 3d configuration, henceforth we denote $B_{0,1d}$ as the density of the 1d model and $B_{0,3d}$ as the density of the 3d configuration. Hence,

$$B_{0,1d} = \frac{V}{V_0} \cdot B_{0,3d} = 7.68B_{0,3d}. \tag{3.37}$$

To adjust the heat transfer coefficient h we first determine the heat radiation q_{rad} according to $q_{rad} = \sigma\epsilon(T^4 - T_\infty^4)$ with $T_\infty = 1393.15$ K and $\Delta T = T - T_\infty = 50$ K. Then we estimate the heat transfer coefficient h_{rad}, which leads to the same heat loss $q_{rad} = h_{rad}\Delta T$. Furthermore, we assume that radiation takes place at a half of the upper circular arc with a length of $s_{rad} = \pi r/2$. At the remaining parts of the cooling zone with a length of $s_{conv} = 3\pi r/2 + l$ we have pure convection which is specified by the heat transfer coefficient h_{conv}. Now the overall heat transfer coefficient h of the cooling zone of the loop is length-weighted and calculates from

$$h \approx \frac{h_{conv}s_{conv} + h_{rad}s_{rad}}{s_{conv} + s_{rad}} \approx 77\frac{\mathrm{W}}{\mathrm{m^2K}}. \tag{3.38}$$

For the adjustment of the material properties let us remember that we have set the ambient temperature T_∞ to zero in the loop model and to 1393.15 K in the simulation and experiment. Hence, the loop model gives an offset temperature which is the difference between the temperature of the melt and 1393.15 K. If this offset temperature tends to zero, the power law formulation of the material properties which we used in the analytical model tends to $\eta \to \infty$ and $\sigma \to 0$ according to Eqs. (3.20) and (3.21). However, in reality and with the exponential formula, Eqs. (1.6) and (1.7), both properties have a finite non-zero magnitude as soon as the melt temperature tends to 1393.15 K. Hence,

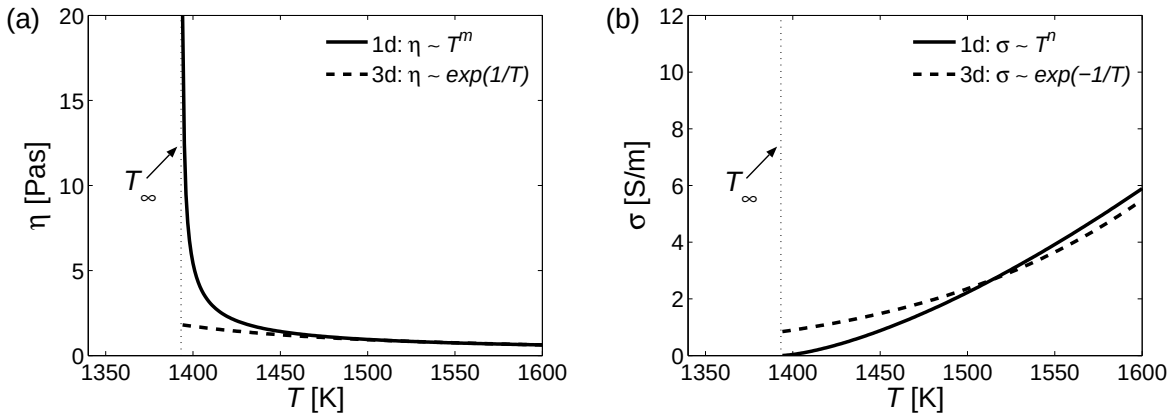

Figure 3.26: Material property laws of (a) the viscosity $\eta(T)$, and (b) the electrical conductivity $\sigma(T)$ for *glass 3* in potential and exponential formulation according to Eqs. (3.20), (3.21) and Eqs. (1.6), (1.7), respectively. The numerical values of both formulations are given in Eqs. (3.39)-(3.40) and Tab. A.2.

we observe a large deviation between the potential and the exponential description for $T \to T_\infty$ as it is shown in Fig. 3.26. These deviations strongly depend on the exponents m and n of the power law formulation. Let us emphasize that for $T \to T_\infty$ η tends to ∞ and leads to an overestimation of the friction force which is breaking the flow. At the same time σ tends to zero for $T \to T_\infty$ and results in an overestimation of the volumetric heat input and hence, an overestimation of the driving buoyancy force. Without performing detailed calculations we can assume that both effects compensate each other. Like for the geometry parameters, J_0, B_0, and h, different possibilities exist to obtain the potential material property laws for $\eta(T)$ and $\sigma(T)$. We have chosen the formulations which provide the minimum least square error to the original exponential material property laws between the offset temperatures 100 K and 400 K. Hence, we have

$$\eta(T) = 18.42\text{Pas}\left(\frac{T}{\text{K}}\right)^{-0.635}, \tag{3.39}$$

$$\sigma(T) = 2.3 \cdot 10^{-3}\text{S/m}\left(\frac{T}{\text{K}}\right)^{1.472}, \tag{3.40}$$

with T being the offset temperature of the system.

3.3.2 Sample calculations for the analytical model

Calculations of electromagnetical controlled flow in the closed loop with glass melt parameters result in the overlapping of various effects which we studied separately in Sec. 3.2.2. We observed multiple-valued solutions for the non-dimensional velocity-force characteristic $u(M)$ due to the imposed Lorentz force as pictured in Fig. 3.20. Furthermore, we found bifurcations due to the temperature-dependent electrical conductivity and due to

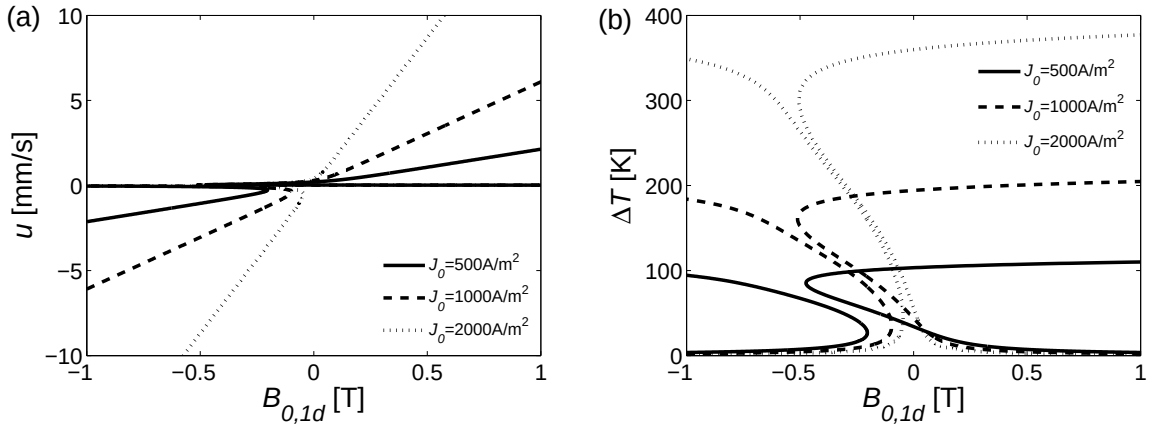

Figure 3.27: Sample calculations for the 1d analytical model for *glass 3* with $\eta(T)$ and $\sigma(T)$ being specified in Eqs. (3.39) and (3.40), the remaining material properties given in Tab. A.2, $h = 77$ W/m^{2}K, $l = 0.04$ m, $r = 0.02$ m, and $d = 0.02$ m: (a) mean velocity u, and (b) temperature difference $\Delta T = T_{max} - T_{min}$ as functions of the magnetic flux density $B_{0,1d}$.

the temperature-dependent viscosity, see Figs. 3.21, 3.24. The bifurcation based on $\sigma(T)$ appears, if the exponent n exceeds a minimum value n_{min}. As shown in Fig. 3.23 n_{min} depends on the dimensionless length of the heating section l and on the forcing parameter M.

In the present configuration the dimensionless length l is 0.194. To observe a '$\sigma(T)$-induced' bifurcation, n would have to be at least $n \geq n_c = 7.52$. We have not investigated this bifurcation in the present sample computations, i.e. we have not chosen the value of n_c.

Fig. 3.27(a) pictures the mean velocity u as a function of the magnetic flux density $B_{0,1d}$ for various current densities J_0. For a wide range of parameters the flow is dominated by the Lorentz force and u is a linear function of $B_{0,1d}$. As expected we observe one turning point for $u < 0$ in the graph $u(B_{0,1d})$. The position of the turning point shifts to larger $B_{0,1d}$ for increasing J_0. Due to the temperature dependency of η we observe a second turning point for $u > 0$ having little dependence on J_0. Additionally, the temperature difference $\Delta T = T_{max} - T_{min}$ as function of $B_{0,1d}$ is shown in Fig. 3.27(b). The left part of the curves correspond $u < 0$ in Fig. 3.27(a), whereas the right curves correspond to $u > 0$. In the Lorentz force dominated flow regime with $u \sim B_{0,1d}$ the temperature difference ΔT tends to zero as the residence time of the glass melt in the heating and cooling zone is very low. In contrast we observe large ΔT for $u \to 0$.

3.3.3 Comparison between numerical and analytical results

Now we compare the results of the 3d numerical simulations which we have already discussed in Sec. 3.1.3 with results of the 1d analytical model. The adjustment of the model parameters and material property laws are described in Sec. 3.3.1. Figs. 3.28 -

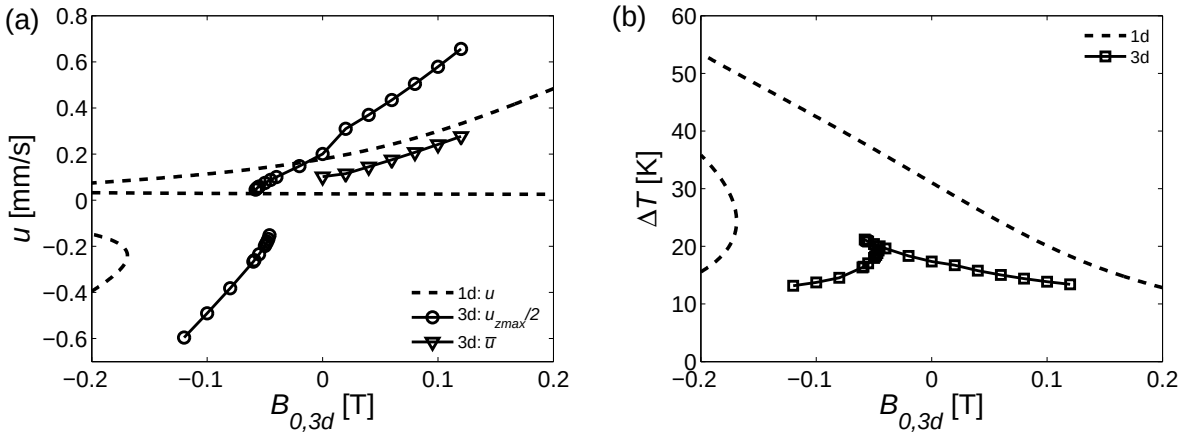

Figure 3.28: Results of 3d numerical simulations with $U_E = 9$ V compared to results of the 1d analytical model obtained with $J_0 = 387.8$ A/m^2, $B_{0,1d} = 7.68 B_{0,3d}$ and $h = 77$ W/m^{2}K. In (a) the velocity u in mm/s, and in (b) the temperature difference $\Delta T = T_{max} - T_{min}$ in K as functions of the magnetic flux density $B_{0,3d}$ are given. The results of the 3d numerical simulation are given in terms of one half of the maximum z-component of the velocity in the centerline of the crucible $u_{zmax}/2$ and the volume-averaged velocity $\overline{u} = \sqrt{\int |\mathbf{u}|^2 dV/V}$.

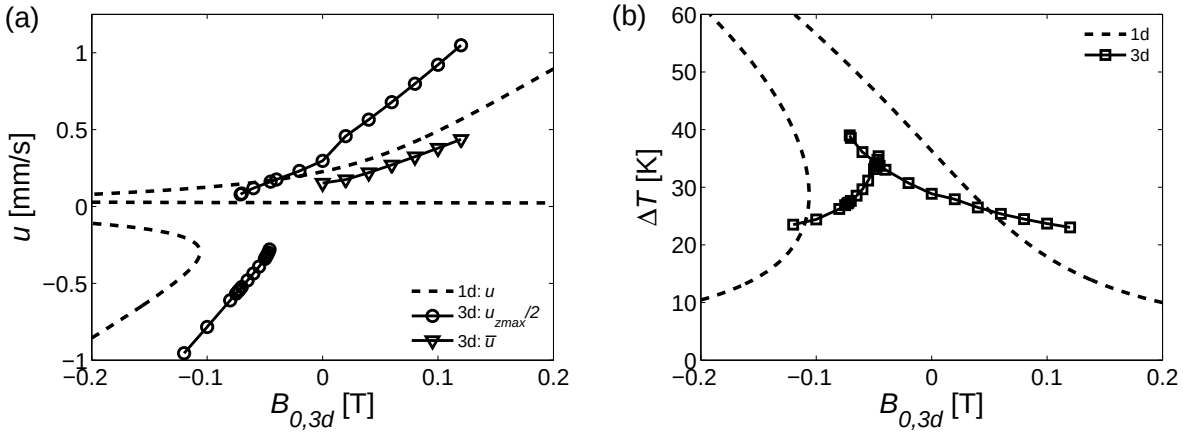

Figure 3.29: Results of 3d numerical simulations with $U_E = 12$ V compared to results of the 1d analytical model obtained with $J_0 = 596.9$ A/m^2, $B_{0,1d} = 7.68 B_{0,3d}$ and $h = 77$ W/m^{2}K.

3.31 give the velocity and the temperature difference ΔT as functions of the magnetic flux density for $U_E = 9$ V, 12 V, 15 V, and 18 V, respectively.

The velocity of the 3d numerical simulation is given in terms of the maximum z-component of the velocity in the centerline of the crucible $u_{zmax}/2$ and in terms of the volume-averaged velocity $\overline{u} = \sqrt{\int |\mathbf{u}|^2 dV/V}$ for $B_0 \geq 0$. Both characteristics differ in such a way that the steepness of $(u_{zmax}/2)(B_0)$ is larger than the steepness of $\overline{u}(B_0)$. Additionally, the magnitude of u_{zmax} is larger than the magnitude of $\overline{u}$ for a given B_0. For all U_E we

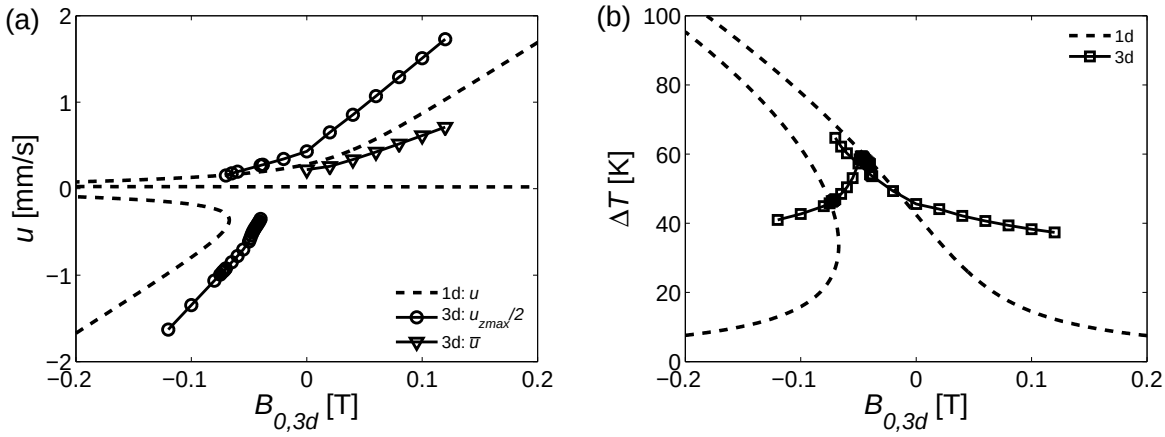

Figure 3.30: Results of 3d numerical simulations with $U_E = 15$ V compared to results of the 1d analytical model obtained with $J_0 = 915.5$ A/m^2, $B_{0,1d} = 7.68 B_{0,3d}$ and $h = 77$ W/m^{2}K.

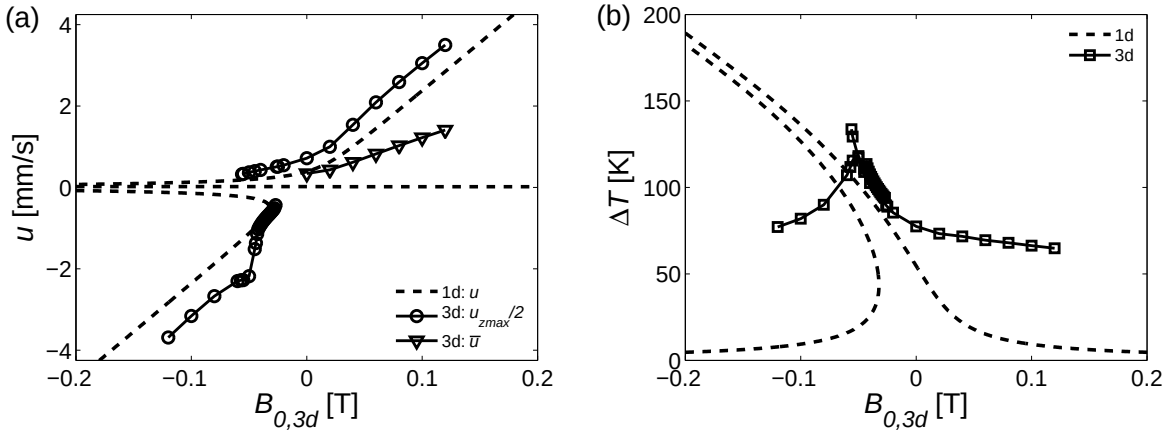

Figure 3.31: Results of 3d numerical simulations with $U_E = 18$ V compared to results of the 1d analytical model obtained with $J_0 = 1813$ A/m^2, $B_{0,1d} = 7.68 B_{0,3d}$ and $h = 77$ W/m^{2}K.

observe that the curves predicted by the 1d model $u(B_0)$ are surrounded by the curves $(u_{zmax}/2)(B_0)$ and $\overline{u}(B_0)$. Hence, the 1d model is overestimating $\overline{u}$ but smaller than $u_{zmax}/2$ and is predicting the tendency of the flow characteristic very well. Furthermore, for $U_E = 12$ V the steepness of $u(B_0)$ is similar to the steepness of $\overline{u}(B_0)$ and for $U_E = 18$ V it is comparable to that of $(u_{zmax}/2)(B_0)$. For $B_0 < 0$ the 1d model reflects the flow characteristic in the 3d crucible as well. This includes the upper stable branch with $0 < u$ and the lower stable branch with $u < 0$. Especially for $U_E = 18$ V the 1d model estimates the magnitudes of $u_{zmax}/2$ and the position of the turning point for $u < 0$ very well. But for reduced U_E we observe $|u| \ll |u_{zmax}/2|$.

The 1d model also predicts the range of temperature differences and the tendencies of $\Delta T(B_0)$ as shown in the right diagrams of Figs. 3.28 - 3.31. Again we find differences in the characteristics $\Delta T(B_0)$ depending on U_E. For $U_E = 9$ V ΔT is overestimated and for

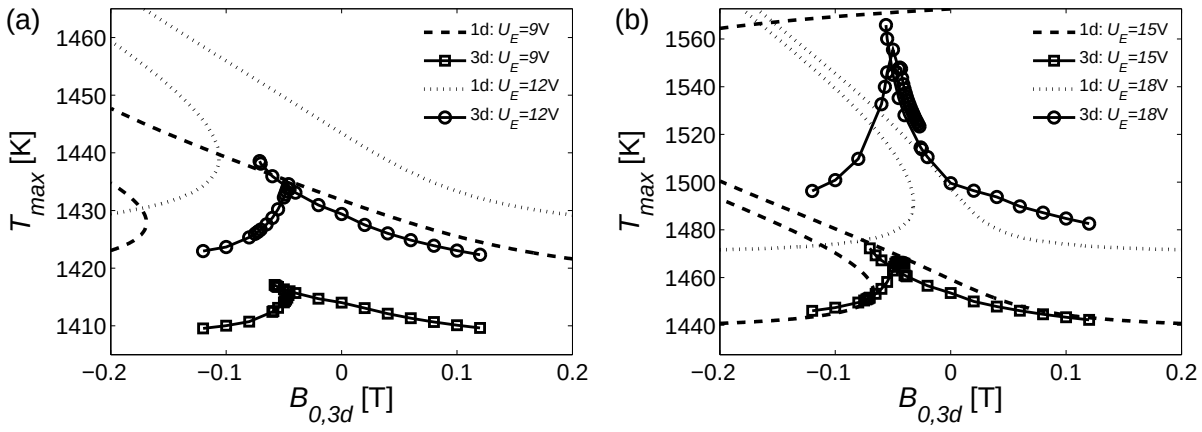

Figure 3.32: Maximum temperature T_{max} in the melt as function of the magnetic flux density B_0 calculated with 3d numerical simulations and 1d analytical modeling. The results correspond to the temperature curves in Figs. 3.28-3.31.

$U_E = 18$ V ΔT is underestimated by the 1d model. It is obvious that in the Lorentz force dominated regimes the steepness of $\Delta T(B_0)$ is much smaller regarding the results of the 3d simulations than those of the 1d analytical model.

An explanation can be given on the basis of the maximum temperature T_{max} which is shown as a function of B_0 in Fig. 3.32. Here, the steepness of the curves $T_{max}(B_0)$ in the Lorentz force dominated regimes are almost identical. Hence, the minimum temperature is not predicted correctly. In the 3d configuration we find the lowest temperatures on the free surface close to the crucible. In this area the fluid hardly moves and is independent of the main vortex velocities. The minimum temperature is almost independent of B_0. In contrast, the minimum temperature of the 1d model varies with the driving Lorentz force. An increasing velocity leads to a reduction of the heat loss and therefore an increase of T_{min}.

3.3.4 Comparison with experimental data

In the following section we compare the numerical and analytical results with the measured data from Krieger in [42]. Krieger managed to determine experimentally the velocity along the centerline of the crucible. He used the fact, that temperature fluctuations occur just after shifting the direction of the magnetic flux density and measured simultaneously the temperature at three different positions along the centerline. A correlation of the measured temperature fluctuations gave the velocity in the centerline. For *glass 3* just three measurements were performed. Due to the difficult experimental conditions the standard deviation of these measurements is very large as shown in Figs. 3.33 and 3.34.

First let us compare the results obtained by the 3d numerical simulations and the measured data. In Fig. 3.33 the maximum velocity in the centerline u_{max} as a function of the electric potential difference between the electrodes U_E and the total heat input Q is shown.

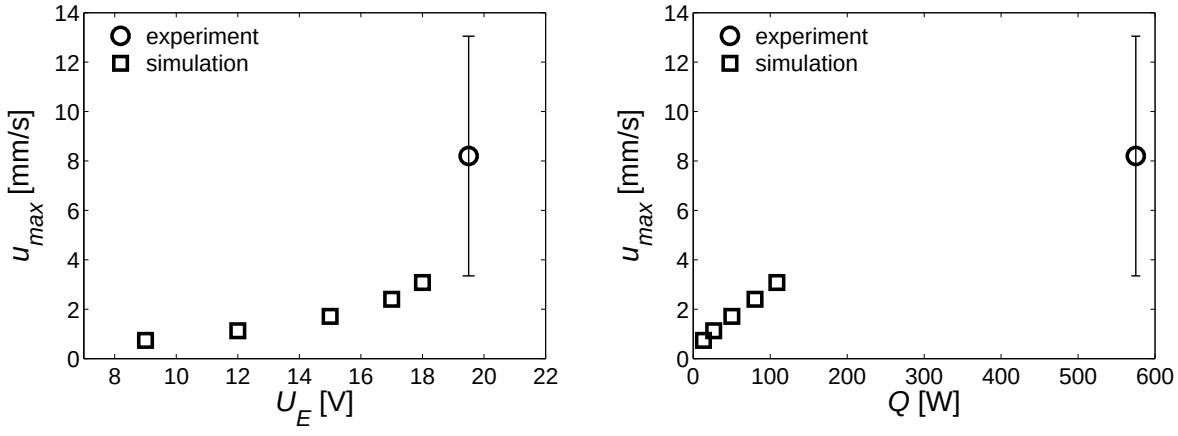

Figure 3.33: Comparison between numerical data which are already discussed in Sec. 3.1.3 and experimental data which are published by Krieger in [42]. The results are obtained for *glass 3* and $B_0 = 40$ mT. The maximum velocity in the centerline of the crucible u_{max} in mm/s is given as function of (a) the electric potential difference between the electrodes U_E in V, and (b) the total heat input Q in W.

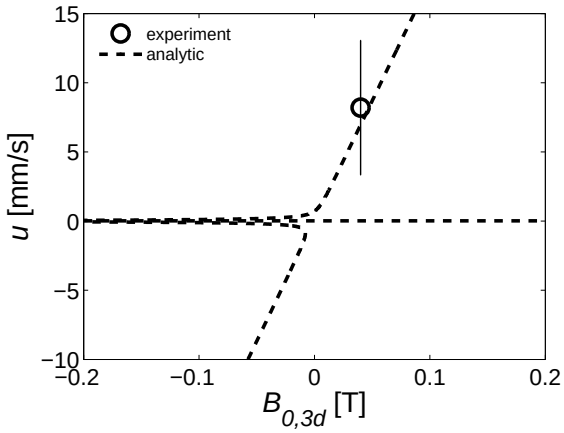

Figure 3.34: Comparison between analytical obtained data obtained with $\sigma = 4$ S/m, $J_0 = 6760$ A/m^2, $B_{0,1d} = 7.68 B_{0,3d}$ and experimental data with $Q = 575$ W, $B_0 = 40$ mT.

If one would extrapolate the value of U_E from the simulation results, one would obviously find a value within the experimental data range of values. The same holds for the values of Q from the simulation results. Furthermore, it is eye-catching that the increase of U_E from 18 V in the simulation to 19.5 V in the experiment leads to an increase of Q from 109 W to 575 W. It is the result of the exponential increase of the electrical conductivity in the corresponding temperature range. As already explained in Sec. 1.2 and the beginning of Sec. 3.1.3 the exponential increase of $\sigma(T)$ leads to a thermal instability which requires a continuous control of Q. Steady simulations as presented in this thesis converge for thermally stable regimes only. We identified thermal stability for an electric potential difference of $U_E \leq 18$ V. Unfortunately, no measurements for $U_E \leq 18$ V exist up to now.

Such measurements would allow a direct comparison between the steady 3d numerical simulations and the experiment. Also the analytical model meets the experimental data very well as shown in Fig. 3.34. We have chosen an electrical conductivity of $\sigma = 4$ S/m to obtain a current density of $J_0 = 6760$ A/m^2. Both comparisons show, that the steady numerical simulations and the steady analytical calculations are able to predict indirectly experimental data for unsteady regimes.

3.4 Summary and discussion

We have presented three-dimensional numerical studies of electromagnetically controlled thermal convection of glass melt in a small scale crucible with two rod electrodes in Sec. 3.1. The Lorentz force was imposed into the melt by the interaction of an external magnetic field with a constant density B_0 and an electric current density applied over the electrodes. During the simulations we varied the magnetic flux density between -120 mT $\leq B_0 \leq 120$ mT and the electrode potential between 3 V $\leq U_E \leq 18$ V. The studies show that the Lorentz force leads to an overall increase of the kinetic energy in the system. For example for $B_0 = 120$ mT and $U_E = 18$ V the volume-averaged velocity is 4.5 times larger than without Lorentz force. Especially below the electrodes, a region which is not affected by buoyancy, we observe a significant increase of the velocity. If the flow pattern is defined by the Lorentz force distribution, the mean velocity is a linear function of f_L. For $B_0 < 0$ T the transition from a buoyancy dominated flow regime to a Lorentz force dominated one and vice versa is characterized by a discontinuous modification of the flow pattern between the electrodes. The transition to a Lorentz force dominated regime takes place for different B_0 than the transition to a buoyancy dominated regime. As a result we pass through a hysteresis and obtain two steady solutions for one set of parameters depending on the starting conditions. The imposed Lorentz force also influences the theoretical maximum value of the stretching function – and hence the mixing. For a wide range of values of the imposed Lorentz force the maximum stretching function increases significantly. Furthermore, the maximum temperature in the melt increases considerably and leads to a worsening of the temperature homogenization. Only for $B_0 > 0$ T we observe an improvement of the temperature homogenization for all U_E.

We also observed a multiple-valued regime caused by the imposed Lorentz force with the one-dimensional analytical model which we studied in Sec. 3.2. The model describes buoyancy driven laminar steady flow of glass melt in a closed loop which is a very simplified representation of a closed streamline in the crucible. Furthermore, the model allows for the study of the influence of the temperature-dependent viscosity and electrical conductivity on the flow. In the presence of an imposed Lorentz force the convection of viscous fluids with temperature-dependent electrical conductivity in a circular loop can lead to a novel type of instability. If the dependence of electrical conductivity and the Lorentz force are sufficiently strong, three steady-state solutions can coexist. We also have determined the mechanism that underlies the non-uniqueness. For a viscous fluid with temperature-dependent viscosity we observed three convective regimes: (i) a stagnant regime for small Grashof numbers where the fluid is immobilized, (ii) a single-valued regime, which marks the onset of convection for a certain critical Grashof number $\mathrm{Gr_c}$, and (iii) a double-valued

regime for $Gr > Gr_c$ in which two velocities can be assigned to one Grashof number.

Overall, the results of the three-dimensional numerical simulations are predicted very well by the one-dimensional analytical model. It holds for characteristic velocities in the melt and the working temperature range. Even more, the flow characteristics obtained by the steady three-dimensional numerical simulations and the steady one-dimensional analytical model meet very well the experimentally determined velocity for an unsteady regime.

4 Outlook

You only grow by coming to the end of something and beginning something else.

J. Irving, The world according to garp

The analytical models and numerical simulations reported in the present thesis have explored the influence of the electromagnetic forces on the flow in glass melts. The electromagnetic forces were generated by an external magnetic field and a current density in the melt. Furthermore, the inclusion of the nonlinear temperature-dependent viscosity and electrical conductivity leads to a substantial number of new and interesting results. We have performed the studies for forced convection in a pipe with a circular cross section and for free convection in a cylindrical small-scale crucible as well as a closed loop. Future research activities into electromagnetically controlled glass melt flow should preferably continue the present theoretical work on both fields.

Further investigations of electromagnetically controlled pipe flow taking a multi-segment setup into account should benefit the application of electromagnetic forces in glass processing as feeders and forehearts are typically subdivided into various segments. The one-dimensional analytical model should be modified in such a way that the pipe consists of at least one heating, one cooling, and one adiabatic segment, whereas the Lorentz force should be part of the heating segment. Judging from our experience, we can expect that already such a multi-segment, one-dimensional pipe model could lead to sufficient accurate predictions of the electromagnetically controlled glass melt flow in feeders.

Electromagnetically forces aside, it is desirable to measure the monotonic non-linear laminar flow characteristic of glass melt in a pipe which we found for a heated system without cooling. Already a simple non-magnetic experiment like the one we introduced in Sec. 2.5 could verify our theory as this new flow regime is the result of the temperature-dependent viscosity.

Obvious areas of future work in the field of electromagnetically controlled free convection would include the precise quantification of the improvement of the glass melt homogeneity by Lorentz forces. A common tool is the statistical analysis of the deformation of particles, preferable length and surface stretch [59], [17], [68].

From the numerical side, the implementation of iterative algorithm to apply a defined heat input is desirable. It would allow for the application of higher constant electrical heat inputs. Furthermore, one should investigate the impact of frequent variation of the Lorentz force orientation with time-dependent calculations. It is conceivable that a time-dependent Lorentz force can significantly improve the mixing rate as it is known from

studies with mechanical stirrers [59]. Additionally, parameter studies of the electrode configuration could give optimal setups to maximize the effect of the Lorentz force on the flow. Beside the studied top-electrode, side- and bottom-electrodes should also be considered.

We hope our results will stimulate further studies on this intriguing topic leading finally to the industrial application of Lorentz forces in glass processing.

Bibliography

[1] M.J. Austin and D.E. Bourne. A mathematical model of an electric glass furnace. *Glass Technol.*, 14(3):78–84, 1973.

[2] C. M. Bender and S. A. Orszag. *Advanced Mathematical Methods for Scientists and Engineers*. Springer, 1991.

[3] V. Bojarevics, Y. Freibergs, E. I. Shilova, and E. V. Shcherbinin. *Electrically Induced Vortical Flows*. Kluwer Academic Publishers, 1988.

[4] J. R. Booker. Thermal convection with strongly temperature-dependent viscosity. *J. Fluid Mech.*, 76(4):741–754, 1976.

[5] D. Cepite, A. Jakovičs, B. Halbedel, and U. Krieger. Modeling of electromagnetic glass convection with temperature-dependent properties of the melt. *Magnetohydrodynamics*, 43(2):195–204, 2007.

[6] T.-S. Chen and R.E. Goodson. Computation of three-dimensional temperature and convective flow profiles for an electric glass furnace. *Glass Technol.*, 13(6):161–167, 1972.

[7] M. K. Choudhary. A three-dimensional mathematical model for flow and heat transfer in electrical glass furnace. *IEEE Trans. Ind. Gen. Appl.*, IA-22(5):912–921, 1986.

[8] M. K. Choudhary. A modeling study of flow and heat transfer in an electric melter. *Journal of Non-Crystalline Solids*, 101:41–53, 1988.

[9] M.K. Choudhary. A modeling study of flow and heat transfer in the vicinity of an electrode. In *Proceedings of the XVIIst International Congress on Glass*, pages 100–107, Beijing, 1995.

[10] Comsol AB. *COMSOL 3.2 Documentation*, 2005.

[11] H. F. Creveling, J. F. De Paz, J. Y. Baladi, and R. J. Schoenhals. Stability characteristics of a single-phase free convection loop. *J. Fluid Mech.*, 67(1):65–84, 1975.

[12] R.L. Curran. Use of mathematical modeling in determining the effects of electrode configuration on convection currents in an electric glass melter. *IEEE Trans. Ind. Gen. Appl.*, IGA-7(1):116–129, 1971.

[13] P. A. Davidson. Magnetohydrodynamics in materials processing. *Annu. Rev. Fluid Mech.*, 31:273–300, 1999.

[14] P. A. Davidson. *An Introduction to Magnetohydrodynamics*. Cambridge University Press, 2001.

[15] G. Desrayaud, A. Fichera, and M. Marcoux. Numerical investigation of natural circulation in a 2d-annular closed-loop thermosyphon. *Int. J. Heat Fluid Flow*, 27:154–166, 2006.

[16] P. Ehrhard and U. Müller. Dynamical behaviour of natural convection in a single-phase loop. *J. Fluid Mech.*, 217:487–518, 1990.

[17] H. Eisermann, U. Lange, H. Loch, and G. Weidmann. The intensity of mixing processes. In D. Krause and H. Loch, editors, *Mathematical simulation in glass technology, Schott Series on Glass and Glass Ceramics*. Springer Verlag, 2002.

[18] V.N. Fekolin and F.A. Stupak. Application of the magnetohydrodynamic effect for the stirring of glass melt, in Russian. *Steklo i Keram.*, 41(12), 1984.

[19] Fluent Inc. *FLUENT 6.3 Documentation*, 2006.

[20] Fluent Inc. *GAMBIT 2.3 Documentation*, 2006.

[21] N. Ghaddar. Analytical model of a side-heated free convection loop placed in a transverse magnetic field. *J. Fluid Eng.*, 120:62–69, 1998.

[22] N. Ghaddar. Analytical model of induced electric current from a free convection loop placed in a transverse magnetic field. *Int. J. Heat Mass Transfer*, 41(8-9):1075–1086, 1998.

[23] C. Giessler, U. Lange, and A. Thess. Nonlinear laminar pipe flow of fluids with strongly temperature-dependent material properties. *Phys. Fluids*, 19:043601, 2007.

[24] C. Giessler, R. Schlegel, and A. Thess. Numerical investigation of the flow of a glass melt through along circular pipe. *Int. J. Heat Fluid Flow*, page accepted for publication, 2008.

[25] C. Giessler, C. Sievert, U. Krieger, B. Halbedel, D. Hülsenberg, U. Lüdke, and A. Thess. A model for electromagnetic control of buoyancy driven convection in glass melts. *Fluid Dyn. Mat. Process.*, 1(3):247–266, 2005.

[26] C. Giessler and A. Thess. Analytical model of an electromagnetically controlled thermal fluid loop with strongly temperature-dependent material properties. *J. Fluid Mech.*, page accepted for publication, 2008.

[27] C. Giessler and A. Thess. Numerical simulation of electromagnetically controlled thermal convection of glass melt in a crucible. *Int. J. Heat Mass Transfer*, page accepted for publication, 2008.

[28] R. Greif. Natural circulation loops. *J. Heat Transfer*, 110:1243–1258, 1988.

[29] B. Halbedel, D. Hülsenberg, U. Krieger, U. Lüdtke, G. Carl, and H.-J. Linz. Methode and device for electromagnetically influencing the flow conditions in fluids of low electrical conductivity and high viscosity, 2007. WO 2007 065 937.

[30] K. R. Helfrich. Thermo-viscous fingering of flow in a thin gap: a model of magma flow in dikes and fissures. *J. Fluid Mech.*, 305:219–238, 1995.

[31] T. Hiemjima, H. Azuma, and M. Sawasaki. Numerical analysis and measurement of glass flow in a small melting furnace. *Glass Sci. Technol.*, 76(4):155–165, 2003.

[32] O. R. Hofmann and G. Philipp. Importance of Lorentz force in electrically heated glass melts. *Glastech. Ber.*, 65(5):142–149, 1992.

[33] O. R. Hofmann and A. Thess. Elektromagnetische Beeinflussung der Glasbadströmung – Ein neues Anwendungsgebiet der Magnetohydrodynamik (in German). *Glas-Ingenieur*, 1:39–45, 2002.

[34] P. Hrma. Criteria for physical modeling of electric glassmelting furnaces. *J. Am. Ceram. Soc.*, 66(7):519–523, 1983.

[35] D. Hülsenberg, B. Halbedel, G. Conrad, A. Thess, Y. Kolesnikov, and U. Lüdtke. Electromagnetic stirring of glass melts using Lorentz forces - experimental results. *Glass Sci. Technol.*, 77:186–193, 2004.

[36] D. Hülsenberg, B. Halbedel, U. Krieger, D. Schröpfer, A. Thess, and U. Lüdtke. Elektromagnetische Modifizierung von Strömungen in Schmelzen (in German). *Elektrowärme International*, 2:107–110, 2006.

[37] F. P. Incropera and D. P. DeWitt. *Fundamentals of Heat and Mass Transfer*. John Wiley, 1996.

[38] J. D. Jackson. *Classical Electrodynamics*. John Wiley, 1975.

[39] L. Jacoutot, P. Brun, A. Gagnoud, and Y. Fautrelle. Numerical modelling of natural convection in molten glass heated by induction. *Chemical Engineering and Processing*, page accepted for publication, 2008.

[40] C. Karcher, Y. Kolesnikov, V. Minchenya, and A. Thess. Industrielle Durchflussmessung in Aluminiumschmelzströmungen mittels Lorentzkraft-Anemometrie (in German). In *Proceedings Workshop Elektroprozesstechnik*, Heyda, 2007.

[41] J. B. Keller. Periodic oscillations in a model of thermal convection. *J. Fluid Mech.*, 26(3):599–606, 1966.

[42] U. Krieger. *Einfluss elektromagnetisch generierter Kraftwirkungen auf die Strömungen in Glasschmelzen (in German)*. PhD thesis, TU Ilmenau, 2007.

[43] U. Krieger, B. Halbedel, D. Hülsenberg, and A. Thess. Electromagnetic control of the glass melt flow in crucibles. *European J. Glass Sci. Technol. A*, page accepted for publication, 2008.

[44] R. Krishnamurti. On the transistion to turbulent convection. part 1. the transition from two- to three-dimensional flow. *J. Fluid Mech.*, 42:295–307, 1970.

[45] R. Krishnamurti. On the transistion to turbulent convection. part 2. the transition to time-dependent flow. *J. Fluid Mech.*, 42:309–320, 1970.

[46] F.A. Kulacki and R.J. Goldstein. Thermol convection in a horizontal fluid layer with uniform volumetric energy sources. *J. Fluid Mech.*, 55(2):271–287, 1972.

[47] C. Kunert, A. Langsdorf, F. Lentes, K. Duch, A. Thess, and Y. Kolesnikow. Verfahren und Anordnung zur Zufuhr einer Glasschmelze zu einem Verarbeitungsprozess (in German), 2004. DE 10 2004 015 055.

[48] U. Lange and H. Loch. Instabilities and stabilization of glass pipe flow. In D. Krause and H. Loch, editors, *Mathematical simulation in glass technology, Schott Series on Glass and Glass Ceramics*. Springer Verlag, 2002.

[49] K.-O. Lim, K.-S. Lee, and T.-H. Song. Primary and secondary instabilities in a glass-melting surface. *Numerical Heat Transfer, Part A*, 36:309–325, 1999.

[50] L. Mardorf and G. Woelk. Berechnung des Verhaltens einer elektrisch beheizten Glasschmelzwanne mit einem mathematischen Modell (in German). *Glastech. Ber.*, 54(4):73–84, 1983.

[51] A.E. Mikelson, V.N. Moshnyaga, A.D. Osmanis, V.T. Slavyanskij, and V.S. Shashkin. Methode of glass melting, in Russian, 1981. SU 814904.

[52] R. Moreau. *Magnetohydrodynamics*. Kluwer, 1990.

[53] L. Moresi and V. Solomatov. Numerical investigation of 2d convection with extremely large viscosity variations. *Phys. Fluids*, 7(9):2154–2162, 1995.

[54] G. Nölle. *Technik der Glasherstellung (in German)*. Deutscher Verlag für Grundstoffindustrie, 1997.

[55] H. Ockendon and J. R. Ockendon. Variable-viscosity flows in heated and cooled channels. *J. Fluid Mech.*, 83(1):177–190, 1977.

[56] M. Ogawa, G. Schubert, and A. Zebib. Numerical simulations of three-dimensional thermal convection in a fluid with strongly temperature-dependent viscosity. *J. Fluid Mech.*, 233:299–328, 1991.

[57] A. D. Osmanis, A. K. Snijedze, and A. M. Aglitis. Influence of electromagnetic stirring of glass melts (in Russian). In *Proceedings of the 12th Riga symposium on magnetohydrodynamics*, pages 179–183, Salaspils, USSR, 1987.

[58] A.D. Osmanis, A.E. Mikelson, L.Y. Pochs, I. Barbans, O.M. Mezhdrejs, V.V. Troshin, V.I. Butaeva, N.M. Vygorka, A.I. Grigorev, and V.M. Zalevskij. Methode of glass melting, in Russian, 1983. SU 1024423.

[59] J. M. Ottino. *The kinematics of mixing: streching, chaos, and transport*. Cambridge University Press, 1989.

[60] J. R. A Pearson. Variable-viscosity flows in channels with high heat generation. *J. Fluid Mech.*, 83(1):191–206, 1977.

[61] L. G. Poddubnaya and G. F. Shaidurov. Convective stability of a conducting fluid in a closed circuit. *Magnetohydrodynamics*, 5(2):63–66, 1969.

[62] W. H. Press, S. A. Teukolsky, W. T. Vetterling, and B. P. Flannery. *Numerical Recipes in C*. Cambridge University Press, 1992.

[63] S. M. Richardson. Injection moulding of theroplastics: Freezing of variable-viscosity fluids. iii. fully-developed flows. *Rheol. Acta*, 25:372–379, 1986.

[64] P. Schäfer and H. Herwig. Stability of plan poiseuille flow with temperature dependent viscosity. *Int. J. Heat Mass Transfer*, 36:2441–2448, 1993.

[65] R. Schlegel. Induktionsströme und Lorentzkräfte in Fluiden mit stark temperaturabhängiger elektrischer Leitfähigkeit - numerische 2D-Untersuchungen mit COMSOL (in German). Master's thesis, TU Ilmenau, 2006.

[66] SCHOTT. *Schott technical glasses - Physical and technical properties*, 2000. Corporate information.

[67] R. Schumacher. Stabilitätsprobleme beim Widerstandsheizen von Glasschmelzen (in German). *Glastech. Ber.*, 55(12):243–248, 1982.

[68] S. Schütz. *Berechnung und Analyse der Vermischung von Flüssigkeiten im Makro- und Mikromaßstab bei laminarer Strömung (in German)*. Shaker, 2006.

[69] H.-U. Seidel. *Zu einigen Fragen des vollelektrischen Schmelzens von Gläsern mittels elektrischer Widerstandsbeheizung (in German)*. PhD thesis, TU Ilmenau, 1977.

[70] J. Staněk. *Electric Melting of Glass*. Elsevier Scientific Publishing Company, 1977.

[71] S.P. Sutera and R. Skalak. The history of poiseuille's law. *Annu. Rev. Fluid Mech.*, 25:1–19, 1993.

[72] A. Thess, E.V. Votyakov, B. Knaepen, and O. Zikanov. Theory of the Lorentz force flowmeter. *New J. Phys.*, 9:299, 2007.

[73] A. Thess, E.V. Votyakov, and Y. Kolesnikov. Lorentz force velocimetry. *Phys. Rev. Lett.*, 96:164501, 2006.

[74] F. V. Tooley. *The handbook of glass manufacture*. Books for Industry Inc. and Glass Industry Magazine, 1974.

[75] K. E. Torrance and D. L. Turcotte. Thermal convection with large viscosity variation. *J. Fluid Mech.*, 47(1):113–125, 1971.

[76] W. Trier. *Glasschmelzöfen (in German)*. Springer, 1984.

[77] E. Truckenbrodt. *Fluidmechanik, Band 2 (in German)*. Springer, 1992.

[78] A. Ungan and R. Viskanta. Three-dimensional numerical simulation of circulation and heat transfer in an electrically boosted glass melting tank. *IEEE Trans. Ind. Appl.*, IA-22(5):922–933, 1986.

[79] A. Ungan and R. Viskanta. Three-dimensional numerical modeling of circulation and heat transfer in a glass melting tank, part 1. mathematical formulation. *Glastech. Ber.*, 60(3):71–78, 1987.

[80] A. Ungan and R. Viskanta. Three-dimensional numerical modeling of circulation and heat transfer in a glass melting tank, part 2. sample simulations. *Glastech. Ber.*, 60(4):115–124, 1987.

[81] J. R. Vávra. *Das Glas und die Jahrtausende (in German).* Artia, 1954.

[82] A.J. Walkden. Improvements in or relating to the manufacture of glass, 1972. GB 1289317.

[83] D. P. Wall and M. Nagata. Nonlinear equilibrium solutions for the channel flow of fluid with temperature-dependent viscosity. *J. Fluid Mech.*, 406:1–26, 2000.

[84] P. Welander. On the oscillatory instability of a differentially heated fluid loop. *J. Fluid Mech.*, 29(1):17–30, 1967.

[85] F. M. White. *Fluid Mechanics.* McGraw-Hill, 1999.

[86] J. A. Whitehead and K. R. Helfrich. Instability of flow with temperture-dependent viscosity: a model of magma dynamics. *J. Geophys. Res.*, 96(B3):4145–4155, 1991.

[87] J. J. Wylie and J. R. Lister. The effects of temperature-dependent viscosity on flow in a cooled channel with application to basaltic fissure eruption. *J. Fluid Mech.*, 305:239–261, 1995.

[88] Y. Zvirin. A review on natural circulation loops in pressurized water reactors and other systems. *Nuclear Engineering and Design*, 67:203–225, 1981.

A Appendix

A.1 Averaged momentum and energy equations for non-isothermal pipe flow

The one-dimensional pipe flow model formulated in Sec. 2.1 is based on the cross section averaged momentum and energy equations. In the following we like to give the reduction of the governing three-dimensional Stokes and heat equations (2.1)-(2.2) to the set of equations (2.4)-(2.5) for the one-dimensional mean temperature and velocity. A similar deviation applies for the one-dimensional equations we used for the model of electromagnetically driven thermal convection in Sec. 3.2.

The temperature can be split in two parts $T = T_0(x) + T_1(r, x)$, with $T_0(x)$ being the cross-section-averaged temperature field and $T_1(r, x)$ being the residual temperature field. The average of this residual temperature field over the cross section area S vanishes by definition, i.e. $\int\int T_1 dS = 0$. For small temperature residuals the temperature-dependent material parameters $\eta(T)$ and $\sigma(T)$ can be linearized according to $\eta(T) = \eta(T_0)+T_1\eta'(T_0)$ and $\sigma(T) = \sigma(T_0) + T_1\sigma'(T_0)$, respectively. The velocity of the fluid can be expressed in terms of the mean velocity u and the distribution function $f(r) = 2(1 - r^2/R^2)$ by $\mathbf{u} = uf(r)\mathbf{e_x}$. The assumed distribution function represents the parabolic Poiseuille profile being valid for a fully developed laminar pipe flow. The distribution function is normalized as follows $\int\int f(r)dS = 1$, where the integration is performed over the cross-section area.

After substituting the introduced velocity and temperature field into the energy equation (2.2), we integrate over the cross section area. The convective term

$$\int\int \rho_0 c_P(\mathbf{u}\cdot\nabla)T dS = \pi R^2 \rho_0 c_P u \frac{dT_0}{dx} + \rho_0 c_P u \int\int f(r)\frac{dT_1}{dx} dS$$

separates into two parts corresponding to the cross-section-averaged temperature field and the residual temperature field. The second term on the right hand side represents the stretching of temperature gradients by shear flow and is neglected. Also the diffusive term splits up in two components and can be rewritten as

$$\int\int \lambda_0 \nabla^2 T dS = \int\int \lambda_0 \frac{1}{r}\frac{\partial}{\partial r} r \frac{\partial T_1}{\partial r} dS + \pi R^2 \lambda_0 \frac{d^2 T_0}{dx^2}.$$

The first term on the right hand side represents the radial diffusion. The application of the Gauss-theorem $\int\int \lambda_0 \nabla \partial T_1/\partial r dS = \oint \lambda_0 \partial T_1/\partial r dr$ and the boundary condition $-\lambda_0 \partial T/\partial r = h(T_0 - T_\infty)$ at the sidewalls $r = R$ reduces the radial diffusion to a wall heat loss $-2\pi hR(T_0 - T_\infty)$. To transform the term of the Joule heating the inverse of

the electrical conductivity is expanded around T_0 with respect to T_1 for small values of T_1 and becomes $1/\sigma(T) = 1/\{\sigma(T_0) + T_1\sigma'(T_0)\} = 1/\sigma(T_0) - T_1\sigma'(T_0)/\sigma^2(T_0) + O(T_1^2)$. Neglecting higher order terms and applying the definition of T_1 the integrated term of Joule heating reduces to

$$\int\int \frac{J_0^2}{\sigma(T)} dS = \pi R^2 \frac{J_0^2}{\sigma(T_0)}.$$

Altogether, the simplified heat transfer equation becomes

$$\rho_0 c_P u \frac{dT_0}{dx} = \frac{J_0^2}{\sigma(T_0)} - \frac{2h}{R}(T_0 - T_\infty) + \lambda_0 \frac{d^2T_0}{dx^2}. \tag{A.1}$$

Since we assume that there is no overall pressure gradient, we have $p(0) = p(L)$ and the remaining axial momentum balance yields

$$0 = \frac{1}{r}\frac{\partial}{\partial r} r\eta(T) \frac{\partial u f(r)}{\partial r} + \rho_0 g + J_0 B_0.$$

This equation simplifies to $0 = -8\pi u\eta(T_0) + \pi R^2 \rho_0 g + \pi R^2 J_0 B_0$ after integration over the cross section area. During this integration the viscosity term splits into two parts according to

$$\int\int \frac{1}{r}\frac{\partial}{\partial r} r\eta(T) \frac{\partial u f(r)}{\partial r} dS = -8\pi u\eta(T_0) - \frac{4u}{R^2} \int\int \frac{1}{r}\frac{\partial}{\partial r} r^2 T_1 \eta'(T_0) dS).$$

The second term represents the modification of the shear stress caused by the residual temperature field T_1. We assume that this term has minor contribution and neglect it. This assumption helps us to keep the resulting one-dimensional equations as simple as possible. As the viscosity depends on temperature and therefore varies along the pipe axis, the resulting momentum equation is integrated over the pipe length and gives

$$L\rho_0 g + L J_0 B_0 = \frac{8u}{R^2} \int_0^L \eta(T_0) dx. \tag{A.2}$$

With the mentioned assumptions the energy equation (A.1) and the momentum equation (A.2) can be derived by applying the energy balance and the balance of the forces acting on a fluid element, see e.g. [37] and [85].

Both the heat equation (A.1) and the momentum equation (A.2) do not depend on the temperature residual field at all. The index of the temperature field is therefore omitted in Sec. 2.1.

A.2 Validation of convective boundary condition

Throughout this thesis we frequently use the convective thermal boundary condition and neglect effects of heat conduction through the wall. Now we like to show briefly the validity of this boundary condition.

Therefore we analyze the effective thermal resistance R_{eff} of the pipe. It is the sum of the resistance for heat conduction through the pipe wall

$$R_{cond} = \ln\left(\frac{R_{out}}{R}\right)\frac{1}{2\pi L\lambda_{wall}}$$

and the resistance for heat convection at the outer side of the wall

$$R_{conv} = \frac{1}{2\pi L R_{out} h,}$$

with R_{out} being the outer radius of the pipe, λ_{wall} being the heat conductivity of the wall, and h being the constant heat transfer coefficient, see for example [37]. Now we model the effective resistance $R_{eff} = R_{cond} + R_{conv}$ as effective heat convection

$$R_{eff} = \frac{1}{2\pi L R_{out} h_{eff}}.$$

The effective heat transfer coefficient h_{eff} then becomes

$$h_{eff} = \frac{h}{1 + \ln(R_{out}/R)R_{out}h/\lambda_{wall}}.$$

Typically the heat conductivity of such pipe walls in glass production is 102 W/(mK) and the thickness is about $R_{out} - R = 10^{-2}$ m. With a typical radius of $R = 0.025$ m and a typical heat transfer coefficient of $h = 5$ W/m^{2}K for free convection we have $\ln(R_{out}/R)R_{out}\alpha/\lambda_{wall} \to 1$ which leads to $h_{eff} \approx h$. Therefore it is legitimate to apply the convective boundary condition at the wall, see e.g. Sec. 2.1 and Eq. (2.21).

A.3 Estimation of heat transfer coefficient h

In the following we sketch how we derived the magnitude of the the heat transfer coefficient h at the outer surface of the crucible wall for the numerical simulations which we used in Sec. 3.1. The starting point for the estimation of h is the laminar free convection on an isothermal vertical surface. For this case the Nusselt number

$$\mathrm{Nu} = \frac{hH}{\lambda_{air}},$$

a measure of the convective heat transfer, can be rewritten in terms of the Grashof number $\mathrm{Gr_{air}}$ and an interpolation formula $g(\mathrm{Pr_{air}})$ of the Prandtl number $\mathrm{Pr_{air}}$ of the air outside the crucible according to [37]

$$\mathrm{Nu} = \frac{4}{3}\left(\frac{\mathrm{Gr_{air}}}{4}\right)^{1/4} g(\mathrm{Pr_{air}}).$$

If we assume a typical temperature difference between the crucible wall and the surrounding of 50 K and determine the air properties at the ambient temperature $T_\infty = 1393$ K, we obtain a heat transfer coefficient of $h \approx 4$W/m^{2}K.

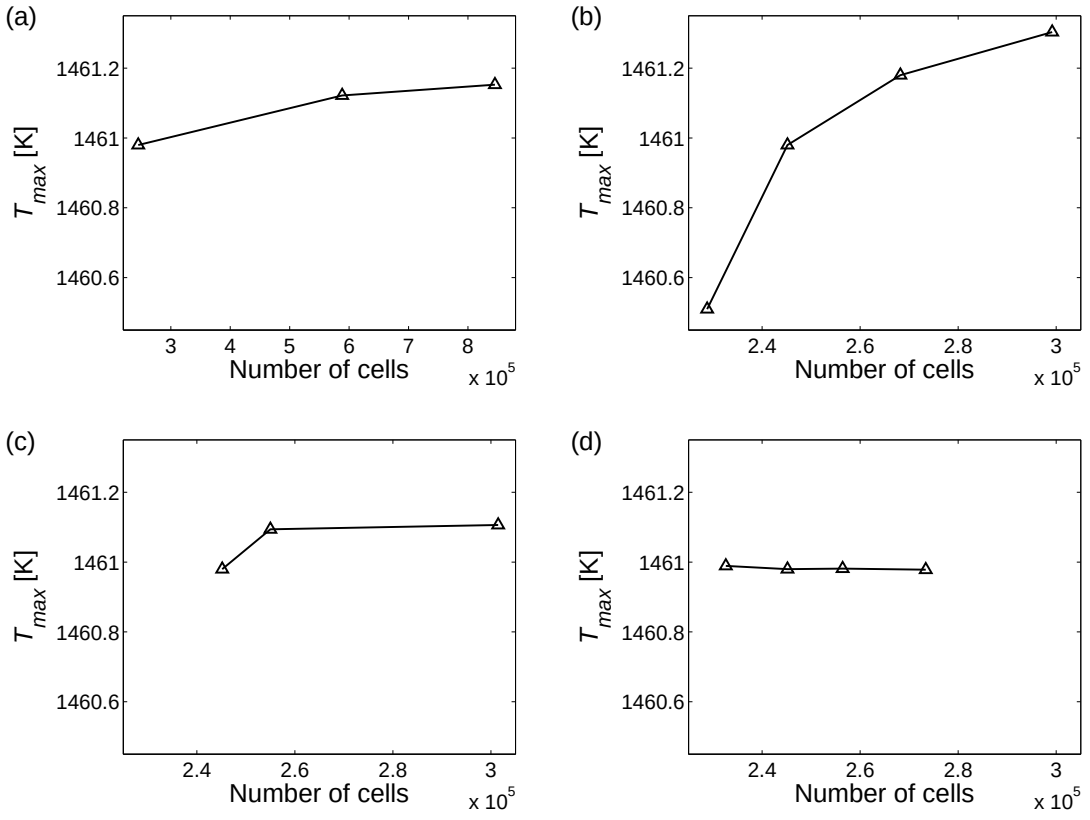

Figure A.1: Studies of the mesh on the basis of the maximum temperature in the melt T_{max} for varying element size: (a) size of the elements in the whole volume, (b) the element height below the free surface, (c) grid size of the elements around the electrode and (d) at the crucible wall.

A.4 Mesh study

The number of cells (a) in the whole volume, (b) close to the free surface, (c) around the electrode and (d) at the crucible wall may significantly influence the results of the numerical simulations of Sec. 3.1. The goal of the following mesh analysis is to find a mesh which maps all parameters of the system and the material properties very well. The influence of the mesh resolution is studied separately for (a)-(d) with the test case $U_E = 15$ V and $B_0 = -40$ mT. The meshes were validated on the basis of the maximum temperature T_{max} in the melt. In Fig. A.1 the evolution of T_{max} for each region of refinement (a)-(d) is shown.

Lets discuss in detail the need of refinement for the cases (a)-(d):

(a) During the first mesh study we changed the average size of all grid elements by varying the hight of the cells outside the boundary layers from $1 \cdot 10^{-3}$ m to $7.5 \cdot 10^{-4}$ m and $5 \cdot 10^{-4}$ m and keeping all other settings of the mesh constant. In Fig. A.1(a) a change of T_{max} can be observed tending to an asymptotic value for decreasing element size. As the reduction of the element size leads to an explosive increase of

the overall cell number and therefore to an explosive increase of the computational time we have chosen an average element size of $7.5 \cdot 10^{-4}$ m for the final mesh.

(b) As we expected large temperature gradients at the surface of the melt, we compared meshes with boundary layers thicknesses ranging from $8 \cdot 10^{-3}$ m to $1 \cdot 10^{-2}$ m and a thickness of the smallest cells ranging from $1 \cdot 10^{-3}$ m to $4 \cdot 10^{-4}$ m, $2 \cdot 10^{-4}$ m and $1 \cdot 10^{-4}$ m. For this mesh studies we observed the maximum variations in T_{max} as shown in Fig. A.1(b). But again the rate of changes also reduces with reducing element size and tends to an asymptotic value. As the ratio width/hight of an element should not exceed 1/10 [19], and the average width of a surface element is $1 \cdot 10^{-3}$ m we have chosen an element thickness of $1 \cdot 10^{-4}$ m.

(c) The need to study the influence of the grid size around the electrode is twofold. First, the electric current flowing from one rod electrode to another meets the greatest electric current density in the immediate vicinity of the electrodes. Consequently, these regions acquire high local temperatures. As the electrical conductivity is increasing expontially with the temperature, a good mapping of the property law $\sigma(T)$ requires a fine mesh in hot regions of the melt. Furthermore, at the squared edges of the electrode the exact solution of the Laplace Eq. (3.10) has a singularity. The numerics yields in high values of $\nabla\phi$ at the edges which require a refinement as well [38]. We have compared a mesh without boundary layer around the electrode with two meshes with a boundary layer thickness of $\delta = 5 \cdot 10^{-3}$ m and the smallest cell sizes of $4 \cdot 10^{-4}$ m and $2 \cdot 10^{-4}$ m. A significant change can be observed if we compare meshes without boundary layer. A refinement of the boundary layer cells leads to an rapid convergence towards an asymptotic value, see Fig. A.1(c).

(d) The Prandtl Number Pr, which describes the ratio between thermal and viscous diffusion, is for glass melts about $\mathrm{Pr} \approx 100$. Furthermore, it is a measure of the ratio between the velocity boundary layer thickness δ_s and the temperature boundary layer thickness δ_t. As the relation $\mathrm{Pr}^{1/2} \sim (\delta_s/\delta_t)$ is valid for laminar flow at a flat plate [77], we can expect that δ_t is about ten times smaller than δ_s. Due to the small dimensions we do not expect free flow and have the smallest velocity boundary layer thickness between the electrode and the crucible wall with $\delta_s = 8.5 \cdot 10^{-3}$ m, and hence at theoretical thermal boundary layer thickness of $\delta_t = 8.5 \cdot 10^{-4}$ m. A proper resolution with 10 cells requires an average cell thickness of $8.5 \cdot 10^{-5}$ m. We studied the influence of the resolution of the thermal boundary layer by refining the thickness the smallest cells at the crucible wall from $4 \cdot 10^{-4}$, $2 \cdot 10^{-4}$, $1 \cdot 10^{-4}$ to $5 \cdot 10^{-5}$. The results in Fig. A.1(d) show that the influence of the boundary layer thickness at the crucible wall is negligible.

Fig. A.2 shows the mesh of the crucible geometry (Figs. 3.1, 3.2), which we finally used for the numerical simulations.

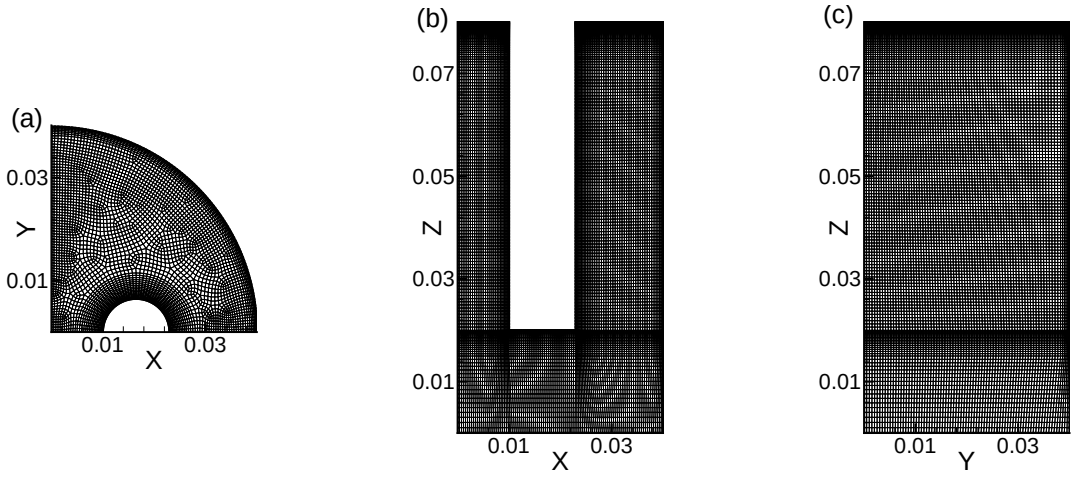

Figure A.2: Final mesh for the quarter crucible corresponding to Fig. 3.1 at (a) $z = 0.04$ m, (b) the symmetry plane $y = 0$ m and (c) the symmetry plane $x = 0$ m.

A.5 Material properties

Throughout this thesis we perform calculations with three types of glass melt. The material property data are listed in Tabs. A.1 and A.2. Additionally, the viscosity η and the electrical conductivity σ are given as function of the temperature in Fig. A.3.

Property	Glass 1 (SCHOTT glass nb. 8412)	Glass 2 (SCHOTT glass nb. 8252)
Viscosity η	$0.01\text{Pas} \cdot \exp\left(\frac{10700\text{K}}{T-515.4\text{K}}\right)$	$6.77 \cdot 10^{-6}\text{Pas} \cdot \exp\left(\frac{18600\text{K}}{T-522.9\text{K}}\right)$
Electrical conductivity σ	$738.9\frac{\text{S}}{\text{m}} \cdot \exp\left(-\frac{7680\text{K}}{T}\right)$	$1.21 \cdot 10^{6}\frac{\text{S}}{\text{m}} \cdot \exp\left(-\frac{26100\text{K}}{T}\right)$
Density ρ_0	$2200\frac{\text{kg}}{\text{m}^3}$	$2420\frac{\text{kg}}{\text{m}^3}$
Heat conductivity λ_0	$1.2\frac{\text{W}}{\text{mK}}$	$1.1\frac{\text{W}}{\text{mK}}$
Heat capacity c_P	$1450\frac{\text{J}}{\text{kgK}}$	$1450\frac{\text{J}}{\text{kgK}}$

Table A.1: Thermophysical properties [66] of the glasses used for the example calculations and the numerical validation of the analytical pipe flow model in chapter 2.

Property	Glass 3 (47.7%BaO-20.0%B_2O_3-27.1%SiO_2-5.2%FeO_2)
Viscosity η	$9.92 \cdot 10^{-2}\text{Pas} \cdot \exp\left(\frac{1046.20\text{K}}{T-1033.41\text{K}}\right)$
Electrical conductivity σ	$1.74 \cdot 10^{6}\frac{\text{S}}{\text{m}} \cdot \exp\left(-\frac{20300\text{K}}{T}\right)$
Density ρ	$3931.5\frac{\text{kg}}{\text{m}^3} - 0.3953\frac{\text{kg}}{\text{m}^3\text{K}} \cdot T$
Heat conductivity λ	$2 \cdot 10^{-6}\frac{\text{W}}{\text{mK}^3} \cdot T^2 - 3.2 \cdot 10^{-3}\frac{\text{W}}{\text{mK}^2} \cdot T + 2.68\frac{\text{W}}{\text{mK}}$
Heat capacity c_P	$1285\frac{\text{J}}{\text{kgK}}$

Table A.2: Thermophysical properties of the composition 47.7%BaO-20.0%B_2O_3-27.1%SiO_2-5.2FeO_2 (all data in mass%) which are used for the three-dimensional simulations and the one-dimensional convection model in chapter 3.

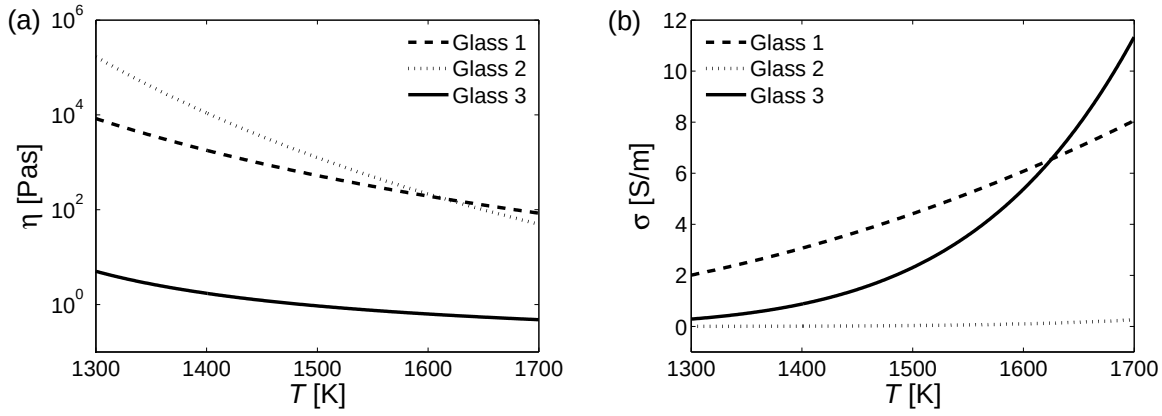

Figure A.3: (a) Viscosity η and (b) electrical conductivity σ as function of the temperature T for the three glass melt compositions we consider in this thesis. The material property laws are given in Tabs. A.1 and A.1.

Acknowledgements

I would like to express my deep gratitude to Prof. A. Thess for introducing to me the interesting topic of electromagnetic control of glass melt flow. The combination of advice, trust, and liberty that he has offered me, has made the research pleasant and fulfilling.

Furthermore, I would like to thank the members of the Forschergruppe Magnetofluiddynamik for the fruitful discussions. I have learned much from them about the interesting subject of magnetohydrodynamics.

I would also like to acknowledge my colleagues at the groups Thermo- and Magnetohydrodynamic and Theoretical Fluid Dynamic. I will fondly remember the support and friendly working environment. Especially I like to thank our group of PhD students with A. Ebert, E. Drapala, J. Langebach, and S. Senin for our friendship and motivation.

I am very grateful to the administrator of the computer center of the TU Ilmenau H. Schwanbeck for his invaluable and incredible support during all stages of the numerical studies.

Finally, I can hardly express my gratitude to thank my family for their support, encouragement, and unlimited patience.